공학박사학위논문

사각 팽창관 내 기포류 유동에서 재부착길이 변화에 대한 실험연구

Experimental study on the reattachment length variation in the bubbly flow in a sudden expansion square pipe

2023년 8월

서울대학교 대학원
기계항공공학부
김 예 원

사각 팽창관 내 기포류 유동에서
재부착길이 변화에 대한 실험연구

Experimental study on the reattachment length variation in the bubbly flow in a sudden expansion square pipe

지도교수 박 형 민

이 논문을 공학박사 학위논문으로 제출함

2023년 4월

서울대학교 대학원
기계항공공학부
김 예 원

김예원의 공학박사 학위논문을 인준함

2023년 6월

위 원 장: _____김 호 영_____ (Signature)
부위원장: _____박 형 민_____ (Signature)
위   원: _____황 원 태_____ (Signature)
위   원: _____고 한 서_____ (Signature)
위   원: _____유 재 영_____ (Signature)

Experimental study on the reattachment length variation in the bubbly flow in a sudden expansion square pipe

Yewon Kim
Department of Mechanical and Aerospace Engineering
Seoul National University

Abstract

In the present study, we experimentally investigate the flow characteristics of both phases in the air-water flow in a sudden expansion square pipe, by measuring the gas and liquid phases simultaneously with high-speed two-phase particle image velocimetry (PIV) and shadowgraph techniques. We consider two Reynolds numbers for the liquid-phase (background) flow as Re = 400 (laminar), and 6000 (turbulent), respectively, and two area expansion ratios as ER = 4.0 and 9.0. The mean volume void fraction ($\langle \bar{\alpha} \rangle$) is varied as 0.12-2.80%. For the gas phase, we developed an automated deep learning-based bubble mask extraction algorithm, that can save time by replacing existing image processing techniques and applying it to the bubble characteristics analysis. We measure the three-dimensional void distribution, bubble velocities, and trajectories, which are captured at the same time with the liquid-phase velocity field that was also compared to the single-phase flow measured under the same condition. It is observed that larger bubbles experience a stronger lift force and move towards the wall faster than smaller bubbles after expansion which is more encouraged by the steeper velocity gradient with increasing the Reynolds number.

However, at a lower expansion ratio, the larger bubbles are unable to overcome the wall repulsion force and rise in a pipe core region, at a higher expansion ratio, larger bubbles are able to reach the wall and exhibit a peak in bubble size near the wall. In addition, the effect of ER and average void fraction on the change in liquid flow characteristics is analyzed, and the effect of gas-phase and pipe geometry on the rate

of development of the shear layer is analyzed by calculating the shear layer vorticity thickness. Based on the measured flow statistics, the interfacial forces acting on the rising bubbles are calculated to explain the void distribution, which is largely governed by the liquid-phase flow characteristics. Affected by the bubble distribution, the enhanced turbulence in the inlet flow energizes the separating shear layer, resulting in the reduction of reattachment length behind the edge. Finally, we summarize the changes in reattachment length according to flow conditions and pipe geometry, in particular, analyze the effects of ER and mean void fractions. We expect that the present results will assist the deeper understanding of the interaction between different phases and the change of reattachment length depending on the flow conditions in the gas-liquid flow in sudden expansion geometry, which is close to practical interest.

Keyword : sudden expansion pipe, bubble-induced turbulence, reattachment length, two-phase particle-image velocimetry, deep learning mask extraction

Student Number : 2016-29877

To my family for their love and support

Table of Contents

List of Tables

List of Figures

Nomenclature

Roman symbols

AR bubble aspect ratio

AP   mask average precision, averaged over IoU thresholds 0.5 to 0.95 with 0.05 intervals

AP_{50} mask average precision for the cases of IoU $\geq$ 0.5

AP_{75} mask average precision for the cases of IoU $\geq$ 0.75

AP_L mask average precision for large bubbles (d_b < 22.6 pixels)

AP_M mask average precision for medium bubbles (22.6 pixels $\leq d_b$ < 39.5 pixels)

AP_S mask average precision for small bubbles (d_b > 39.5 pixels)

c_p pressure coefficient

C force coefficient

D pipe width after expansion

d pipe width before expansion

d_e equivalent bubble diameter, $2(3V/4\pi)^{1/3}$

Eo Eötvös number, $Eo = g(\rho_l - \rho_g)<d_e>^2/\sigma$

ER Expansion ratio, $ER = D^2/d^2$

F lateral force acting on bubble

g gravitational acceleration

h step height, $(D-d)/2$

I light intensity

IoU   intersection over union

IoU_B	intersection over union between two bounding boxes
J_G	gas flow rate
J_L	liquid flow rate
k	turbulent kinetic energy
M	pixel magnification factor
$N_{detected}$	number of detected bubbles
Q_L	volumetric liquid flow rate
Re	liquid-phase Reynolds number, $Re = u_{bilk}d/v$
Re_b	bubble Reynolds number, $Re_b = \langle \bar{v}_r \rangle \langle \bar{d}_e \rangle/v$
s	displacement
t	time
u_{bulk}	inlet bulk velocity, $u_{bulk} = Q_L/d^2$
u_x	liquid lateral velocity
$u_{x,b}$	bubble lateral velocity
u_z	liquid streamwise velocity
$u_{z,b}$	bubble rise velocity
$u'_{x,rms}$	root-mean-square of liquid-phase lateral velocity fluctuations
$u'_{z,rms}$	root-mean-square of liquid-phase streamwise velocity fluctuations
U_{piv}	velocity obtained from PIV, $U_{piv} = M\Delta s/\Delta t$
V	volume of the bubble
v_r	relative rise velocity
We	Weber number, $We = \rho_l \langle \bar{v}_r \rangle^2 \langle \bar{d}_e \rangle/\sigma,$
w	weight factor

x	coordinate in a lateral direction
y	coordinate in a spanwise direction
z	coordinate in a streamwise direction
z_R	reattachment length

Greek Symbols

α	void fraction
β	volumetric quality
δ_ω	shear layer vorticity thickness
ω	vorticity
ρ_l	density of water
ρ_g	density of air
σ	surface tension of water
μ	dynamic viscosity
v	kinematic viscosity of water

Superscripts

$(\bar{\ })$	time-averaged quantity
$(\ )'$	total fluctuation liquid-phase
$(\ )''$	fluctuation by bubbles
$<>$	spatial averaged quantity

Subscripts

b	bubble

D	drag
e	equivalent
g	gas-phase
l	liquid-phase
L	lift
r	relative
TD	turbulent dispersion
W	*w*all-lubricant

Abbreviations

BIT	bubble-induced turbulence
ER	expansion ratio
PDF	probability density function
PIV	particle-image velocimetry
PTV	particle tracking velocimetry
SIT	shear-induced turbulence

Chapter 1.

Introduction

1.1 Upward bubbly pipe flow

There are many hydrodynamic functionalities we can obtain through the interaction between different phases; and among them, it is well recognized that the gas-liquid two-phase flow effectively modulates the turbulence characteristics, heat transfer, and mixing, compared to the single-phase flow. Therefore, many previous studies have been performed to understand the interactive influences between two phases in gas-liquid two-phase flow, especially in the regime of bubbly flow in a pipe or channel. Depending on the ratio between gas and liquid fluxes, the position of the locally maximum concentration of gas bubbles tends to move from near-wall (wall-peaking) to core (core-peaking) region (Serizawa et al., 1975; Van der Welle, 1985; Wang et al., 1987; Kashinsky et al., 1993; Liu and Bankoff, 1993; Lu et al., 2006; Hosokawa et al., 2012; Hosokawa & Tomiyama, 2013; Kim et al., 2016).

On the other hand, it is well understood that the gas bubbles may suppress or enhance liquid-phase turbulence depending on ratio of gas to liquid flow rate, bubble size, liquid-phase Reynolds number, void fraction distribution, and distance to the solid wall (Hosokawa et al., 2012; Hosokawa & Tomiyama, 2013; Kim et al., 2016; Lance & Bataille, 1991; Serizawa et al., 1975; Wang et al., 1987). For example, Serizawa et al. (1975) commented that the turbulent intensity initially decreases with increasing gas-flow rate and increases again with further increasing of flow rate at constant water superficial velocity. In addition, Wang et al. (1987) reported that air bubbles with higher gas flow rate suppress the turbulence intensity of the liquid-phase because bubbles enhance dissipation as well as promote the production of turbulent kinetic energy.

For the nature of two-phase flow turbulence, in particular, it is understood that it has two contributions of the shear-induced turbulence (SIT) existing in a single-phase flow and of the bubble-induced turbulence (BIT) (Hosokawa & Tomiyama,

2013; Kim et al., 2016; Lance & Bataille, 1991; Martínez-Mercado et al., 2007; Michiyoshi & Serizawa, 1986; Riboux et al., 2010; 2013; Theofanous & Sullivan, 1982). Theofanous & Sullivan (1982) explained that the agitation due to bubbles shows up as an additive to the wall shear-generated turbulence. As Lance & Bataille (1991) pointed out, on the other hand, a simple superposition of them is not enough to explain the complex trends in a wide range of different flow conditions and it is also important to distinguish the pure agitation due to bubbles (so-called pseudo-turbulence) and the bubble-induced modulation of the SIT (Wang et al., 1987; Liu & Bankoff, 1993). For the orientation of this bubble-induced turbulence, the interaction between unsteady wake structures behind each bubble has been suggested, in general (Kim et al., 2016; Lance & Bataille, 1991; Lee & Park, 2017; Rensen et al., 2005; Riboux et al., 2010; 2013), which is also the major mechanism of mass transfer due to bubbles (Fan & Tsuchiya, 1990; Stöhr et al., 2009).

1.2 Sudden expansion geometry flows

1.2.1 Backward-facing step flow

While previous efforts have greatly enhanced our understanding of the physics behind the interaction between gas and liquid phases in bubbly flows, mostly they have been performed on a straight (constant cross-sectional area) pipe (channel) flows. Considering that in practical (industrial) situations where the gas-liquid bubbly flows play an important role in determining its thermal-fluid characteristics, more complex geometries such as bend and sudden change in the cross-sectional area are frequently involved.

In particular, flow through the sudden expansion pipe (channel), also known as a backward-facing step flow, is characterized by the boundary-layer separation, reattachment, and re-development and is closely related to the fluid mixing (reattachment length (z_R) as an indirect measure of mixing), which is an important issue in industrial applications such as the chemical reactors, combustors, heat exchanger, and nuclear power plants.

Thus, there have been many fundamental studies on the dependence of

reattachment length on flow conditions such as expansion ratio (*ER*), inlet turbulence, and Reynolds number (Re), for the single-phase backstep flow (Adams & Johnston, 1988; Furuichi et al., 2003; Jović, 1998; Kim et al., 1980; Ötügen 1991; So, 1987). It has been shown that the reattachment length decreases with increasing the expansion ratio (Ötügen, 1991) and inlet turbulence (So, 1987). In the laminar flow regime, the reattachment length increases with increasing up to Re ~ 1000 and then decreases to be constant over a turbulent flow regime (Furuichi et al. 2003).

Based on this knowledge, there have been active investigations to control the flow over the backward-facing step to reduce the reattachment length through two-dimensional forcings or three-dimensional perturbations (Chun & Sung, 1996; Gai & Sharma, 1994; Kang & Choi, 2002; Park et al., 2007)

1.2.2 Sudden expansion pipe

Reflecting the academic interest and practical importance of the flow in discussion, the two-phase flows in sudden expansion pipe (channel) have been also investigated so far (Aloui et al., 1999; Aloui & Souhar, 1996; Attou et al., 1997; Fessler & Eaton, 1999; Pakhomov & Terekhov, 2016; Petrick & Swanson, 1959; Rinne & Loth, 1996; Voutsinas et al., 2009). Table 1.1 summarizes the previous and present studies for two-phase flows in a sudden expan- sion channel geometry. While the turbulence modulation due to solid particle loadings in gas flow has been performed by Fessler & Eaton (1999), most of the studies on gas-liquid flows in sudden expansion geometry have focused on the change in the singular pressure drop depending on void fraction, expansion ratio, and bubble size.

Petrick & Swanson (1959) experimentally investigated the effects of sudden expansion on the relative velocity between two phases and showed that the void fraction after sudden expansion increases as the expansion ratio increases. Similarly, theoretical models for singular pressure drop and void fraction distribution of gas-liquid flows in sudden expansion pipe have been proposed (Attou et al., 1997; Pakhomov & Terekhov, 2016).

On the other hand, a few studies performed experimental measurements of bubble distribution, liquid-phase flow characteristics as well as pressure drop. Aloui

& Souhar (1996) visualized the bubbles in gas-liquid two-phase flow in a sudden expanded flat duct (*Re* = 29,000) and showed that local no-slip occurs in the recirculation zone. Aloui et al. (1999) expanded the former work to a two-phase flow in a sudden expansion pipe (*Re* = 40,000 - 80,000) to verify the model for singular pressure drop. Also, they measured bubble characteristics such as void fraction, bubble velocity, and bubble size distribution, by which some aspects of bubble dynamics were understood. They pointed out that the bubbles get smaller as they move through the singularity point (i.e., position of sudden expansion), which is due to the increased pressure and the higher rate of breakup than coalescence of bubbles.

Although there have been some studies on the bubbly flows in a pipe (channel) with sudden expansion, we think our understanding of the detailed two-phase flow phenomena is not enough compared to that of the single-phase flow in the same geometry or that of the two-phase flow in a straight pipe with a constant cross-section.

Furthermore, most previous studies tended to focus on the singular pressure drop rather than the flow structure itself or the interaction between two phases occurring across the expansion. In addition, most of the previous studies were conducted intensively on small expansion ratios (*ER* < 4.0) although industrial facilities are operated with high expansion ratios. For example, some expansion joints used in heating, ventilating, and air conditioning systems have an expansion ratio of nearly 4, and mixing chambers used in water treatment have an expansion ratio of 9 or more. In summary, despite previous intensive efforts, we think that (i) the temporal and spatial changes in instantaneous flow fields, (ii) the detailed relation between the bubble dynamics and liquid flow statistics, and (iii) bubbly flows in high expansion ratios are strongly required to be investigated.

1.3 Main purposes

Therefore, in the present study, we experimentally investigate the flow characteristics of both phases in the air-water flow in a sudden expansion square pipe, by measuring the gas and liquid phases simultaneously with high-speed two-phase particle image velocimetry (PIV) and shadowgraph techniques. We consider two Reynolds numbers for the liquid-phase (background) flow as *Re* = 400 (laminar),

and 6000 (turbulent), respectively, and two area expansion ratios as $ER = 4.0$ and 9.0. The mean volume void fraction ($\langle \bar{\alpha} \rangle$) is varied as 0.12-2.80%. For the gas phase, we developed an automated deep learning-based bubble mask extraction algorithm, that can save time by replacing existing image processing techniques and applying it to the bubble characteristics analysis.

We measure the three-dimensional void distribution, bubble velocities, and trajectories, which are captured at the same time with the liquid-phase velocity field that will be also compared to the single-phase flow measured under the same condition. In addition, the effect of ER and average void fraction on the change in liquid flow characteristics was analyzed, and the effect of gas-phase and pipe geometry on the rate of development of the shear layer was analyzed by calculating the shear layer vorticity thickness. Based on the measured flow statistics, the interfacial forces acting on the rising bubbles are calculated to explain the void distribution, which is largely governed by the liquid-phase flow characteristics.

Finally, we summarize the changes in reattachment length according to flow conditions and pipe geometry, in particular, analyze the effects of ER and mean void fractions. We expect that the present results will assist the deeper understanding of the interaction between different phases and the change of reattachment length depending on the flow conditions in the gas-liquid flow in sudden expansion geometry, which is close to practical interest.

The paper is organized as follows. In §2, we explain the experimental setup including a high-speed shadowgraph, two-phase particle image velocimetry, and bubble velocity measurement using an optical flow algorithm. Next, we will discuss the training process and the test results under various flow conditions of the developed deep learning-based bubble segmentation algorithm in §3. Next, we will discuss in detail how the gas and liquid phases interact with each other across the sudden expansion in upward channel flow in §4 and 5. Also, we will calculate shear layer vorticity thickness and estimate the hydrodynamic forces acting on the rising bubble to explain the specific void distribution. And we analyze the reattachment length changes according to the flow conditions and ER in §6. The summary and conclusions will be given in §7.

Reference	Flow type	ER	$Re \times 10^{-4}$	$\langle \bar{\alpha} \rangle$ [%]	β	z_R	D	C	Focuses
Aloui and Souhar, 1996	N$_2$-C6N6FeK3 solution	2.3	2.9	-	0.2-0.3	Y	Y	Y	skewness factor
Aloui et al., 1999		2.3-9.0	4.0-8.0	6-11	0.1-0.2	Y	Y	N	singular pressure drop
Attou et al., 1997	Air-water	2.3-9.0	< 12.5	< 50	< 0.7	N	N	N	singular pressure drop
Fessler and Eaton, 1999	Particle-air	1.7	1.8	3-40	-	Y	Y	Y	turbulence modification
Pakhomov and Ter ekhov, 2016	Air-water	7.1	0.8-4.2	-	< 0.1	Y	Y	Y	wall friction, heat transfer
Petrick and Swans on, 1959	Air-water	1.3-8.0	0.1-3.9	20-80	0.1-0.9	N	Y	N	void fraction model
Rinne and Loth, 19 96	Air-water	5.1	1.4-4.2	-	0.06-0.5	N	Y	N	interfacial area concentration
Voutsinas et al., 20 09	CO$_2$-water	5.4	2.3	-	< 0.1	N	Y	N	pressure drop and fluctuation
Present study	Air-water	4.0-9.0	≤ 0.6	≤ 2.8	< 0.12	Y	Y	Y	bubble dispersion, flow modification (reattachment)

Table 1.1 Summary of flow conditions and results of previous and present studies for two-phase sudden expansion flow. *ER*: area expansion ratio; *Re*: liquid-phase Reynolds number; $\langle \bar{\alpha} \rangle$: inlet volume void fraction; *β*: volumetric quality; z_R: reattachment length measurement; D: dispersed phase flow statistics; C: continuous phase flow statistics.

Chapter 2.

Experimental setup and procedure

2.1 Flow facilities

The present experiments are carried out in an air-water circulating system, as shown in Fig. 2.1 From the reservoir, tap water at room temperature is supplied by the water pump (PM-403PI, WILO pump Ltd.) into a vertically aligned square channel (width of d = 20 mm) whose cross section increases with an expansion ratio of $ER = D^2/d^2$ = 4.0 and 9.0 (step height $h = (D-d)/2$), at $41d$ downstream from the inlet. Thus the square channel after the expansion has a width of D = 40 and 60 mm. The streamwise length of the test section (made of acrylic) after the expansion is approximately $9D$ and $16D$ for ER = 4.0 and 9.0 to measure the reattachment length of laminar single-phase flow, respectively. The water flow rate is precisely controlled by the regulator and monitored by a flow meter (KTM-800, KOMETER) to maintain the targeted superficial velocity of the liquid phase during the experiments. For the background liquid-phase flow, we consider three Reynolds numbers ($Re = u_{bilk}d/v$), based on the inlet bulk velocity ($u_{bulk} = Q_L/d^2$, Q_L: volumetric liquid flow rate) and channel width (d) before the expansion; Re = 400 (laminar flow), and 6000 (turbulent flow).

For the gas-phase, the air generated from a compressor is first stored in a pressure chamber whose pressure is set by a pressure regulator, which is then introduced to the bubble generator located at the bottom through a flow meter (PFMV5, SMC) in the range of 0.5-500 mL/min (Fig. 1). At the top of bubble generator, the 4 × 4 array of needles whose tip has an inner diameter of 0.018 mm is located. The size and configuration of the needles should be determined based on the flow conditions. Furthermore, it is important to optimize the ratio between the flow rate and air pressure to achieve the desired condition of bubbles.

For each Reynolds number considered, the mean volume void fraction is varied as $\langle \bar{\alpha} \rangle$ = 0.29 to 2.80% for Re = 400, and 0.12 to 1.85% for Re = 6000, respectively (see Table 2.1 for the details), which is measured at z/d = -1, before the expansion.

For each case, the size of the bubble is characterized by the bubble shadow image projected on two planes perpendicular to each other (see section 2.2.1, each bubble reconstructed as a series of ellipses from two perpendicular projected images.). Based on the Reynolds and Eötvös numbers (Clift et al. 1978), the bubbles in the present study have a wobbling shape (see Fig. 2.3b) that has been approximated as an oblate ellipsoid in previous studies (Fujiwara et al., 2004; Jeong & Park, 2015; Kim et al., 2016; Lee & Park, 2017). Therefore, based on the projected shape on each two-dimensional plane, the equivalent bubble diameter (d_e) is defined as $d_e = 2(3V/4\pi)^{1/3}$ (V = volume of the bubble, see section 2.2.1).

Table 2.1 summarizes the conditions of the gas phase considered in the present study. For each Re, the mean bubble diameter, $\langle \bar{d}_e \rangle$, tends to slightly increase with increasing $\langle \bar{\alpha} \rangle$ and ranges from 1.62 to 3.56 mm. The bubble Reynolds and Weber numbers are defined based on $\bar{d}_e$ and relative rise velocity (v_r) such as $Re_b = \langle \bar{v}_r \rangle \langle \bar{d}_e \rangle / v$ and $We = \rho_l \langle \bar{v}_r \rangle^2 \langle \bar{d}_e \rangle / \sigma$, which are in the ranges of 20-770 and 0.003-2.95, respectively. This indicates that the present bubbles are deformable and subject to path (i.e., rising along oscillatory paths) instability. The Eötvös number is also calculated as $Eo = g(\rho_l - \rho_g) \langle \bar{d}_e \rangle^2 / \sigma$. Here, v and ρ_l are the kinematic viscosity and density of water, ρ_g is the density of air, σ is the surface tension of water, and g is the gravitational acceleration.

On the other hand, Fig. 2.2 shows the probability density function (PDF) of equivalent bubble diameter for each case. The equivalent bubble diameter is measured for all the bubbles in individual instantaneous flow fields (about 8000 fields in total) before the expansion. It is seen that the bubble size follows the Gaussian distribution for most of the cases considered, except the cases with a small mean equivalent diameter (>2.0mm) which follows a log-normal distribution.

2.2 Measurement techniques

2.2.1 Three-dimensional high-speed shadowgraph

To analyze the bubble dynamics three-dimensionally, we use a high-speed shadowgraphy technique with two high-speed cameras positioned perpendicular to

each other (Fig. 2.3a). Opposite to each camera, the plane LED panels (red colors, wavelength of 675 nm) are located as an illumination, by which the shadows of rising bubbles are captured by the cameras at the speed of 1000fps (576×2064 pixel resolution). Two cameras, equipped with a 50mm focal length lens are synchronized to capture the images of identical bubbles, which are further processed to calculate the gas-phase flow characteristics.

The image process methods such as particle extraction are explained in detail at section 2.2.2. Fig. 2.3(b) shows the typical bubble images obtained by two high-speed cameras. For each bubble at an instantaneous flow field, two images for the identical bubble reflected on x-z and y-z planes can be matched, while it has the same vertical (z) position. Using this pair of images, the three-dimensional information about the shape and center of each bubble is reconstructed. As shown in Fig. 2.3(c), along the vertical center axis, each horizontal cross-section of the bubble (1-pixel height) is assumed as an ellipse whose major and minor axis are evaluated from two planes (x-z and y-z planes) respectively (Hosokawa & Tomiyama, 2013). The shape and volume of each bubble are defined from the assumed ellipse series and used to detect the center and equivalent diameter of the bubble.

Once the center of each bubble is detected, its velocity is calculated based on the conventional particle tracking velocimetry algorithm. For the equivalent diameter, we calculate the diameter of the sphere which has the same volume as the reconstructed ellipsoidal bubble. The reconstructed bubble size information was used to define the mean volume void fraction of the inlet.

The uncertainty in bubble volume reconstruction measurement mainly comes from three sources: optical distortion at air-water-acrylic interfaces, bubble mask extraction algorithms, and volume 3D reconstruction method. Considering the thickness (10 mm) of the acrylic wall of the present test section, its effect on the optical distortion would be less than 4% (Fu & Liu, 2018). And the uncertainties from bubble mask extraction algorithms and volume 3D reconstruction method are estimated as 14% and 10% maximum, respectively. Thus, in overall, the uncertainty in bubble volume reconstruction measurement is estimated as about 15% (Fu & Liu, 2018). The statistical uncertainty of the present reconstruction shows less than 0.5% at the 95% confidence level in bubble size measurement for all experimental cases.

2.2.2 Two-phase particle image velocimetry (PIV)

To measure the liquid-phase flow statistics, we use the high-speed two-phase particle image velocimetry with one high-speed camera and two illuminations, as shown in Fig. 2.3d (Lindken & Merzkirch, 2002; Bröder & Sommerfeld, 2007; Kim et al. 2016, Lee & Park 2017). A high-speed camera (Phantom VEO 710, Vision Research) records both gas and liquid phase images produced from two illuminations of different wavelengths, and each phase is separately analyzed through a sequence of image processing.

A red-colored plane LED (wavelength of 675 nm) is used to make a shadow of a bubble, while a green-colored laser sheet (wavelength of 532 nm) from a continuous-wave laser (RayPower 5000, Dantec Dynamics) illuminates fluorescent seeding particles (PMMA-Rhodamine B, 2-20 μm in size) for liquid-phase measurement. To utilize the different wavelengths from two illuminations, an orange filter (high-pass cut-off wavelength of 520 nm) is equipped to a camera that captures the images at the speed of 500-1800 fps. Also, a mirror is precisely positioned at the opposite side of the laser to minimize data loss caused by the blocking of the laser sheet due to bubbles.

Finally, the bubble shadows and seeding particles of which the grayscale levels are different from each other and the background is clearly identified in the raw images (Fig. 2.4a). The measurements are done at the x-z plane (center plane of $y = 0$), and the field of view has the size of $-0.1 \leq x/D \leq 0.5$ and $-1 \leq z/D \leq 3.0$ (spatial resolution is about 7.7 - 18.4 % of the equivalent bubble size).

To separate gas and liquid phase information from the raw image (Fig.2.4a), we use a deep learning-based bubble segmentation algorithm (see section 3) and sequential image process algorithms for the gas and liquid-phase respectively. The deep learning-based algorithm directly applied to the raw image and extracted the bubble mask (Fig.2.4e). The bubble mask includes both in-focused and out-of-focused bubbles, and they should be distinguished from each other. To achieve this, a Sobel filter is applied to distinguish out-of-focused bubbles whose edge has a small gradient of grayscale levels compared to in-focused ones (Bröder & Sommerfeld,

2007; Pang & Wei, 2013). Finally, the center position and shape of the in-focused bubble are defined to calculate gas-phase statistics such as void fraction distribution, equivalent size, and distribution of bubbles.

For the liquid-phase images (Bröder & Sommerfeld, 2007; Pang & Wei, 2013; Kim et al., 2016), Laplacian of Gaussian (LoG) filter applied to the raw image (Fig. 2.4a) to detect the edges of both bubbles and seeding particles as shown in Fig. 2.4b, then a median filter is applied to LoG filtered image to figure out bubble edges only (Fig. 2.4c). The final seeding particle image (Fig. 2.4d) is obtained by subtracting the bubble edge from the LoG-filtered image.

Using the image of seeding particles, the liquid-phase velocity vectors are evaluated with the conventional cross-correlation algorithm (interrogation window of 32 × 32 pixels, and 75% and 75% overlap along the spanwise and streamwise directions, respectively). During the evaluation, the bubbles in each instantaneous flow field act like a moving mask, and velocity vectors inside the bubble were excluded from velocity field averaging, which is necessary to avoid having a non-physically large velocity gradient at the bubble surface. And we perform a convergence test with Reynolds stress which converges last among all variables during velocity field averaging.

As we have explained above, one of the advantages of the present two-phase particle image velocimetry technique is to measure the gas and liquid phases simultaneously. Thus, we have confirmed that the gas-phase flow characteristics such as mean void fraction, void distribution, and equivalent bubble size, measured from shadowgraph (three-dimensional) and two-phase particle image velocimetry (two-dimensional) are not different. Also, the tracer particle used in the present experiment is PMMA which has hydrophilic properties and is a hundred times smaller than the bubble, we can estimate that particle collision with the bubble is significantly low. (Farrokhpay et al., 2020)

During PIV measurement, it is known that the uncertainty is caused by several sources. The velocity vector U_{piv} evaluated from any grid-point of particle image can be calculated from $U_{piv} = M\Delta s/\Delta t$, where M is the pixel magnification factor, Δs is a particle image displacement, and Δt is a time difference. Then the total percentage

error ($\delta(U_{piv})$)in velocity measurement can be estimated by (Lawson et al., 1999):

$$\delta(U_{PIV}) = \sqrt{[\delta(M)]^2 + [\delta(\Delta s)]^2 + [\delta(\Delta t)]^2} \qquad (2.1)$$

From the images that were used to do calibration, the $\delta(M)$ was estimated as 0.1% with $M = 30$ μm/pixel. The percentage error in time difference $\delta(\Delta t)$ is estimated as 0.2% where the inter-frame time interval is 1 μsec. Lastly, the percentage error in particle image displacement $\delta(\Delta s)$ is 1.7% where the particle displacement resolution is about 0.1 pixel with an average particle displacement of 6 pixels. Thus, the estimated overall percentage error in the measurements is about 1.7%.

2.2.3 Bubble velocity measurement using optical flow

In the present two-phase particle image velocimetry, we measure the gas-phase velocity with an optical flow algorithm. The algorithm estimates the velocity field based on the change of the light intensity I which is assumed as constant between the two consecutive frames.

$$I(x + \delta x, y + \delta y, t + \delta t) = I(x, y, t) \qquad (2.2)$$

Applying first-order Taylor expansion to the left-hand side of equation (2.2)

$$I_x u + I_y v = -I_t \quad (I_x = \frac{\partial I}{\partial x}, \; I_y = \frac{\partial I}{\partial y}, I_t = \frac{\partial I}{\partial t}) \qquad (2.3)$$

Then each pixel p_i satisfies the equation (2.3), and if we consider a window of N x M pixels,

$$\begin{bmatrix} I_x(p_1) & I_y(p_1) \\ \vdots & \vdots \\ I_x(p_{N\times M}) & I_y(p_{N\times M}) \end{bmatrix} (u\ v) = - \begin{bmatrix} I_t(p_1) \\ \vdots \\ I_t(p_{N\times M}) \end{bmatrix} \qquad (2.4)$$

Using equation ([2.4](#)) and raw images ([Fig.2.4a](#)), we compute the bubble velocity field. Only the value inside the bubble is used for the time-averaged field.

Compare to the particle tracking velocimetry (PTV) algorithm, the optical flow algorithm has advantages that need no image pre-processing and could applied for the bubbly flow with high void fraction. It has been confirmed that the bubble velocity measurement using the optical flow algorithm can sufficiently replace the existing PTV algorithm under the void fraction conditions in the present experiment ([Choi et al., 2022](#)).
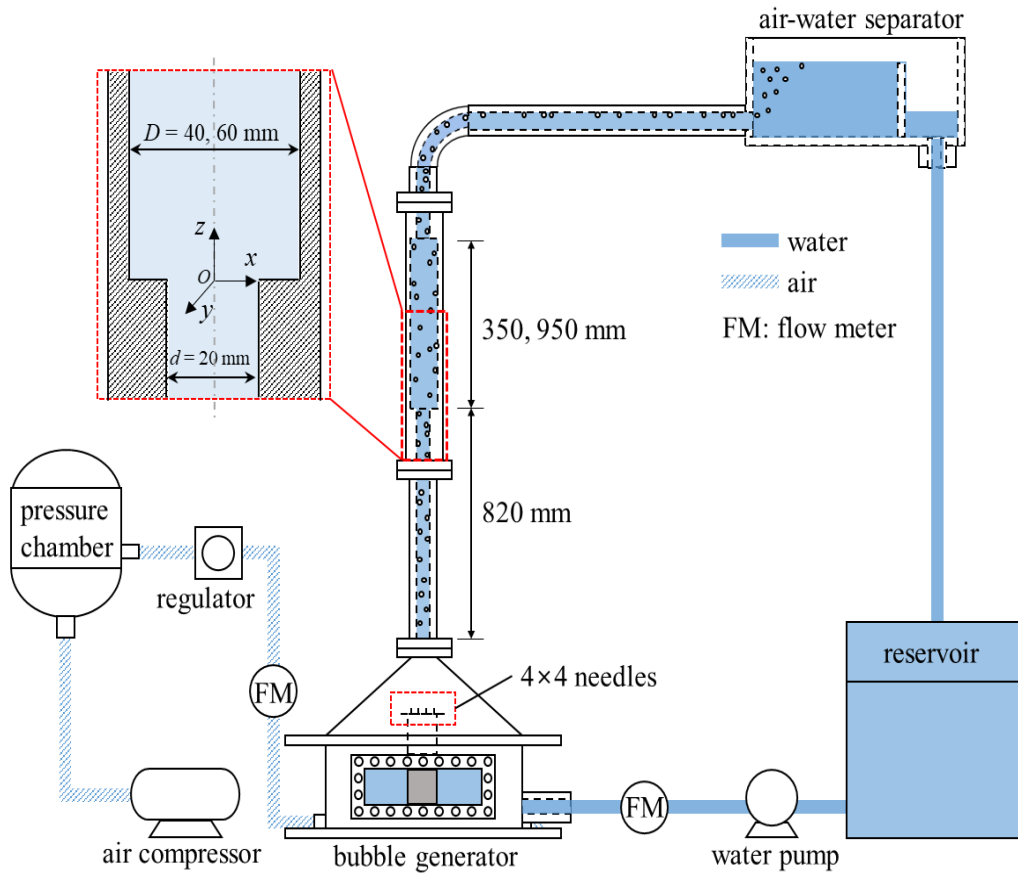
Fig. 2.1 Schematics for the air-water bubbly flows in an upward square pipe with a sudden expansion in cross section.

ER	Re	J_L [m/s]	J_G [m/s]	$\langle\overline{\alpha}\rangle$ [%]	$\langle\overline{d}_e\rangle$ [mm]	Re_b	We	Eo	AR
4	420	0.021	1.13×10^{-3}	0.29	2.12	530	1.87	0.61	1.66
			1.79×10^{-3}	0.39	2.41	590	2.03	0.79	1.68
			2.79×10^{-3}	0.63	2.80	770	2.95	1.07	1.77
	6000	0.302	2.08×10^{-3}	0.41	2.65	180	0.16	0.96	1.51
			4.04×10^{-3}	0.72	3.00	360	0.61	1.22	1.53
			6.38×10^{-3}	0.98	3.13	400	0.70	1.33	1.64
9	440	0.022	0.63×10^{-3}	0.30	1.62	230	0.44	0.36	1.23
			0.92×10^{-3}	0.39	1.79	250	0.50	0.48	1.28
			1.79×10^{-3}	0.69	2.29	360	0.80	0.71	1.4
			3.21×10^{-3}	1.13	2.84	470	1.09	1.09	1.57
			6.38×10^{-3}	2.01	3.39	550	1.25	1.57	1.74
			8.33×10^{-3}	2.80	3.56	560	1.23	1.73	1.78
	6000	0.300	0.38×10^{-3}	0.12	1.76	20	0.003	0.42	1.26
			0.96×10^{-3}	0.23	2.06	60	0.021	0.58	1.27
			2.08×10^{-3}	0.43	2.4	110	0.070	0.79	1.33
			4.04×10^{-3}	0.70	2.62	180	0.162	1.15	1.61
			6.38×10^{-3}	1.00	3.17	280	0.351	1.37	1.6
			8.04×10^{-3}	1.23	3.28	330	0.452	1.46	1.67
			12.50×10^{-3}	1.85	3.29	390	0.628	1.48	1.75

Table 2.1 Gas-phase condition for different liquid-phase expansion ration (*ER*) and Reynolds number (*Re*). J_L: liquid flow rate; J_G: gas flow rate; α: inlet volume void fraction, d_e: equivalent bubble diameter, Re_b: bubble Reynolds number, *We*: Weber number, *Eo*: Eotvos number, AR: bubble aspect ratio.
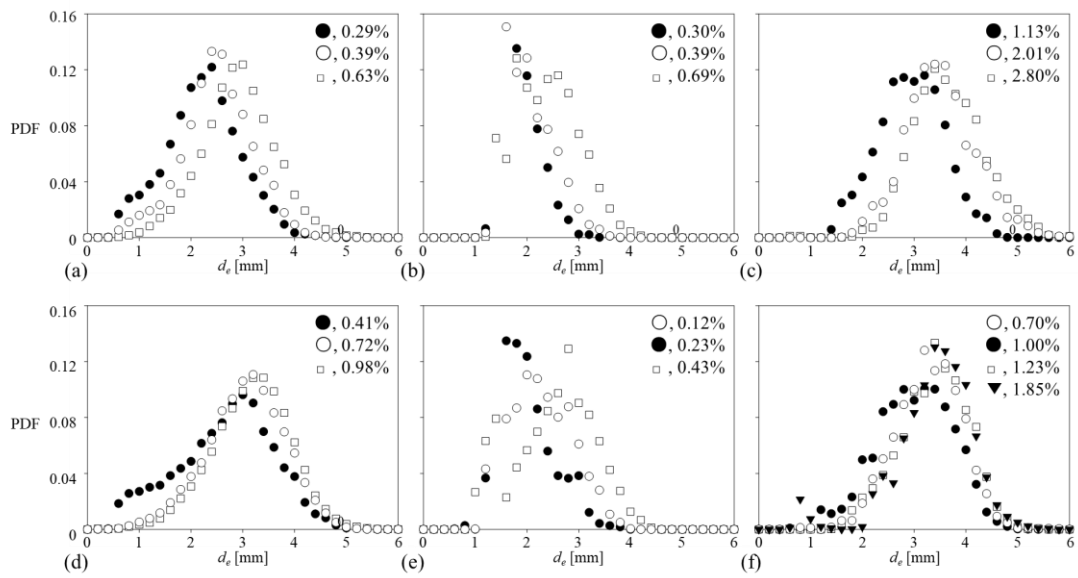
Fig. 2.2 Probability density function (PDF) of equivalent bubble diameter (d_e) for each void fraction (α) considered, measured at z/d = -1.0: (a) *Re, ER* = 420, 4.0; (b,c) 440, 9.0; (d) 6000, 4.0; (e,f) 6000, 9.0.
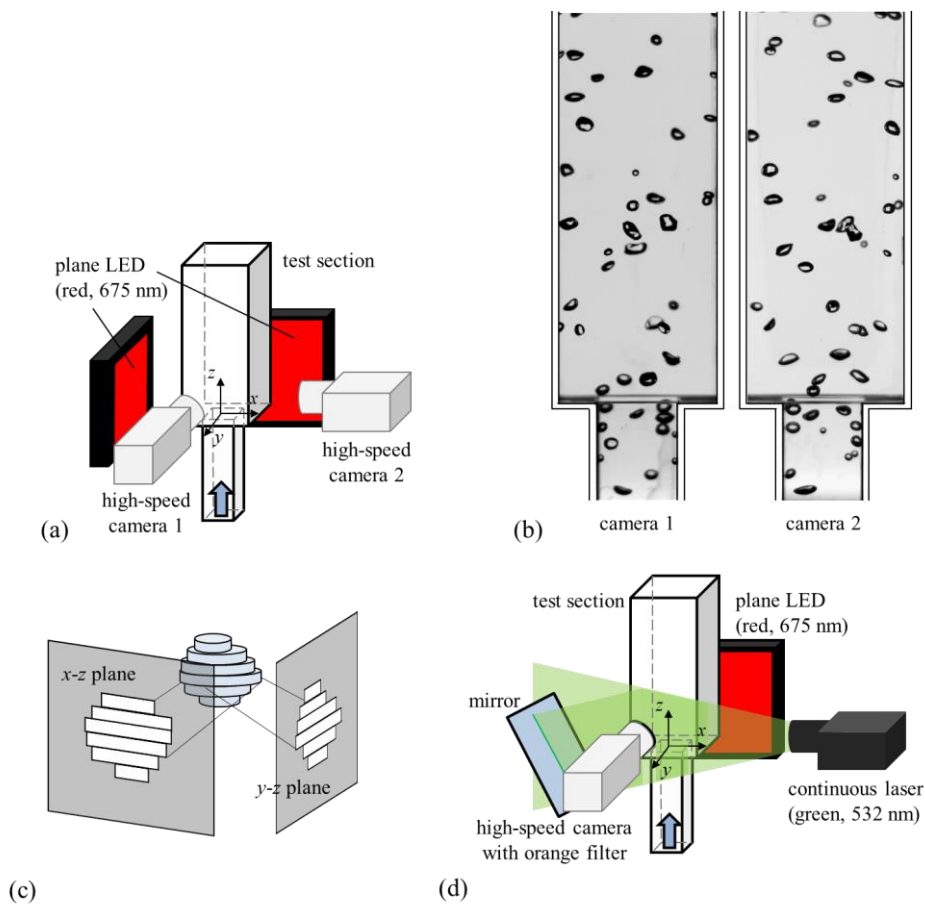
Fig. 2.3 Experimental setup: (a) optical arrangement for three-dimensional high-speed shadowgraph; (b) example of bubble images taken with two cameras in (a); (c) schematic of three-dimensional bubble reconstruction; (d) configuration of two-phase particle image velocimetry.
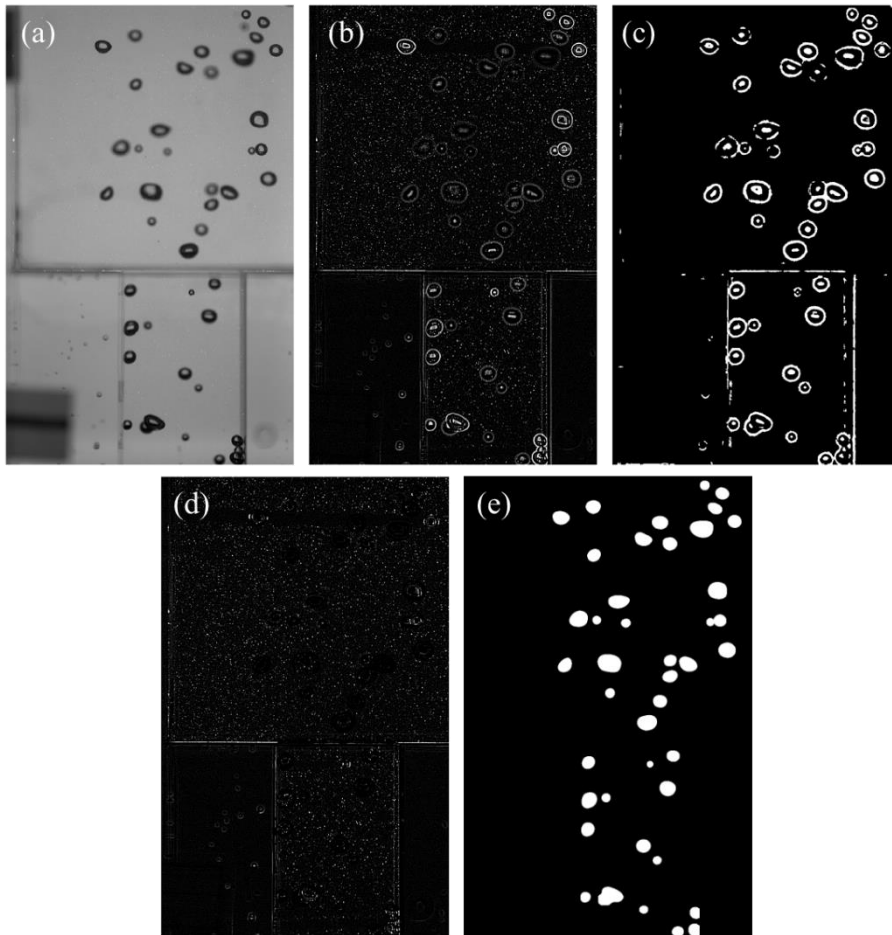
Fig. 2.4 Image processing to separate the liquid (d) and gas (e) phases from a raw image (a).

Chapter 3.

Deep learning-based bubble detection and mask extraction

The measurement techniques based on optical visualization are now ubiquitous approaches adopted in the experimental investigation of diverse problems from biological (small scale) to industrial (large scale) phenomena (Stephens & Allan, 2003; Xie, 2008; Chen et al., 2018; Moen et al., 2019). This is also true for the study of multiphase flows, where the simultaneous measurement of each phase over a large region of interest without disturbing the flow is quite advantageous (compared to the intrusive measurement methods) for understanding the interaction between phases.

In dealing with a gas-liquid two-phase (bubbly) flow, in particular, it is critical to measure the spatiotemporal variation of interfacial shape accurately to analyze the transport phenomena between phases (Kim et al., 2016; Alméras et al., 2017; Aoyama et al., 2017; Kim & Park, 2019; Lee & Park, 2020).

While detecting the bubbles from the optical visualization, the major obstacle is to identify and track individual bubbles (and statistics including the size and velocity) from the overlapped bubble cluster. As a tool to detect the bubbles against this challenge, numerous image processing techniques have been proposed such as the Hough transform (Hosokawa et al., 2009; Gordiychuk et al., 2016), breakpoint method (Fu & Liu, 2016; Zhong et al., 2016), and watershed transform (Lee & Park, 2020; Lau et al., 2013; Villegas et al., 2019). These methods have proven to be useful, but the application of a simple image processing filter is insufficient to process all images of bubbles with different geometrical features since the flow conditions and optical settings of each study are widely scattered. Even in a single image of a bubbly flow, bubble images have different characteristics that cannot be readily distinguished with a single process (criteria).

While tackling this issue, our group has established a reliable framework to detect bubbles in different types of bubbly flows with volume void fraction as high as 2%, by rigorously synthesizing digital image-processing algorithms (Kim et al.,

2016; Kim & Park, 2019; Lee & Park, 2020); however, the limitation of this approach is still existing. Most importantly, conventional methods require the optimization of coefficients or thresholds by the trial-and-error, and they are not universally applicable to various types of bubbly flow. Therefore, the accuracy of the detection largely varies depending on the skillfulness of the researcher, and the overall processing cost including human resources is very high.

In recent years, on the other hand, deep learning has been recognized as a powerful tool in the field of digital image processing and also has been proven to be promising in addressing the various problems in fluid mechanics (Stoecklein et al., 2017; Brunton et al, 2020; Jung et al., 2020; Kim & Lee, 2020; Park & Choi, 2020; Ye et al., 2020). They are finding ways to overcome the long-lasting problems by applying the deep learning-based methodology to solve governing equations or to improve experimental techniques, which were shown to enhance the model accuracy and save the overall data processing cost dominated by human resources.

In the experimental front of multiphase flow study, there have been recent attempts to detect objects (e.g., bubbles, droplets, and particles) by combining the deep learning model such as Faster R-CNN (Ren et al., 2015), an object detection model, with the conventional image processing in a gas-liquid two-phase flow (Oktay & Gurses, 2019; Cerqueira & Paladino, 2020; Hass et al., 2020; Li et al., 2020; Torisaki & Miwa, 2020; Poletaev et al., 2020; Chun-Yu et al., 2021).

Cerqueira & Paladino (2020) figured out the best-fitted ellipse of each candidate bubble by using the region proposal algorithm and CNN (convolution neural network), and Poletaev *et al*. (2020) found the center, axes, and orientation of each bubble in a bubbly jet flow using the autoencoder and CNN classifier. To understand the detailed interactions between each phase, however, it is important to know the exact shape (not just the bounding box or fitted ellipse) of the gas-liquid interface, which was not possible so far. As introduced, the aforementioned studies have a distinct limitation such that it is not feasible to obtain the actual bubble geometry under the shape instability (i.e., wobbling or deformation) caused by various flow conditions, since they considered a narrow range of bubble shapes (spherical or synthetic (artificially manipulated) ones). It is also noted that the test (validation) of the trained model with the untrained data is missing in most previous studies.

Therefore, in the present study, we develop and validate a fully automated tool to detect and extract the actual shape of the bubbles based on the deep-learning framework, which can be universally applied to various types of two-phase flows.

Here, we pay attention to the instance segmentation that extracts a pixel-wise segmentation mask of each detected instance, one of the representative challenges in the area of computer vision (He et al., 2017; Li et al., 2017). It has been actively adopted in the fields in which it is necessary to identify each instance under harsh conditions like having a higher level of noise or various image contrasts and colors. For example, many studies in biology or biotechnology need to identify each cell or tissue in a complex image (Caicedo et al., 2019; Ali et al., 2020; Cho et al., 2020; Moshkov et al., 2020).

We train the Mask R-CNN (He et al., 2017), one of the instance segmentation models, with the training data composed of bubbly flow data obtained experimentally from different conditions and synthetic bubble images. We optimize the amount and composition of training data from different sources and use a variety of image augmentation methods to achieve the optimal performance of the model.

Typically, the object detection model requires a huge amount of training data, but we were able to achieve a high detection performance with a relatively small amount of rigorously selected datasets. In addition, a customized loss function was used to improve the performance of detecting small bubbles, which is typically quite poorer than dealing with larger objects (He et al., 2017; Caicedo et al., 2019). As a result, we have obtained a fully automated bubble detection and mask extraction tool that works quite well in different gas-liquid bubbly flows without a manual tuning of thresholds. We hope this will be useful in easing the difficulties in evaluating the optical images of multiple objects interacting in a complex manner.

3.1 Data acquisition and optimization

As a training dataset, we used both experimental and synthetic bubbly flow images obtained from the upward bubbly flows in an expansion pipe (Kim & Park, 2019) and the BubGAN algorithm (Fu & Liu, 2019), respectively (Table 3.1). Experimental bubbly flow data includes the bubbles whose size range is 7-98 pixels

(0.25-3.4 mm in physical scale) and their volume void fraction is 0.72%. As shown in Table 3.1, we obtained data by two different techniques of two-phase particle image velocimetry (PIV) and shadowgraph.

While the shadowgraph visualizes the bubble shadow only, the two-phase PIV measures the liquid-phase velocity as well as the bubble statistics (shadows). Thus, the images from the two-phase PIV were added to the training dataset to make the model robust to the environments, in which the optical image has a significant level of noise (represented by seeding particle images). Also, the training dataset would be benefited from the fact that the distribution of gray levels in the image is different depending on the optical setup (Kim & Park, 2019; Lee & Park, 2020).

Since one of our primary goals is to improve the performance of dissembling the overlapped bubbles, the conditions possibly missing in the experimental dataset can be supplemented by the synthetic dataset in which the size and distribution of bubbles are controlled. For the data produced by the BubGAN, the bubble size was varied as 4-123 pixels, and the intersection over union between two bounding boxes (of each bubble) was set as $IoU_B = 0.11$, 0.16, and 0.2. A much higher value of IoU_B causes negative effects such that the dense bubble population would lead to an excessive split of bubbles. Here, the intersection over union indicates the ratio of overlapping area between two objects to the union area. The void fraction of the synthetic dataset was set to be 3.0-8.0%.

To add the bubbles smaller than the average size (35 pixels in diameter), on the other hand, the height of the image with $IoU_B = 0.16$ was adjusted to be three times longer than other cases ($IoU_B = 0.11$ and 0.2) because all training inputs are scaled into the same size (640×640 pixels) regardless of the physical size of the image.

While some of the images from the same experimental conditions as the training dataset are used to evaluate the model, we also added the experimental data of bubble-swarm flow (Lee & Park, 2020) to the test dataset, which is not included in the training set (Table 3.1). The bubble size range in the bubble-swarm flow data in the test set is 7-65 pixels (0.6-5.2 mm) with a volume void fraction of 0.3-2.0%. For all experimental images in the training and test datasets, the overlapped bubbles that are difficult to obtain the exact separated mask (ground truth) were removed to avoid detrimental effects on the model. The conditions of training and test datasets are

summarized in Table 3.1.

In general, a model trained with more data would perform better, but there is a practical limit to the amount (and quality, as well) of data that can be obtained from the experiments. Therefore, we need to optimize the composition of the training dataset, and we run through several experiments to determine the optimal condition. That is, two models were trained for the same iterations, while the first one is trained only with the experimental data and the second one with the synthetic data only. Then, they were evaluated with the same test dataset: 30% from the upward bubbly flow in an expansion pipe, 45% from the synthetic bubble images, and 25% from the bubble-swarm flow. The model trained with the synthetic data only showed half the accuracy (AP_{50}, average precision for the cases of IoU $\geq$ 0.5) of the model trained only with the experimental data, indicating that the model trained with the synthetic dataset only (even though its size is huge) does not provide the desired performance.

The experimental data play a critical role in transferring the power to recognize the actual bubble shapes under various conditions. By adding synthetic bubble images to the training set of the experimental data, it was enhanced to dissemble the overlapped bubbles. Moreover, we found that the accuracy (AP_{50}) slightly increases, if the training dataset includes the experimental images without brightness gradient inside the bubble shadows, i.e., if all the bubbles are filled with black color. The optimized composition of the training and test dataset is shown in Table 3.1.

For the training and evaluation of the model, we need raw images of bubbles with ground truth masks for each bubble. We followed the conventional image processing method for optical gas-liquid two-phase flow experiments that our group has established (Kim et al., 2016; Kim & Park, 2019; Lee & Park, 2020) to create the ground truth mask of the experimental images. First, the images are binarized by median filter and Sauvola binarization (Sauvola & Pietikäinen, 2000), then the bright bubble core is filled via the morphological image reconstruction algorithm (Soille, 2013) and denoised by a size filter (Kim et al., 2016). Next, each object in the binarized image was determined whether it is overlapped bubble cluster or a solitary bubble using a roundness criterion (Lau et al., 2013) based on the relationship between the perimeter and area of the bubble.

After the overlapped bubble clusters are determined, they were removed from both raw and binarized images by the in-house MATLAB code. If any overlapped bubble cluster indistinguishable by a roundness criterion remains, it is also removed manually using the MATLAB GUI tool. As a result, we get bubble images with only a solitary bubble and a binary mask for each bubble in the image.

3.2 Training and evaluation

Mask R-CNN is an instance segmentation model that labels each pixel corresponding to each instance detected by adding a parallel mask branch to Faster R-CNN, one of the widely used object detection models. In this study, we used Matterport Mask R-CNN implementation (https://github.com/matterport/Mask_RCNN), using ResNet-101 as the backbone, and applied transfer learning from pre-trained COCO weights (https://github.com/matterport/Mask_RCNN/releases/download/v2.0/mask_rcnn_c oco.h5) to maximize the data efficiency and delay the overfitting.

The model was trained for 24 epochs using a batch size 1, with an initial learning rate of 10^{-4}, which we optimized for our computing environment using a grid search (from 10^{-2} to 10^{-5}), while decreasing it by a factor of 10 after every 10 epochs. From the entire model, only the ResNet stage 5 and the head layer were re-trained, by which it was empirically shown that the highest accuracy is achieved before the occurrence of overfitting, compared to the selection of other layers to be trained. Also, to slow down the overfitting, we applied several image augmentations, such as a flip, rotation, and Gaussian noise addition, randomly to the training input image at each iteration. For the training, ADAM was chosen as an optimizer and the regularization weight decay value was set as 10^{-4}. The training was conducted on a single NVIDIA RTX 2080 Ti GPU.

In general, large objects in the image have a dominant influence on the training loss of the object detection model (He et al., 2017; Caicedo et al., 2019), and thus the accuracy of detecting smaller objects tends to be low. In the case of bubble detection problem, however, the detection accuracy of small bubbles is as much important as that of large bubbles, because the bubble size follows a Gaussian

distribution in a typical gas-liquid two-phase flows, and their scale-wise interactions are physically very important in studying the transport phenomenon (Kim et al., 2016; Kim & Park, 2019; Lee & Park, 2020). Therefore, we improved the mask accuracy of small bubbles by using a customized loss function that flattens the effect of bubble size on the loss by weighting the loss according to the bubble size.

To increase the model accuracy for small bubbles as much as that for large bubbles, we apply the weight factor to the loss function, to increase the contribution of small bubbles on training losses (smooth L1 loss, equation (3.1)).

$$\text{smooth}(x) = \left(\frac{\text{size}^{-1} - \text{size}_{\text{max}}^{-1}}{\text{size}_{\text{min}}^{-1} - \text{size}_{\text{max}}^{-1}} - 0.5 \right) w + 1 \qquad (3.1)$$

The customized weights are given by equation (3.2), where *size* denotes the bubble equivalent diameter (d_e), and *w* is the weight effect factor, which is 0.3 in the present study.

$$\text{Global weight} = \left(\frac{\text{size}^{-1} - \text{size}_{\text{max}}^{-1}}{\text{size}_{\text{min}}^{-1} - \text{size}_{\text{max}}^{-1}} - 0.5 \right) w + 1 \qquad (3.2)$$

To apply the global weights to the loss function rather than the local weights, which only work on each iteration (image), the minimum and maximum bubble sizes of all the bubbles in the training set are used. During this, we have empirically found that weighting only small bubbles is more effective than weighting small and large bubbles.

As a result, the mask accuracy of small bubbles (AP_S) increased by approximately 4%, and the overall accuracy (AP_{50}) slightly increased together (the definitions of AP_x are provided in the next section). More configuration details can be found in our code, which is available online (https://github.com/ywflow/BubMask).

The performance of the model was evaluated by calculating the mask average precision (AP) for each mask intersection over union (IoU) threshold and object size

range, following the COCO evaluation metrics (https://cocodataset.org/#detection-eval). The evaluation metrics we have used include AP (averaged over IoU thresholds 0.5 to 0.95 with 0.05 intervals), AP_{50} (for IoU $\geq$ 0.5), and AP_{75} (IoU $\geq$ 0.75) according to the IoU threshold, and AP_S, AP_M, and AP_L according to the bubble size of the test dataset. Here, the subscript refers to the IoU threshold in percentage or the size range of the bubble. The ranges of bubble size (d_b) for the AP_S, AP_M, and AP_L were determined by classifying all bubbles in the test dataset by $d_b < 22.6$ pixels (small), 22.6 pixels $\leq d_b < 39.5$ pixels (medium), and $d_b > 39.5$ pixels (large), respectively, and they cover 36%, 38% and 26% of the number of whole bubbles tested. This ratio was determined intentionally to quantitatively evaluate the effect of the customized loss function on the model performance, especially in detecting small bubbles.

It is noted that each kind of AP for each image was averaged over all corresponding images in the test dataset, not from a single test while maintaining the same number of images for all types of data. This is because the accuracy of each image is also important to confirm the universality of the present model that works in various complex two-phase flows; as mentioned above, each test image has a different level of bubble density, bubble locations, image background, and lighting conditions, which sorely requires the development of a universal model.

3.3 Results

3.3.1 Averaged precision (AP)

Fig. 3.1 shows the accuracy (averaged precision, AP) of the present model depending on the IoU threshold value and object size range, evaluated by three test datasets of set #1, set #2, and set #3. Each test set includes the entire test images, images from similar experimental conditions to the training set(Kim & Park, 2019; Fu & Liu, 2019), and images of different experimental conditions (Lee & Park, 2020) from the training dataset, respectively (see Table 3.1).

The present model shows a high accuracy not only for test set #2 with similar experimental conditions as the training set, but also for set #3 that were not included

in the training set. While the accuracy difference among the test sets is not substantial in general, the AP_S differs relatively larger between test sets #2 and #3. This is because set #2 contains relatively more small bubbles compared to set #3. Even if the magnitude of the mask difference between the ground truth and the detected mask is the same as that of the large bubbles, the IoU is largely reduced for small bubbles, resulting in a significant decrease in the accuracy of detection.

The representative results of bubble edge (mask) detection by the present model (for IoU threshold of 0.5) are shown in Fig. 3.2. It is clear that the detected bubble shapes follow the actual bubble shadows quite well. Based on the results shown in Figs.3.1 and 3.2, we think it is reasonable to represent the performance of the present model based on AP_{50}, because the difference between AP_{50} and AP_{75} is quite small, and the IoU between the ground truth and predicted mask would increase due to human errors involved in the process of labeling the ground truth mask (bubble edge). The AP_{50} for the entire test dataset (set #1) of the present model is 0.981 (it is 0.997 for set #3), which is a quite promising bubble edge detection performance.

3.3.2 Model performance under various flow conditions

In this section, we have assessed the performance of the present model in several ways to confirm that it works well under a wide range of experimental and/or flow conditions. First, we analyze the dependency on the volume void fraction ($\langle \bar{\alpha} \rangle$) of the model performance, which is one of the most important parameters to characterize the physics of bubbly flows.

In Fig. 3.3 (a), we plotted the variation of AP_{50} and AP_{75} depending on the void fraction. Since correct answers (separated bubble edges) for overlapped bubbles are required for a fair evaluation, the evaluation was done using the synthetic bubble images; the results of 50 synthetic images were averaged for each void fraction. As expected, the accuracy tends to decrease as the void fraction increases, and AP_{50} and AP_{75} become 0.567 and 0.463, respectively when the void fraction increases to 5%. Considering that the typical maximum void fraction considered in the experimental studies on the bubbly flows using the optical measurement is approximately 2-3% (mostly below 1%) (Schlegel et al., 2009; Hosokawa & Tomiyama, 2013; Kim et al.,

2016), the AP_{50} is higher than 0.71-0.8 (0.9 for void fraction below 1%), which is acceptable performance. On the other hand, some representative result images for each void fraction are shown in Figs. 3.3(b)-(f), which qualitatively demonstrates the operating range and performance of the present model.

Next, we test the model with the actual experimental data of bubble-swarm flow[9], which include a larger number of overlapped bubbles than the images used in the training dataset, to find out how well the present model works in the two-phase flows with a moderate void fraction (up to approximately 2%).

Unlike the synthetic images, it is not feasible to obtain the exact individual shape from all overlapped bubbles in this case, thus the ratio of the number of bubbles detected by the model to that of total bubbles was calculated depending on the volume void fraction (Fig. 3.4a). Here, the results of 10 images were averaged for each corresponding void fraction, and the representative result images were also shown to judge qualitatively the operating range and performance of the present model (Figs. 3.4b-f).

As shown, more than 92% of the bubbles were detected for the void fractions up to 1%. The loss of detection slowly increases as the void fraction increases; however, still, more than 87% of the bubbles are detected (within 5% standard deviation) even for the intermediate void fraction of 2%. As shown in Fig. 3.4(f), the bubbles are severely overlapped even with the void fraction of 2%. The capability of the present model to identify individual bubbles with corresponding masks among the overlapped bubbles is well demonstrated in bubble clusters without a clear bright core (highlighted with dashed boxes in Figs. 3.4e, f). It is noted that some of the image processing algorithms, introduced at the beginning, use the bright spot inside the bubble shadow to distinguish the individual bubble from the cluster.

Finally, we have shown the results of bubble detection and mask extraction achieved by the present model for different types of gas-liquid two-phase flows (Fig. 3.5), of which the visualization data came from our group (published and unpublished data). Tested two-phase flow includes the bubble plume (Fig. 3.5a, unpublished), bubbly flow in a rod-bundle geometry in a nuclear power plant (Fig. 3.5b, unpublished), pool boiling bubble (Fig. 3.5c, Kim & Park, 2022), bubble-swarm flow (Fig. 3.5d, Lee & Park, 2020), and upward bubbly flow in an expansion

pipe (Fig. 3.5e, Kim & Park, 2019). It is noted that these data were not included in the both training and test dataset.

As shown, it is qualitatively demonstrated that the present model can be universally applied to diverse two-phase flows, to detect and extract the individual bubble in the flow. It is also promising to see that the bubbles in the interaction with the solid wall such as adhesion, bouncing, and sliding can be also detected (Figs. 3.5b, c, and e).

3.3.3 Reduce the time required for mask extraction

When processing the optically obtained experimental data, computational speed is also an important issue as its accuracy. Since the conventional multiple-filter image processing technique is now replaced with the convolutional layers in the present model, it is expected that the time required for mask extraction would be reduced. When we use the same computing resources to test the same images, the calculation time of the present model is 2 - 3 times shorter than that taken by the conventional method. It is noted that the bubble mask extracted by the present model is at least equivalent to or better than the result from conventional image processing (Fig. 3.5).

Fig. 3.6 shows an example of the extraction of bubble masks and a time-cost comparison between the present model and the conventional method. Here, the bubble-swarm flow (Lee & Park, 2020) of 0.9% void fraction is compared, and the Watershed transform was applied twice repeatedly as a conventional method. As shown, the extracted bubble masks are equivalent to each other but the time cost (averaged for 10 images) significantly decreased to 4.4 seconds from 14 seconds taken by the Watershed transform.
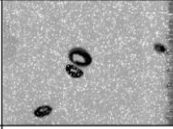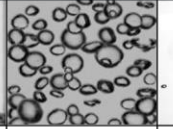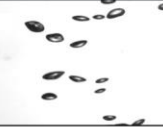
Source of data		Expansion pipe bubbly flow (Kim & Park, 2019)		BubGAN (Fu & Liu, 2019)	Bubble swarm (Lee & Park, 2020)
		2-phase PIV	Shadowgraph		
Sample image					
Resolution		736 ×1120	576 ×1032	200 × 300 100 × 900	624 × 976
Bubble size [pixels]		7–98 (46.8)	10–60 (31.4)	4–123 (34.0)	7–65 (28.3)
$\langle \bar{\alpha} \rangle$ [%]		0.72	0.72	3.0–8.0	0.3–2.0
Training set	# of images	1588	854	150	-
	# of bubbles	8160	14640	15280	-
Test set	# of images	8	8	8	8
	# of bubbles	40	120	770	330

Table 3.1 Data details for training and test set. Sample images were cropped from original images and scaled for better visibility. The numbers in the bracket denote the averaged bubble size. $\langle \bar{\alpha} \rangle$: volumetric void fraction
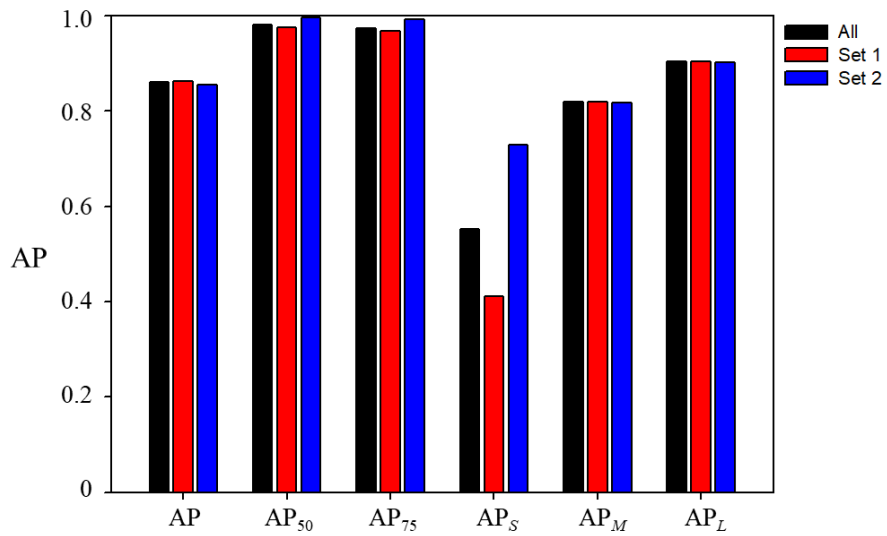
Fig. 3.1 Mask AP based on IoU threshold and object size range. set #1: all test dataset in Table 3.1, set #2: images with similar experimental conditions to the training set (Kim & Park, 2019; Fu & Liu, 2019), set #3: images with different experimental conditions than the training dataset (Lee & Park, 2020)
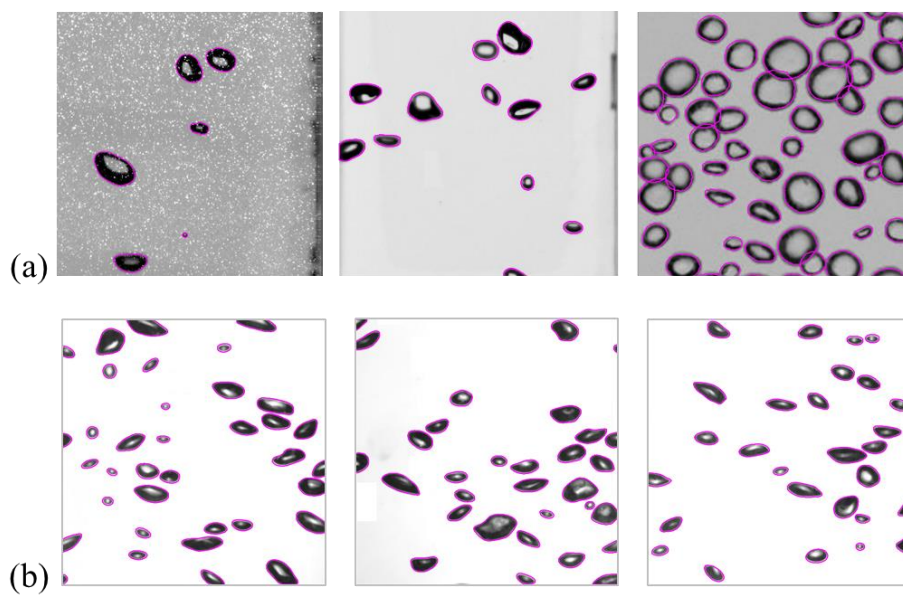
Fig. 3.2 Bubble detection examples (IoU threshold of 0.5) for (a) test set #2 and (b) #3. Here, the solid purple lines represents the extracted bubble shapes, and the images were cropped from original images and scaled for better visibility.

(a)

(b)　　　(c)　　　(d)

(e)　　　(f)
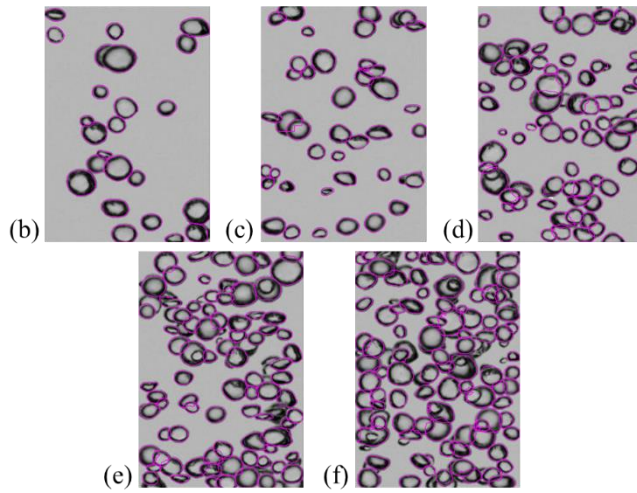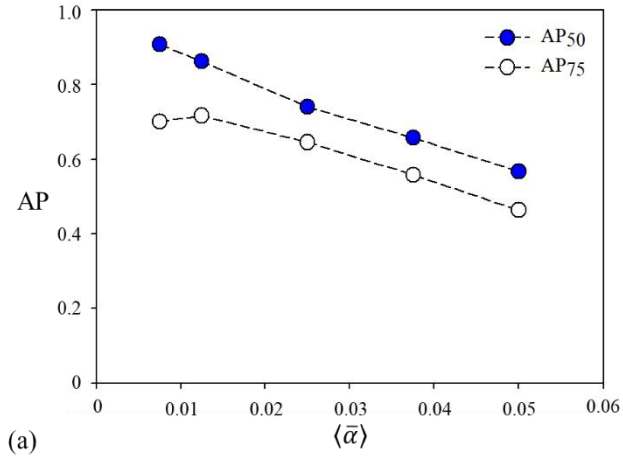
Fig. 3.3 (a) Variation of AP_{50} and AP_{75} of synthetic images with volume void fraction $\langle \bar{\alpha} \rangle$. Representative bubble images with detection results (purple solid lines) are shown for $\langle \bar{\alpha} \rangle$ of (b) 0.0075; (c) 0.0125; (d) 0.0250; (e) 0.0375; (f) 0.0500.
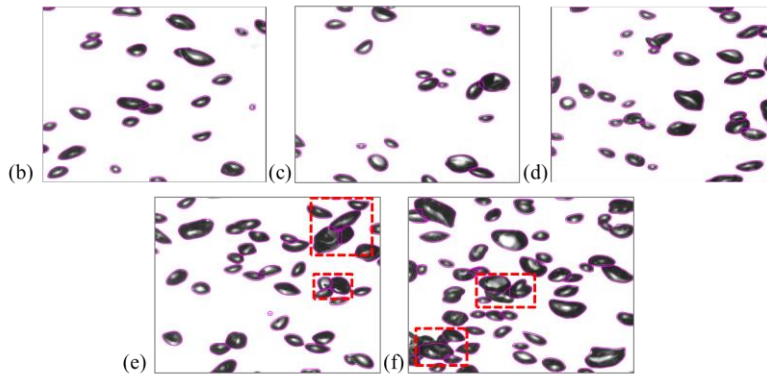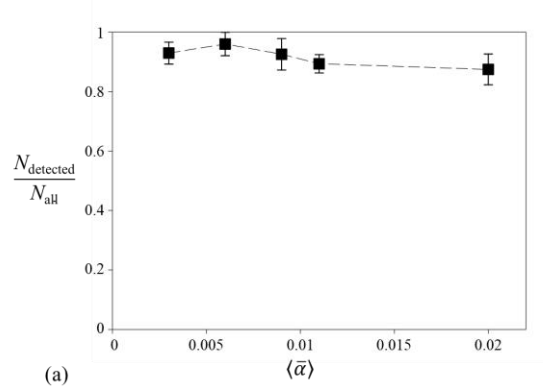
Fig. 3.4 (a) Ratio of the number of detected bubbles ($N_{detected}$) to the total number of bubbles in the bubble-swarm flow images (Lee & Park 2020) with volume void fraction $\langle \bar{\alpha} \rangle$. Representative bubble images with detection results (purple solid lines) are shown for $\langle \bar{\alpha} \rangle$ of (b) 0.003; (c) 0.006; (d) 0.009; (e) 0.011; (f) 0.02.
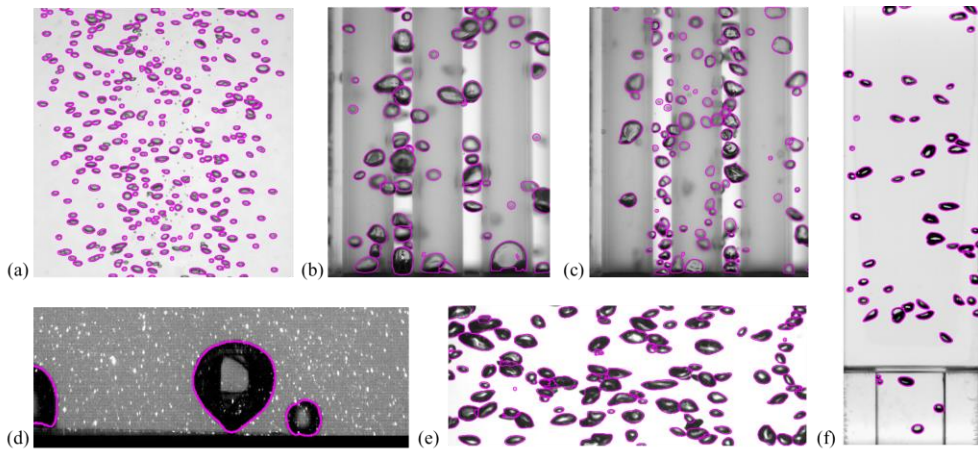
Fig. 3.5 Bubble detection and mask extraction results for various gas-liquid two-phase flow experiments: (a) bubble plume; (b) rod bundle without background flow; (c) rod bundle with background flow; (d) pool boiling; (e) bubble swarm; (f) expansion pipe.
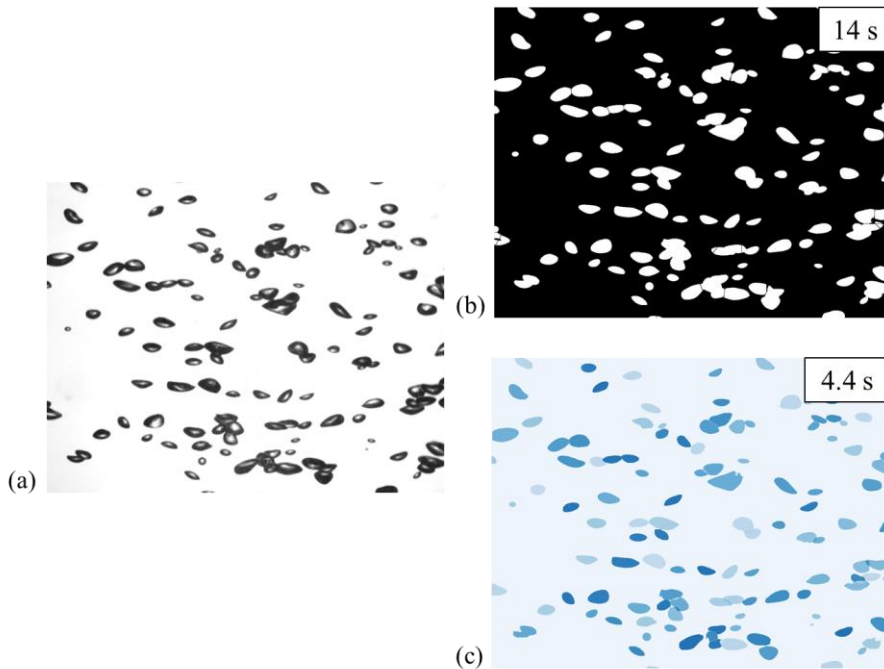
Fig. 3.6 Example of the comparison of mask extraction and corresponding time consumption: (a) raw image; (b) conventional image processing result; (c) present model result. The image was obtained from the bubble-swarm experiment with void fraction of 0.9% (Lee & Park 2020) and has a resolution of 1248×976 pixels.

Chapter 4.

Bubble dynamics in a square pipe with a sudden expansion

4.1 Bubble lateral migration

Bubble trajectories and there size contour for $ER = 4.0$ are shown in Fig. 4.1. In the present experiments, bubbles rise through a three-dimensional path (Fig. 4.2 and 4.3), but the figures are drawn in the x-z plane to confirm a clear relation between the size of each bubble and its tendency of lateral movement. As expected, present bubbles rise in oscillating paths and the alternating nature of lateral movement is maintained after the expansion ($z/D > 0$).

In laminar flow (Fig. 4.1a), bubbles tend to move in the core region of the pipe and spread to the wall as they rise after the expansion without any specific trends in bubble size. Even if the background flow is weak, it is understood that the bubble-induced flow sets up a mean velocity gradient that is strong enough to force the lateral migration of rising bubbles.

However, in turbulent flow (Fig. 4.1c, 4.1d), most of the bubbles rise in the wall region and show a clear tendency regarding bubble size, large bubble moves to the core region more frequently than small one. As Re increases, on the other hand, the streamwise distance where bubbles attach to the wall after the expansion becomes shorter; for example, it is $z/D \simeq 0.5$ and 0.4 for the cases of Fig. 4.1(a) and 4.1(c), respectively. The wavelength (i.e., period) of the oscillating bubble path is also reduced as Re increases. This is because the liquid-phase velocity gradient becomes stronger and thus the contribution of shear-induced lift force increases (see Section 5.4).

When the mean void fraction increases, bubbles in laminar flow show the same bubble size effect as turbulent flow (Fig. 4.1a, 4.1b) because the bubble size PDF shift to the right (Fig. 2.2a) (i.e., the number of larger bubble increases) and has a similar range to turbulent flow PDF (Fig. 2.2d). As the flow develops after the expansion, bubbles reattach to the wall faster at higher background flow rates, for

example, in turbulent flow, bubbles reattach to the wall earlier than laminar flow (Fig. 4.1a, 4.1c).

In the case of *ER* 4.0, most of the bubbles are migrated toward the core in laminar flow regardless of the size of the bubbles, and in the case of turbulent flow, large bubbles are migrated toward the core, and small bubbles are migrated toward the wall as a result of hydrodynamic force applied to the bubbles. To ensure that migration trends in *ER* 4.0 are maintained in *ER* 9.0, time-averaged bubble size distribution along the streamwise direction (z/D = -1.0 − 3.0) for the cases of (Re, $\langle \bar{\alpha} \rangle$, ER) = (420, 0.39%, 4.0), (440, 0.39%, 9.0), (6000, 0.72%, 4.0), and (6000, 0.7%, 9.0) is shown in Fig 4.4.

The bubble size distribution of *ER* 4.0 (Fig. 4.4a, 4.4c) was consistent with the results confirmed in Fig 4.1. Meanwhile, in the case of *ER* 9.0, both laminar flow (Fig. 4.4b) and turbulent flow (Fig. 4.4d) showed bubble size peaks near the wall, in particular, in laminar flow, the bubble size increased near the wall than the core. A few previous studies reported similar qualitative descriptions about the bubble size effect on the bubble movement across the expansion channel (Voutsinas et al., 2009; Pakhomov & Terekhov, 2016), but quantitative analysis to understand the cause of this phenomenon is not sufficient. Therefore, we analyze the hydrodynamic forces acting on the bubble in §5.4 to figure out why this occurs.

Fig. 4.5 shows the lateral distribution of planar void fraction along the streamwise direction (z/D = -1.0 − 3.0) for the cases of (Re, $\langle \bar{\alpha} \rangle$, ER) = (420, 0.39%, 4.0), (440, 0.39%, 9.0), (6000, 0.72%, 4.0) and (6000, 0.7%, 9.0). In general, it is found that the inlet void distribution is recovered faster after the expansion as Re increases.

As shown above, the bubbles show a core-peaking (or intermediate-peaking) void distribution at the inlet for the laminar flow, which is maintained after the expansion. As the flow develops, the void peak at the core is broadened laterally faster in ER = 4.0 compared to ER = 9.0, while its amplitude is slightly reduced due to bubble dispersion (Fig. 4.5a). Therefore, the position of the maximum lateral gradient of void distribution ($\partial \bar{\alpha} / \partial x$) moves from the separation edge ($x/D \simeq 0.25$) to the wall ($x/D \simeq 0.5$) .

For the turbulent flow, the void distribution becomes quite different as it shows

a wall-peaking condition at the inlet (Figs. 4.5c, 4.5d). Due to the sudden deceleration of the flow at the expansion, the void distribution is disturbed and flattens out at $z/D \simeq 0 - 0.75$ and $0 - 4.5$ for $ER = 4.0$ and 9.0 each, but it recovers the original wall-peaking distribution quickly at $z/D \simeq 1.0$ and 2.0 as the separated flow re-develops along the streamwise direction. Thus, the position of the void peak is located near the wall except at $z/D \simeq 0 - 0.75$ for $ER = 4.0$ and $0 - 1.5$ for $ER = 9.0$. Due to its larger cross-sectional area after expansion, ER 9.0 takes more time to redistribute to the wall void peak compared to ER 4.0, and the void fraction in the core region decreases rapidly compared to ER = 4.0 immediately after expansion. Figs. 4.8 and 4.9 shows three-dimensional void fraction distribution and describe well the void fraction re-distribution after the expansion between laminar and turbulent flow.

4.2 Bubble velocity distribution

Time-averaged bubble velocity profiles along the streamwise and lateral directions for the cases of Fig. 4.5 are shown in Fig. 4.6 and 4.7. Here, the velocities in streamwise and lateral directions, normalized by the bulk velocity (u_{bulk}) of a corresponding single-phase flow, are shown separately. Despite the difference in the void distribution, the overall shape of the bubble velocity profile is similar for both Re's, and the lateral velocity is smaller (below 25%) than the rise velocity. Bubble rise velocity shows a quite broad peak at the core before and after the expansion, and it decreases gradually toward the wall region (Fig. 4.6). Interestingly, the rise velocity ($u_{z,b}$) remains nearly constant in the lateral direction after expansion for laminar flow, but for $Re = 6000$, the velocity near the wall decreases gradually after the expansion which is the effects of liquid flow deceleration due to volumetric expansion.

In laminar flow, the bubble rise velocity is much faster than the liquid-phase bulk velocity and thus the deceleration of the flow due to expansion seems less affect the bubble rise velocity. While the individual bubble follows a vigorous lateral oscillatory motion, due to its periodic nature, time-averaged lateral velocity is almost zero (Fig. 4.7). However, sudden growth and collapse of lateral bubble velocity

(toward the wall) are induced at z/D $\simeq$ 0 − 1.5 (*ER* = 4.0, Fig. 4.7a) and z/D $\simeq$ 0 − 2.5 (*ER* = 9.0, Fig. 4.7b) for laminar flow, and z/D $\simeq$ 0 – 1.0 (*ER* = 4.0, Fig. 4.7a) and z/D $\simeq$ 0 – 0.75 (*ER* = 9.0, Fig. 4.7b) for turbulent flow, respectively. Bubbles reattach to the wall faster in turbulent flow than in laminar flow, reach the wall faster at *ER* 4.0 than at 9.0 in laminar flow, and faster at *ER* 9.0 than at 4.0 in turbulent flow. It can be inferred that the development rate of the shear layer is different from each other through the change in the lateral velocity of the bubbles. The location of maximum $\bar{u}_{x,b}$ moves toward the wall along the z-direction, which agrees with the evolution of void distribution (Fig. 4.5).
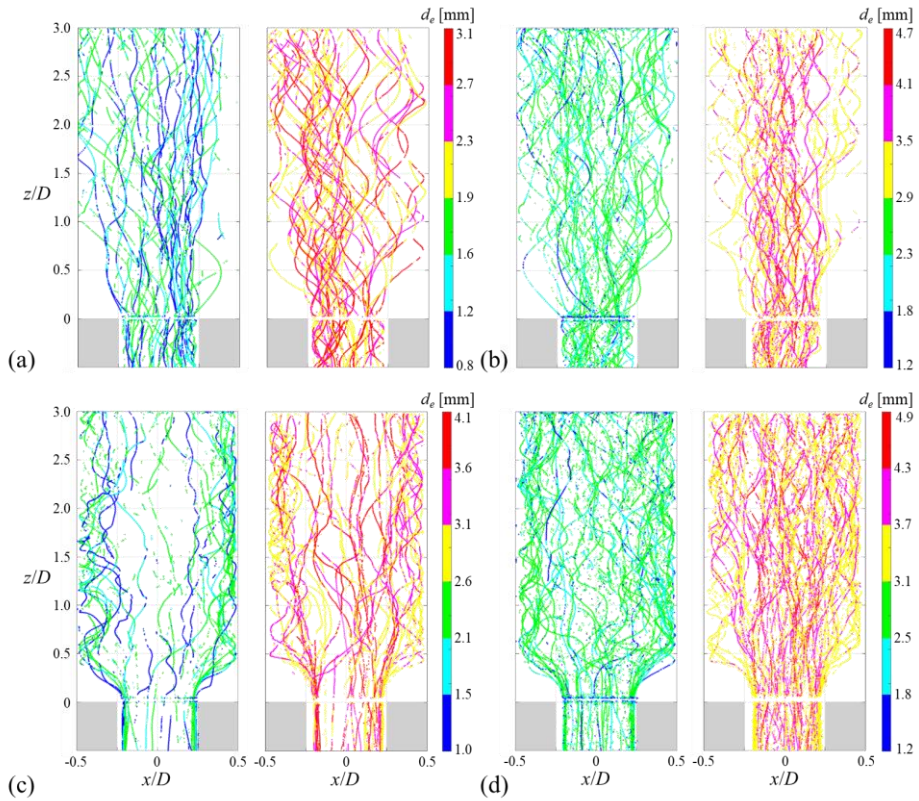
Fig. 4.1 Bubble trajectories across the expanded square pipe ($ER = 4$) at (a) Re, $\langle \bar{\alpha} \rangle = 420$, 0.29%; (b) 420, 0.63%; (c) 6000, 0.41%; (d) 6000, 0.98%. The line colors of each trajectory denote the corresponding range of bubble size (d_e), and the left and right panels of each sub-figure are allotted for smaller and larger bubbles, respectively, for the purpose of enhanced visibility.
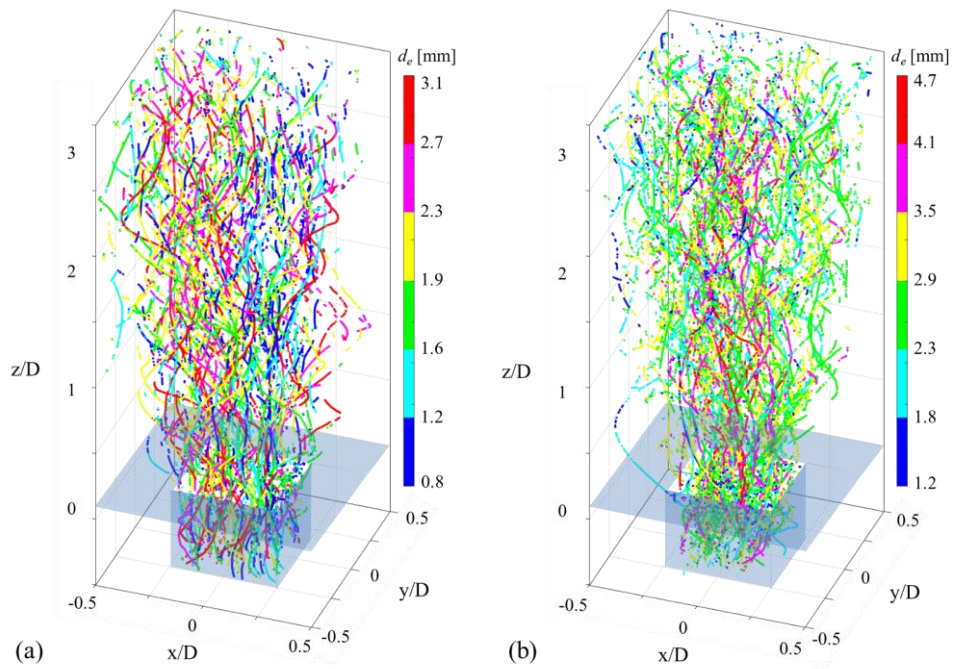
Fig. 4.2 3D bubble trajectories with bubble size contour for Re = 420, $\langle \bar{\alpha} \rangle$ = 0.29% (a), 0.63% (b)
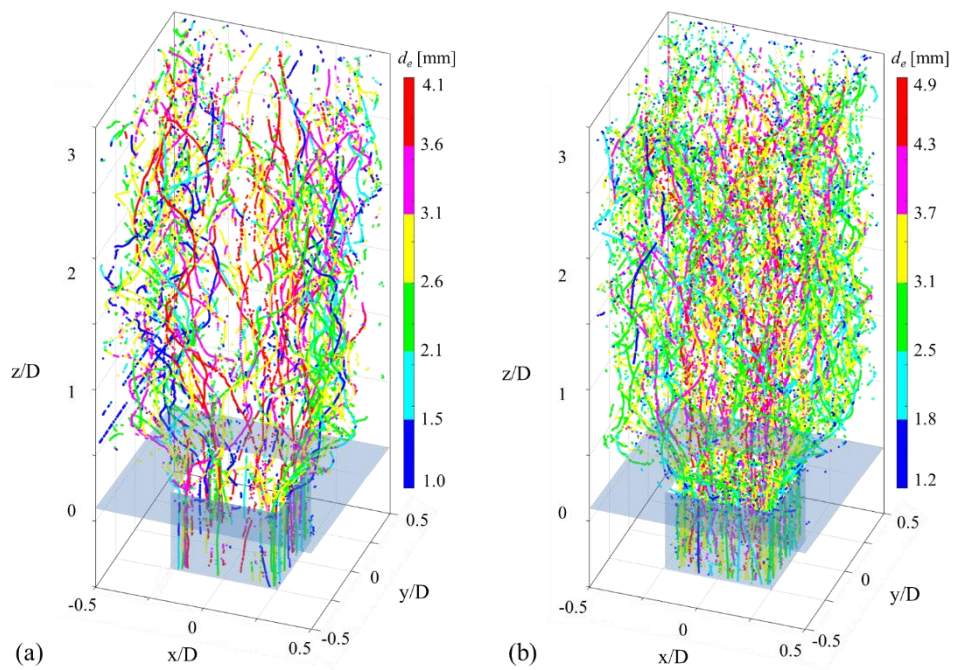
Fig. 4.3 3D bubble trajectories with bubble size contour for $Re = 6000$, $\langle \bar{\alpha} \rangle$ = 0.41% (a), 0.98% (b)
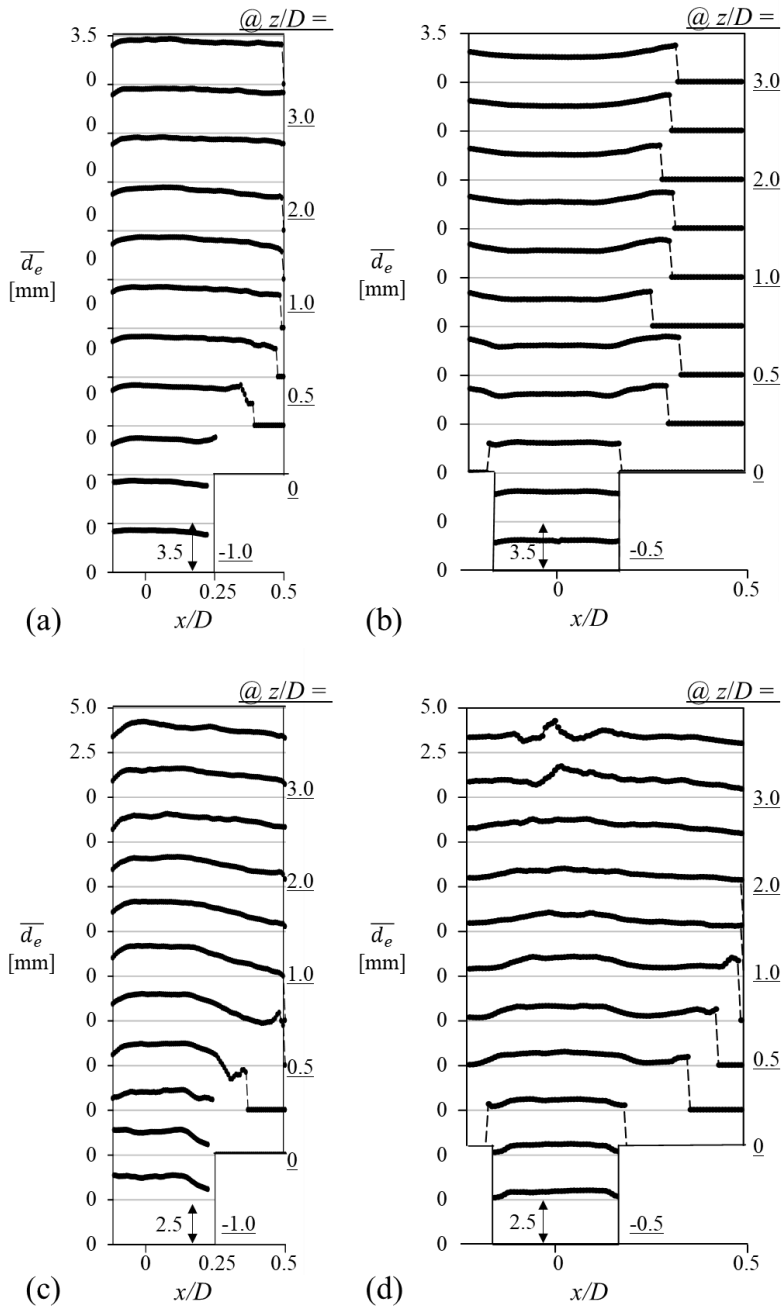
Fig. 4.4 Time-averaged bubble size ($\bar{d}_e$) distribution at (a) *Re*, $\langle\bar{\alpha}\rangle$, *ER* = 420, 0.39%, 4.0; (b) 440, 0.39%, 9.0; (c) 6000, 0.72%, 4.0; (d) 6000, 0.70%, 9.0. In vertical axes, each height (*z/D*) has the same scale.
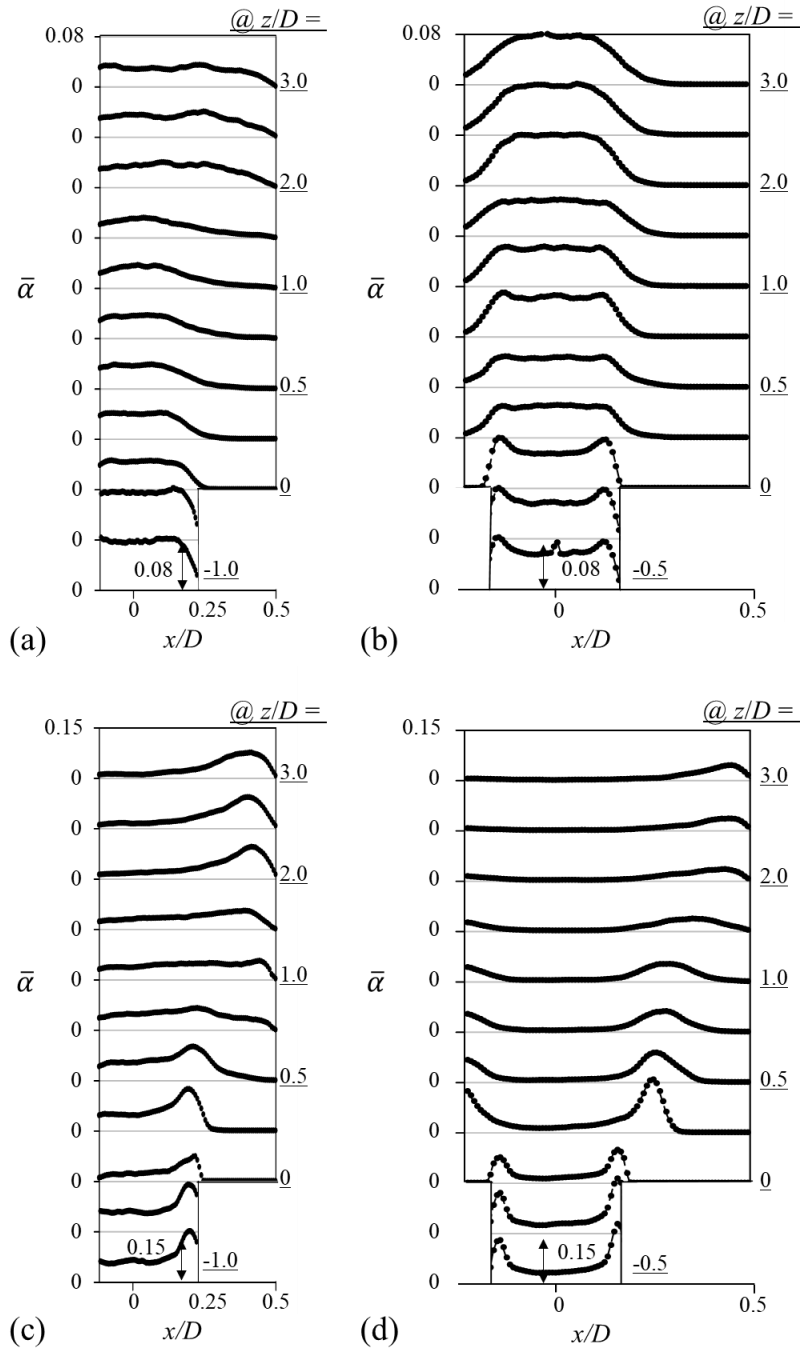
Fig. 4.5 Time-averaged lateral void distribution ($\bar{\alpha}$) at (a) *Re*, $\langle\bar{\alpha}\rangle$, *ER* = 420, 0.39%, 4.0; (b) 440, 0.39%, 9.0; (c) 6000, 0.72%, 4.0; (d) 6000, 0.70%, 9.0. In vertical axes, each height (*z/D*) has the same scale.

4 5
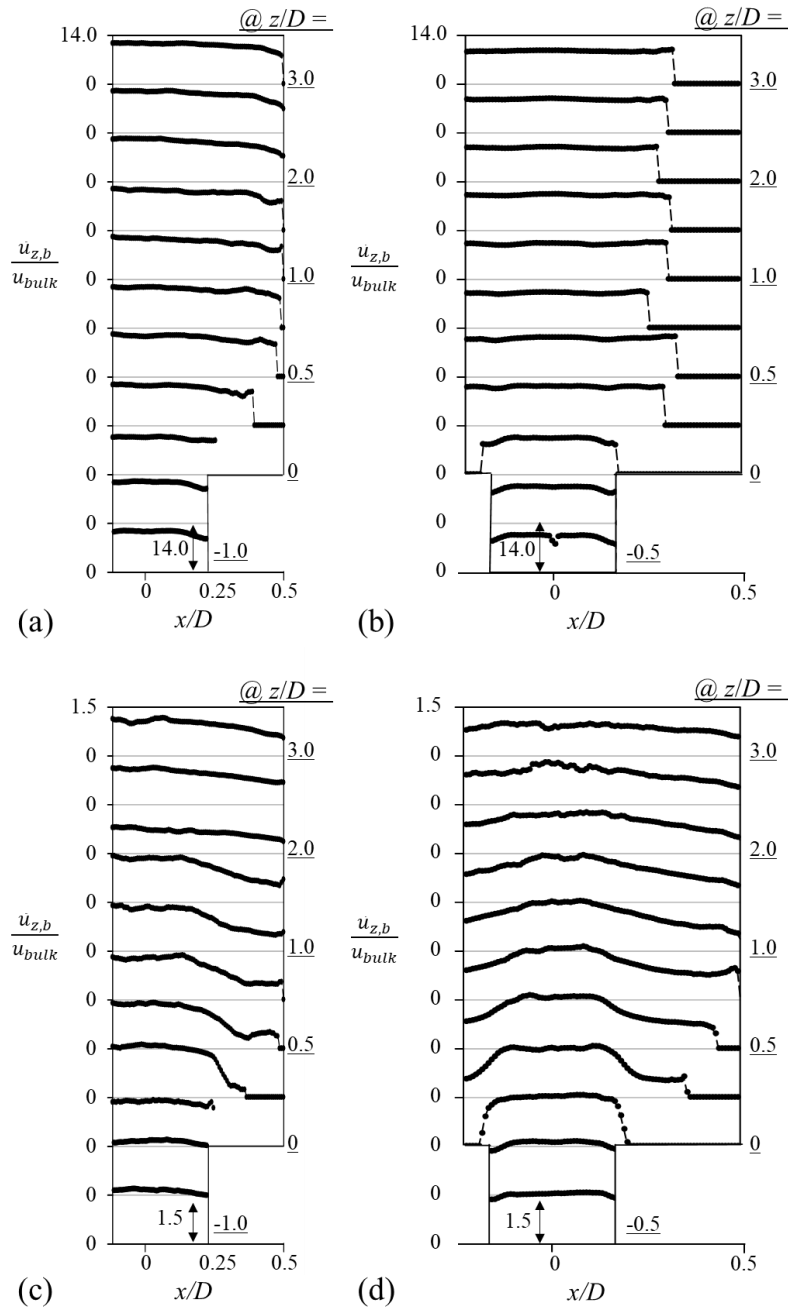
Fig. 4.6 Time-averaged bubble velocities in streamwise ($\bar{u}_{z,b}$) directions, normalized by the bulk velocity (u_b) of a single-phase flow: (a) Re, $\langle\bar{\alpha}\rangle$, $ER =$ 420, 0.39%, 4.0; (b) 440, 0.39%, 9.0; (c) 6000, 0.72%, 4.0; (d) 6000, 0.70%, 9.0. In vertical axes, each height (z/D) has the same scale.
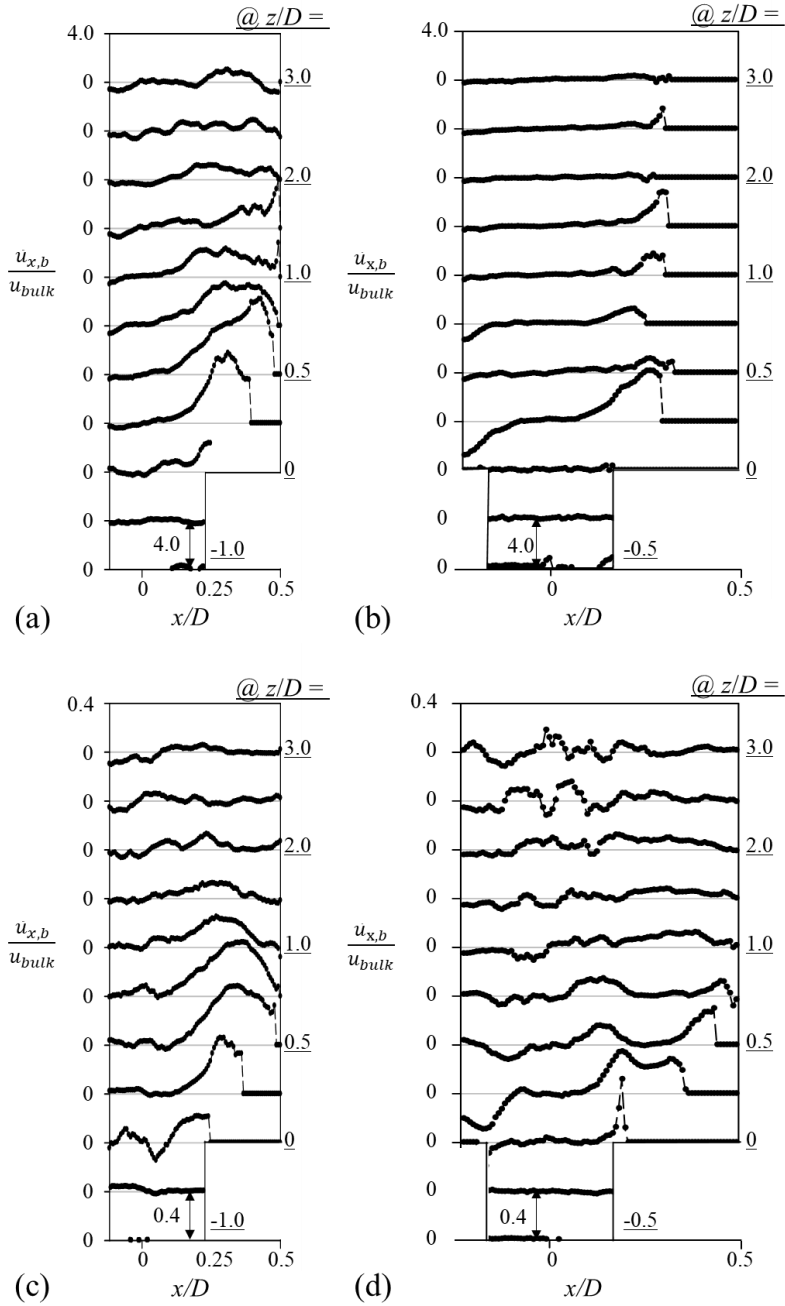
Fig. 4.7 Time-averaged bubble velocities in lateral ($\bar{u}_{x,b}$) directions, normalized by the bulk velocity (u_b) of a single-phase flow: (a) Re, $\langle\bar{\alpha}\rangle$, $ER = 420$, 0.39%, 4.0; (b) 440, 0.39%, 9.0; (c) 6000, 0.72%, 4.0; (d) 6000, 0.70%, 9.0. In vertical axes, each height (z/D) has the same scale.
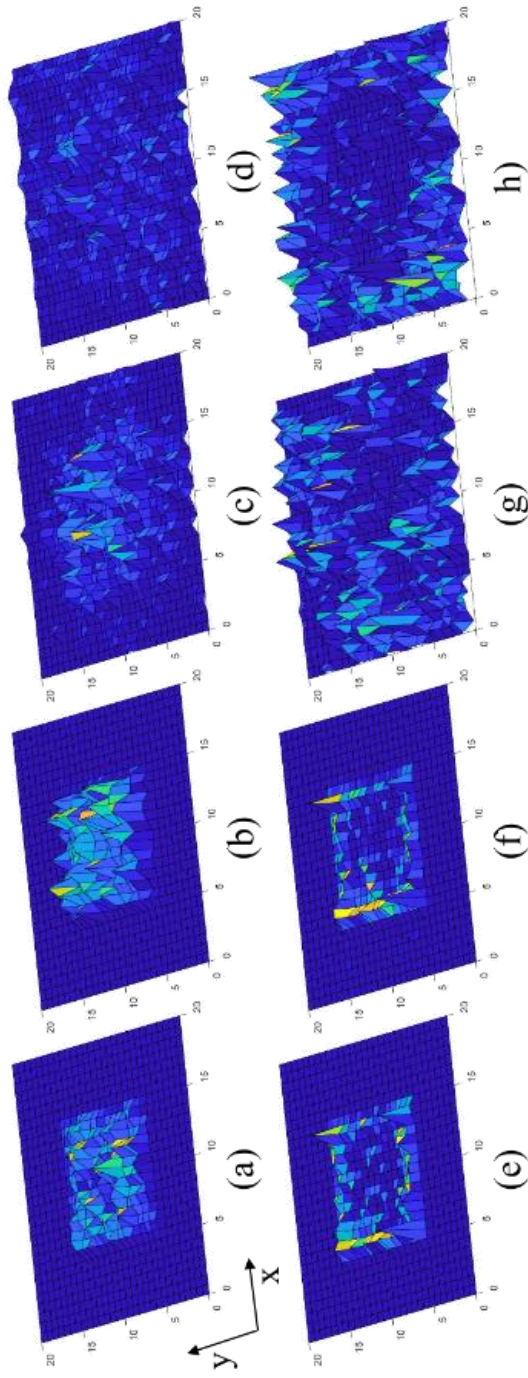
Fig. 4.8 3D void fraction distribution for (a)-(d) *Re*, $\langle\bar{\alpha}\rangle$, *ER* = 420, 0.29%, 4.0; (e)-(h) 6000, 0.41%, 4.0: Measured at z/D = -0.5 (a, e); 0 (b, f); 0.75 (c, g); and 2 (d, h).
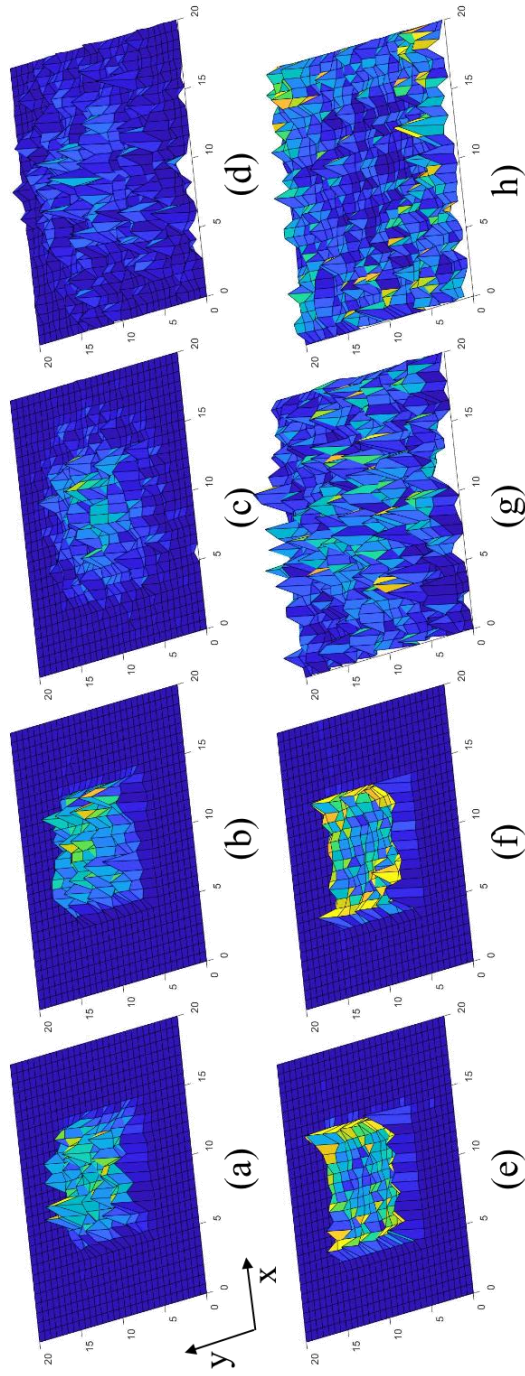
Fig. 4.9 3D void fraction distribution for (a)-(d) Re, $\langle \bar{\alpha} \rangle$, $ER = 420$, 0.63%, 4.0; (e)-(h) 6000, 0.98%, 4.0: Measured at z/D = -0.5 (a, e); 0 (b, f); 0.75 (c, g); and 2 (d, h).

Chapter 5.

Liquid-phase flow statistics modification due to bubbles

5.1 Inlet flow condition modification

Before analyzing the consequent change of liquid-phase flow statics by bubbles, we confirm inlet flow conditions and investigate the effects of gas-phase on liquid-phase flow structure. Velocity profiles before the expansion for each Reynolds number are plotted in Fig. 5.1. Flows in the present study show laminar and turbulent flow characteristics depending on the Reynolds number, and especially laminar flow velocity profile follows parabolic distribution well. Flows with different expansion ratios with similar Reynolds numbers have very similar flow conditions. In all cases, when the bubbles are injected, the liquid velocity core is flattened and the velocity gradient near the wall becomes stiff.

Next, we analyzed the changes in the turbulence statistics of the liquid phase with the mean volumetric void fraction $\langle \bar{\alpha} \rangle$ at each background *Re*. Fig. 5.2 shows time-averaged streamwise liquid velocity and turbulence statistics in the laminar flow with *ER* = 9.0 varying with $\langle \bar{\alpha} \rangle$. In Fig. 5.2(a), the mean streamwise velocity in the core increased with increasing void fraction and the near-wall velocity gradient became steeper which means enhanced turbulence. The root-mean-square of streamwise (Fig. 5.2b) and lateral (Fig. 5.2c) liquid-phase velocity fluctuations also increased significantly with void fraction increasing compared to that of the single-phase flow. Similar to laminar flow, in the case of turbulent flow, we observed an increase in near-wall velocity gradient and a decrease in core region velocity with a higher void fraction (Fig. 5.3a), leading to an overall increase in turbulence. Interestingly, in the region with the small void fraction ($\langle \bar{\alpha} \rangle$ < 0.5%), we observed that the increase in turbulence was less sensitive to the increase in $\langle \bar{\alpha} \rangle$ (Figs. 5.3b, 5.3c).

The changes in the turbulence statistics can be analyzed more intuitively in the centerline turbulence intensity variation with $\langle \bar{\alpha} \rangle$ (Fig. 5.4). As $\langle \bar{\alpha} \rangle$ increases, in

laminar flow (Fig. 5.4a), the inlet centerline liquid-phase turbulence intensities in both streamwise and lateral directions show a linear increase. The inlet turbulence intensity also increases as $\langle\bar{\alpha}\rangle$ increases for turbulent flow (Fig. 5.4b), except in the range $\langle\bar{\alpha}\rangle < 0.5\%$, which shows a plateau in the lateral turbulence intensity. This is expected because, in the case of laminar flow, there is little background turbulence, resulting in a stronger BIT as more bubbles are injected, whereas in the case of turbulent flow, strong SIT and bubbles interact near the wall. It has been reported that the energy spectrum slope changes from -5/3 to -3 on a small scale in the bubbly flow due to fluctuation by bubbles (Prakash et al., 2016; Alméras et al., 2017). Fig. 5.5 shows the energy spectrum at the inlet and after the expansion, respectively, using the autocorrelation function to confirm that the flow of the current experiment followed the slope change in previous studies. The slope of -5/3 in the inertial sub-range was observed in both before and after the expansion, and it was confirmed that the slope changed to around -3 after bubbles were injected.

Fig. 5.6 shows a variation of reattachment length normalized by single-phase flow reattachment length ($z_{R,s}$) with inlet centerline turbulence intensity. It is well known that the reattachment length decreases with increasing liquid-phase turbulence in the backstep or expansion pipe flow (Park et al., 2007). The present study also showed a trend in which the reattachment length decreased as the inlet turbulence intensity ($\langle\bar{\alpha}\rangle$) increased in both laminar and turbulent flows. However, in the two cases with the highest turbulence intensities in laminar flow ($\langle\bar{\alpha}\rangle > 2.0$), the reattachment length tended to increase as the inlet turbulence increased. In a bubbly flow in an expansion pipe, the turbulence of the inlet flow as well as the BIT after expansion can affect the reduction of reattachment length. Therefore, it can be inferred that the reason for the sudden increase in the reattachment length in laminar flow with $\langle\bar{\alpha}\rangle > 2\%$, the bubble-bubble interaction (such as collision, coalescence, and break-up) after expansion significantly increases, resulting in increased interference between flow structures.

Fig. 5.7 shows the scaling relation between bubble-induced inlet streamwise velocity fluctuation and $\langle\bar{\alpha}\rangle$. Risso and Ellingsen (2002) show the bubble-induced turbulence resulting from interactions between flow structures is proportional to the 0.4 power of $\langle\bar{\alpha}\rangle$. Also, pure bubble-induced turbulence was evaluated using liquid

velocity decomposition ($v_l = \bar{v}_l + v_l' + v_l''$) proposed by Sato & Sekoguchi (1975), agrees well with power relations. The turbulent flow showed a slight change in slope after the $\langle \bar{\alpha} \rangle$ the regime in which the power relation was verified ($\langle \bar{\alpha} \rangle < 0.0105$).

5.2 Liquid-phase flow statistics

Now, we compare the liquid-phase flow statistics of single- and two-phase flows and $ER = 4.9$ and 9.0. As a representing condition, we consider the cases of $\langle \bar{\alpha} \rangle$, $ER = 0.39\%$, 4.0 and $\langle \bar{\alpha} \rangle$, $ER = 0.39\%$, 9.0 for laminar flow ($Re \sim 400$), and $\langle \bar{\alpha} \rangle$, $ER = 0.72\%$, 4.0 and $\langle \bar{\alpha} \rangle$, $ER = 0.70\%$, 9.0 for turbulent flow ($Re = 6000$). Figs. 5.8 and 5.9 show the time-averaged streamwise ($\bar{u}_z$) and lateral ($\bar{u}_x$) liquid-phase velocity profiles along the streamwise directions, respectively. With the bubbles, the streamwise velocity profiles are flattened in the core and the accelerated flow region is widened toward the wall quite fast, which is observed better for laminar flow (Figs. 5.8a, 5.8b).

The lateral velocity components are modified similarly with bubbles; i.e., the accelerated flow region, centered at $x/D \simeq 0.25$, becomes wider along the lateral direction (Fig. 5.9). However, the influence is clearer for the turbulent flow, which is attributed to more vigorous lateral migration of bubbles, as we explained above. Interestingly, in laminar flow, the lateral velocity varies largely after the reattachment (Figs. 5.8a, 5.8b) and this is because the bubbles regain their rocking motion as the flow re-develops after the reattachment. For both laminar and turbulent flows, therefore the separating shear layer after the expansion is thicker, and the velocity profiles converge faster along the streamwise direction for a two-phase flow due to the enhanced mixing by rising bubbles.

Comparing the streamwise velocity of $ER = 4.0$ (Fig. 5.8c) and 9.0 (Fig. 5.8d), it can be seen that the entrainment in the recirculation zone increases in the two-phase flow compared to the single-phase flow, and the effect is larger at an expansion ratio of 9.0 than at 4.0. As the high momentum fluid in the shear layer enters the wake more, the shear layer spreads rapidly and accelerates the reattachment in the two-phase flow, especially faster in larger ER.

On the other hand, based on the streamwise velocity profiles, the location of reattachment ($\partial \bar{u}_z/\partial x = 0$ at $x/D = 0.5$) can be measured. For a single-phase flow, it

is measured to be $z_R \simeq 26h$ ($= 6.5D$) ($Re, ER = 420, 4.0$), $24h$ ($= 8D$) ($Re, ER = 440$, 9.0), $8.9h$ ($= 2.2D$) ($Re, ER = 6000, 4.0$), and $8.7h$ ($= 2.9D$) ($Re, ER = 6000, 9.0$), respectively. Here, step height h is defined as $h = (D - d)/2$. These results agree with the experimental data reported for similar conditions (Park et al., 2007).

With bubbles, the reattachment of the separated shear layer occurs earlier and the reattachment length is measured as $z_R \simeq 8.7h$ ($= 2.2D$) ($Re, ER = 420, 4.0$), $11.4h$ ($= 3.8D$) ($Re, ER = 440, 9.0$), $6.5h$ ($= 1.6D$) ($Re, ER = 6000, 4.0$), and $5.9h$ ($= 2D$) ($Re, ER = 6000, 9.0$), respectively. If we revisit the void distribution, it is understood that bubbles cannot penetrate the recirculation zone immediately after the expansion ($z/D < 0.75$) but are rapidly accelerated toward the wall (Fig. 4.7). After the reattachment of the flow, bubbles recover their distribution of the inlet ($z/D < 0$) quite fast.

Turbulence statistics of the liquid-phase flow are shown in Figs. 5.10 – 5.12. Here, the root-mean-square of liquid-phase velocity fluctuations ($u'_{z,rms}$ and $u'_{x,rms}$) and Reynolds stress ($-\overline{u'_x u'_z}$) are normalized by bulk velocity (u_{bulk}) of the single-phase flow. With bubbles, additional turbulence is induced, which propagates toward the wall as the flow develops.

The single-phase laminar flow shows nearly zero velocity fluctuation, but with the gas phase added, velocity fluctuations increase significantly and they show a broad core peak profile for both streamwise and lateral components (Figs. 5.10a, 5.10b, 5.11a and 5.11b). For $Re = 6000$, the single-phase flow turbulence shows a typical distribution behind a step edge; the turbulence distribution has a sharp peak emanating from the step edge, which becomes wider along the separating shear layer (Park et al., 2007). With bubbles, the enhanced turbulence in the inlet flow ($z/D < 0$) interacts with the turbulence in this shear layer after the expansion ($0 < z/D < 1.0$), and its effect propagates toward the wall.

Like the time-averaged velocity, the locally enhanced turbulence due to bubbles is saturated quite fast as the reattached flow re-develops (Figs. 5.11a and 5.11b). Therefore, the effect of bubble-induced turbulence is quite dominant very near the step edge ($z/D < 2.0$) while the shear-induced turbulence in the background flow sustains a little bit longer up to $z/D \simeq 3.0$. In turbulent flow, the contribution of bubble-induced agitation to $u'_{z,rms}$ (Figs. 5.10c and 5.10d) is larger than that of $u'_{x,rms}$

(Figs. 5.11c and 5.11d), which is again attributed to the strong lateral flow structures behind the step. Comparing the turbulence in *ER* 4.0 (Figs. 5.10c and 5.11c) and 9.0 (Figs. 5.10d and 5.11d) the turbulence increases with higher expansion ratios, and the difference was even greater when bubbles were injected. This enhancement of BIT in a pipe with a wider cross-sectional area after the expansion leads to faster flow reattach in ER 9.0 compared to *ER* 4.0.

The effect of bubbles on the Reynolds stress distribution also appears to be similar. As shown in Figs. 5.12 (a) and (b), for the laminar flow, bubble-induced turbulence in the upstream flow ($z/D < 0$) is amplified substantially through the interaction with the separating shear layer at $0 < z/D \lesssim 1.0$ for *ER* 4.0 and $0 < z/D \lesssim 2.0$ for *ER* 9.0. With further bubble dispersion in downstream, it tends to be saturated. In turbulent flow, the enhanced turbulence starts to saturate at $z/D \simeq 2.5$, which is faster than the single-phase flow (Figs. 5.12c and d). Thus, it is understood that the added bubbles enhance the turbulence of the separated flow effectively, especially at very near the separating edge, which energizes the separated flow to force the early reattachment.

This also indicates that in addition to the enhancement of mixing by bubble wakes, the reduction of the dead zone behind the step contributes to the mixing enhancement. A similar strategy has been popular to control the flow behind a single-phase backward-facing step for the purpose of mixing enhancement (Chun and Sung, 1996; Yoshioka et al., 2001; Park et al., 2007). In particular, it has been shown that three-dimensional disturbance, like the bubble-induced perturbations to the flow in the present study, is more effective in reducing the reattachment length behind the backstep (Park et al., 2007).

The pressure decreases and increases sharply after the expansion and becomes saturated at a value higher than the inlet. To determine the effect of bubble injection and ER change on the pressure drop after expansion, the pressure Poisson equation was calculated from the PIV results (Park & Park, 2021):

$$\nabla^2 \bar{p} = \rho_l \frac{\partial}{\partial x_i}\left(-\frac{\partial}{\partial x_i}\left(\bar{u}_i \bar{u}_j\right) + \nu \nabla^2 \bar{u}_j - \frac{\partial}{\partial x_i}\overline{u_i' u_j'}\right) \tag{5.1}$$

$$\overline{c_p} = (\bar{p} - p_\infty)/(0.5\rho_l u_\infty^2) \qquad (5.2)$$

Fig 5.13 shows the time-averaged pressure coefficient ($\overline{c_p}$) field after expansion for Re = 6000. It can be seen that the pressure drop was larger in ER = 9.0 (Figs. 5.13b, 5.13d) compared to ER = 4.0 (Figs. 5.13a, 5.13c), two-phase flow (Figs. 5.13a, 5.13b) compared to single-phase flow (Figs. 5.13a, 5.13b). In addition, it can be confirmed that the shear layer of the two-phase flow is formed thicker than that of the single-phase flow. The pressure analysis results support the bubble behavior and the reattachment length reduction mechanism identified in the liquid phase flow field.

5.3 Shear layer vorticity thickness

In both laminar and turbulent flow, the faster the shear layer spreads, the faster the flow reattaches. To further compare the spreading rate of the shear layer under single- and two-phase flow for different ERs, we calculated the development of the shear layer vorticity thickness (δ_ω/h) (Smits & Dussauge, 2006) under each flow condition as follows:

$$\delta_\omega(z) = \frac{\Delta\overline{u_z}}{max\left(\left|\frac{\partial\overline{u_z}}{\partial x}\right|\right)} \qquad (5.3)$$

Figs. 5.14 and 5.15 shows the development of shear layer vorticity thickness for laminar and turbulent flow, respectively. When bubbles were injected into the laminar flow, the shear layer spreading rate increased as much as the turbulent flow ($\Delta\delta_\omega/\Delta z \approx 0.2$ for $Re = 4.3 \times 10^5$, Schrijer et al., 2014), and the slope changes larger in ER 4.0 compared to 9.0, leading to faster flow reattachment in ER 4.0. In turbulent single-phase flow (Fig. 5.15), similar to the laminar flow, the spreading rate of ER 4.0 is larger than that of ER 9.0. After bubbles are injected, the slope of ER 4.0 is almost maintained, but for ER .09, the slope is greatly increased and becomes almost similar to the slope of ER 4.0, leading to a larger reattachment length reduction compared to single phase flow in ER 9.0.

We also calculated the shear layer vorticity thickness of the turbulent flow

according to the increase of the mean void fraction to analyze the effect of the void fraction on the shear layer development (Fig. 5.16). As a result, as the mean void fraction increased, the initial shear layer vorticity thickness gradient also increased.

5.4 Interfacial forces on rising bubbles

5.4.1 Interfacial force models

Since the liquid-phase velocity distributions are available, it will be meaningful to estimate the interfacial forces acting on the rising bubbles to understand the bubble size dependency of bubble dispersion. Among the force components that can affect the bubble movement, here we consider the drag (F_D), lift (F_L), wall-lubricant (F_W), and turbulent dispersion (F_{TD}) forces (Fig. 5.17). Since we are interested in the lateral bubble dispersion, each force in the following equations denotes the lateral component. The net lateral force per unit volume is expressed as:

$$F_T = \alpha(F_D + F_L + F_W) + F_{TD} \qquad (5.4)$$

Here, we ignore the forces due to bubble collision and the virtual mass effect. Because the void fraction (< 0.03) of the present experiment is relatively small, these forces are estimated to be smaller than the forces considered in Eq. (5.4) (Lahey et al., 1980; Sharma et al., 2017). Drag force is proportional to the square of the relative bubble velocity and is expressed as:

$$F_D = -C_D \rho_l \frac{3}{4d_e} |u_{x,b} - u_x|(u_{x,b} - u_x) \qquad (5.5)$$

Here, the drag coefficient (C_D) of the distorted multiple bubble system is derived based on the mixture viscosity model Ishii and Zuber (1979):

$$C_D = \frac{2}{3} d_e \sqrt{\frac{g(\rho_l - \rho_g)}{\sigma}} (1 - \alpha)^{-1/2} \quad \text{(for } \mu_l \gg \mu_g) \qquad (5.6)$$

Here, μ_l and μ_g represent the liquid- and gas-phase viscosity, respectively. Wall-normal lift force is induced by the liquid-phase shear (known as the Saffman's lift) and is expressed as below. We use the lift coefficient (C_L) model for a single bubble in a simple shear flow suggested by Tomiyama et al. (2002). According to Tomiyama et al. (2002), C_L is controlled by different dimensionless numbers depending on the bubble size. For smaller bubbles ($d_e \lesssim 4.4$ mm), it is determined by Reynolds number (d_e as a reference length), while C_L on larger bubbles ($d_e > 4.4$ mm) is governed by modified Eötvös number (bubble horizontal length as a reference length). In the present study, most of the bubbles belong to the first range, and C_L as a function of the Reynolds number is used.

$$F_L = -C_L \rho_l (u_{z,b} - u_z) \times \frac{\partial u_z}{\partial x} \tag{5.7}$$

$$C_L = \begin{cases} min(\,0.288\,tanh(\,0.121\,Re_b),\ f(Eo)), & Eo < 4 \\ f(Eo), & 4 \le Eo \le 10.7 \end{cases} \tag{5.8}$$

$$f(Eo) = 0.00105Eo^3 - 0.0159Eo^2 - 0.0204Eo + 0.474 \tag{5.9}$$

The bubble experiences a repulsion force as it approaches a solid wall, and for this wall-lubricant force, Tomiyama et al. (1995) developed a modified equation for this force per unit volume:

$$F_W = C_W \frac{d_e}{2} \rho_l [\frac{1}{y_W^2} - \frac{1}{(D - y_W)^2}](u_{z,b} - u_z)^2 \tag{5.10}$$

$$C_W = \begin{cases} e^{-0.933Eo + 0.179}, & 1 \le Eo \le 5 \\ 0.007Eo + 0.04, & 5 < Eo \le 33 \end{cases} \tag{5.11}$$

Here, y_w is the wall distance, and C_W is the wall-lubricant force coefficient. Lastly, the turbulent dispersion force due to the interphase turbulent momentum transfer is considered. Lahey et al. (1993) derived a formulation:

$$F_{TD} = -0.1\rho_l k_l \nabla \alpha \tag{5.12}$$

Where k_l is the turbulent kinetic energy of the liquid–phase.

Based on the above equations, the distribution of time-averaged net lateral force (F_T) is shown, together with void fraction distribution in Fig. 5.18. It is noted that the estimation of interfacial forces would involve a higher uncertainty compared to the bubble size and velocities. For example, the lift force estimation is determined by the bubble size and velocities of both gas and liquid phases, resulting in an uncertainty of about 10% (see Section 2.3.2 for the uncertainty analysis).

Since the lift and wall-lubricant forces are determined by the streamwise velocity (which is quite larger than the lateral component), these two are found to be dominant over drag and turbulent dispersion forces, for example, both the ratios of F_D/F_L and F_{TD}/F_L are smaller than 0.05 in terms of their peak values.

In the figure, the negative (positive) force acts toward the core (wall) at $x/D > 0$ (it is opposite at $x/D < 0$). Considering this, the typical void distribution peak for laminar (broad core peak) and turbulent (wall peak) flows are qualitatively explained by the force distribution, as shown in Fig. 5.18. The negative lateral force (near the wall) is mostly contributed by the wall-repulsion force. That is, away from the wall, the wall-repulsion force becomes quite small. Thus, it is understood that the negative peak location corresponds to the position where the void fraction starts to decrease toward the wall, and effective BIT changes as the flow develops.

5.4.2 Bubble size distribution

The distributions of two dominant forces (lift and wall lubricant forces) are shown for $z/D = 0 – 1.0$ (near the step edge) in Fig. 5.19, together with the bubble size distribution, to examine the details of the lateral movements of the bubble depending on its size. The dispersion of bubbles toward the wall after the expansion ($z/D < 1.0$) is attributed to the shear-induced lift force. As shown in section 5.4.1, there is a sharp liquid velocity gradient after the expansion, and this results in a discernible lift force there. It is noted that the negative lift force at $x/D < 0$ applies to the wall ($x/D = -0.5$).

Right after the expansion, large bubbles approach the wall faster than small bubbles, because they experience a larger lift force than smaller ones under the same velocity gradient (Eq. (5.7), (5.8) and Fig. 5.19). However, for *ER* 4.0 (Fig 5.19c),

as the bubbles approach the wall, large bubbles are affected by the stronger repulsion force and cannot reach close to the wall, while small bubbles are allowed to move further almost touching the wall.

Unlike *ER* 4.0, in *ER* 9.0 (Fig 5.19d), the shear lift immediately after expansion becomes strong due to the large pressure drop and distance from the wall, large bubbles have a chance to reach the wall, and a bubble size peak is shown near the wall.

The magnitude difference of the lift according to ER difference is shown in the time-average wall-normal lift in Fig. 5.20. The lift immediately after the expansion ($z/D = 0.0$) of *ER* 9.0 increased 4 times compared to *ER* 4.0, and this lift peak decreases rapidly due to the influence of the increased pipe size. In laminar flow, although following the bubble size distribution according to the ER the lift force is not sufficient to push the bubbles to the wall, and most bubbles rise in the core region (Figs. 5.19a, b) in both ERs, whereas in turbulent flow, bubbles can reach the wall due to the sharper liquid-phase velocity gradient, i.e., stronger shear-induced lift force, near the step edge (Figs. 5.19c, d).

Although it was not shown in the figure due to its small values, before the expansion (in the fully developed region of a vertical channel flow), F_L and F_{TD} show peaks of an opposite sign at similar x positions. After the expansion, however, the signs of both peaks become the same. As the flow re-develops, two peaks approach the wall and a negative peak appears in F_{TD} to regain the initial profile before the expansion. This is because the void fraction is almost zero in the extended lateral direction of $x/D > 0.25$ after the expansion (Fig. 4.5), which makes the void fraction gradient induce F_{TD} in the same direction as F_L.
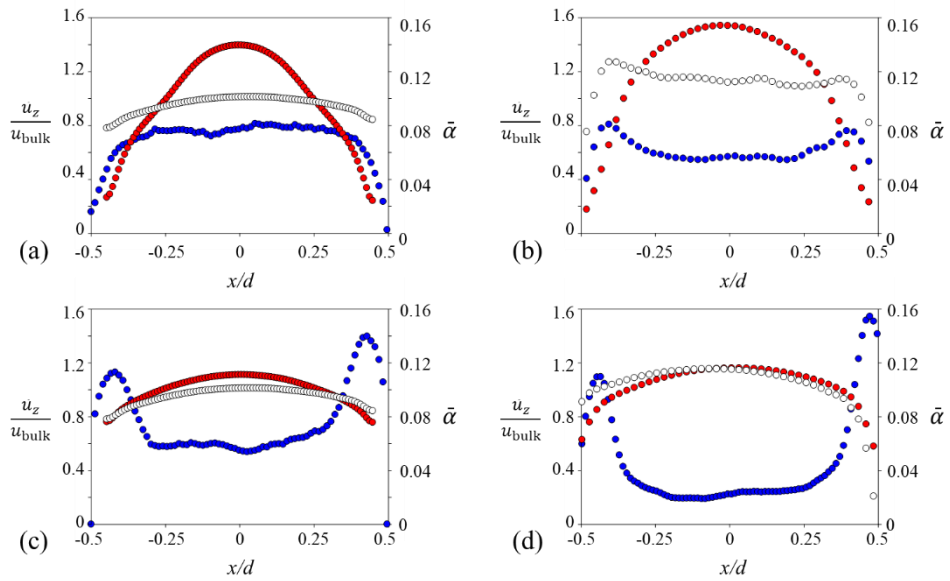
Fig. 5.1 Time-averaged streamwise liquid-phase velocity ($\bar{u}_z/u_{bulk}$) and lateral void distribution ($\bar{\alpha}$) at z/d = -1.0, y = 0 plane: (a) Re, $\langle\bar{\alpha}\rangle$, ER = 420, 0.39%, 4.0; (b) 440, 0.39%, 9.0; (c) 6000, 0.72%, 4.0; (d) 6000, 0.70%, 9.0. ●, single-phase flow velocity; ○, two-phase flow velocity; ●, void distribution.

6 0
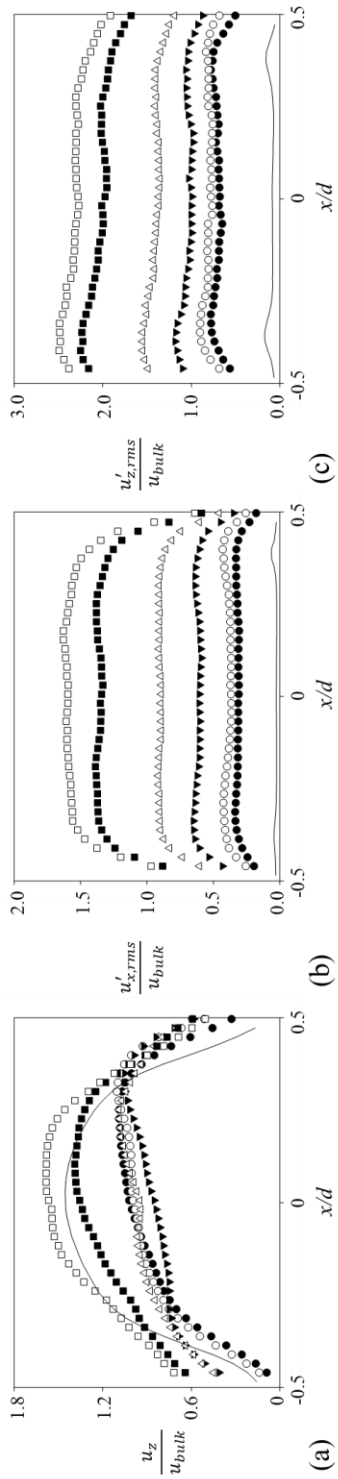
Fig. 5.2 Lateral distributions of (a) time-averaged streamwise liquid-phase velocity ($\bar{u}_z/u_{bulk}$), (b) root-mean-square of streamwise liquid-phase velocity fluctuation ($u'_{z,rms}/u_{bulk}$), (c) root-mean-square of lateral liquid-phase velocity fluctuation ($u'_{x,rms}/u_{bulk}$) at $z/d = -1.0$, $y = 0$ plane for $Re = 440$ and $ER = 9.0$: solid line, single-phase flow; ●, $\langle \bar{\alpha} \rangle = 0.30\%$; ○, 0.39%; ▼, 0.69%; △, 1.13%; ■, 2.01%; □, 2.80%.

6 1
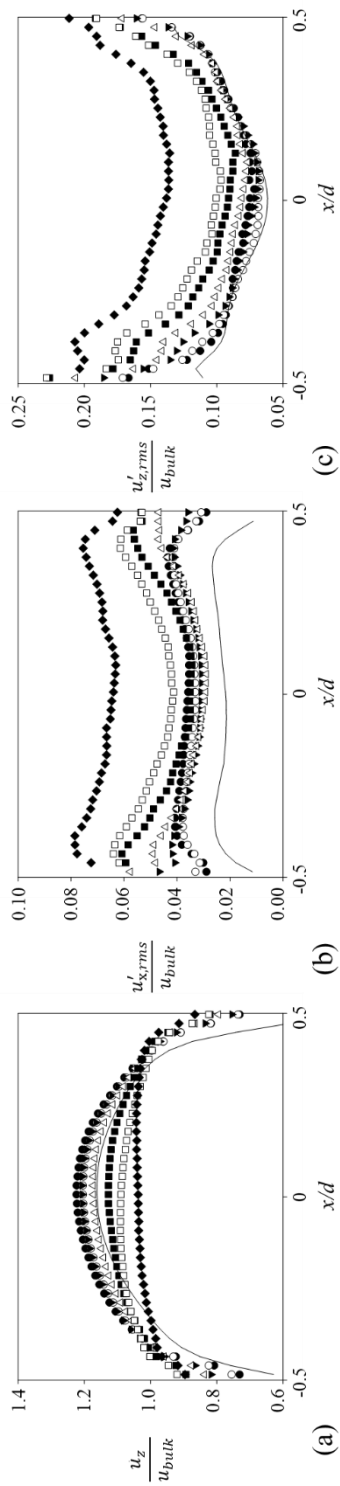
Fig. 5.3 Lateral distributions of (a) time-averaged streamwise liquid-phase velocity ($\bar{u}_z / u_{bulk}$), (b) root-mean-square of streamwise liquid-phase velocity fluctuation ($u'_{z,rms}/u_{bulk}$), (c) root-mean-square of lateral liquid-phase velocity fluctuation ($u'_{x,rms}/u_{bulk}$) at $z/d = -1.0$, $y = 0$ plane for $Re = 6000$ and $ER = 9.0$: solid line, single-phase flow; ●, $\langle \bar{\alpha} \rangle = 0.12\%$; ○, 0.23%; ▼, 0.43%; △, 0.70%; ■, 1.00%; □, 1.23%; ◆, 1.85%.

6 2
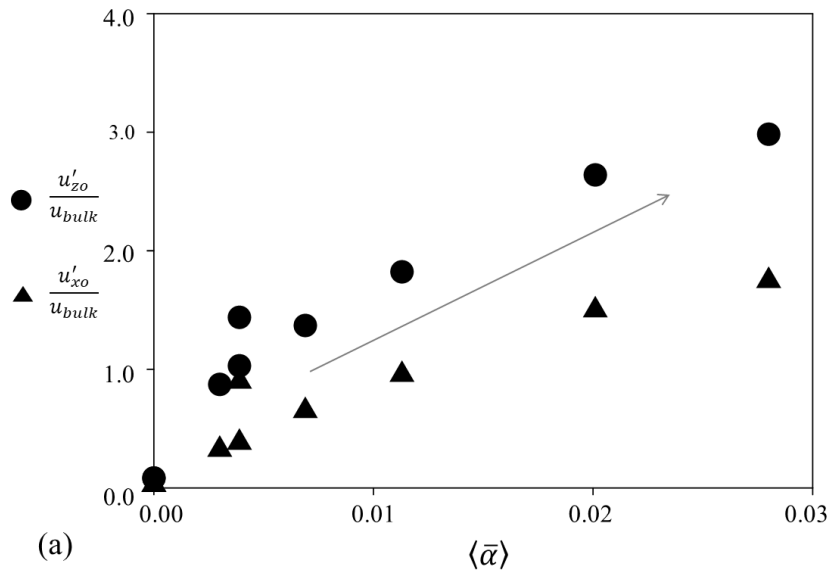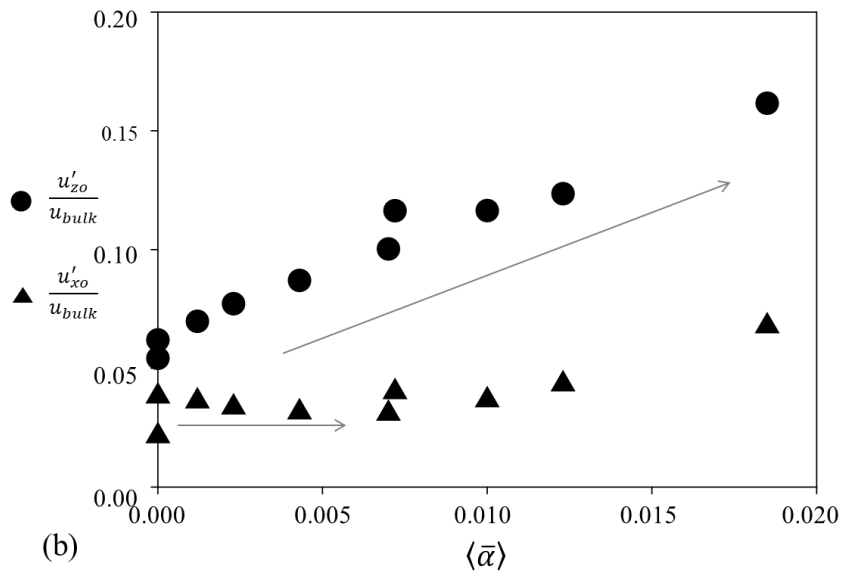
Fig. 5.4 Variation of inlet centerline streamwise (u'_{zo}/u_{bulk}) and lateral (u'_{xo}/u_{bulk}) turbulence intensity with volume void fraction $\langle\bar{\alpha}\rangle$ at (a) $Re \approx$ 400, (b) = 6000: ●, inlet centerline streamwise turbulence intensity; ▲, inlet centerline lateral turbulence intensity.
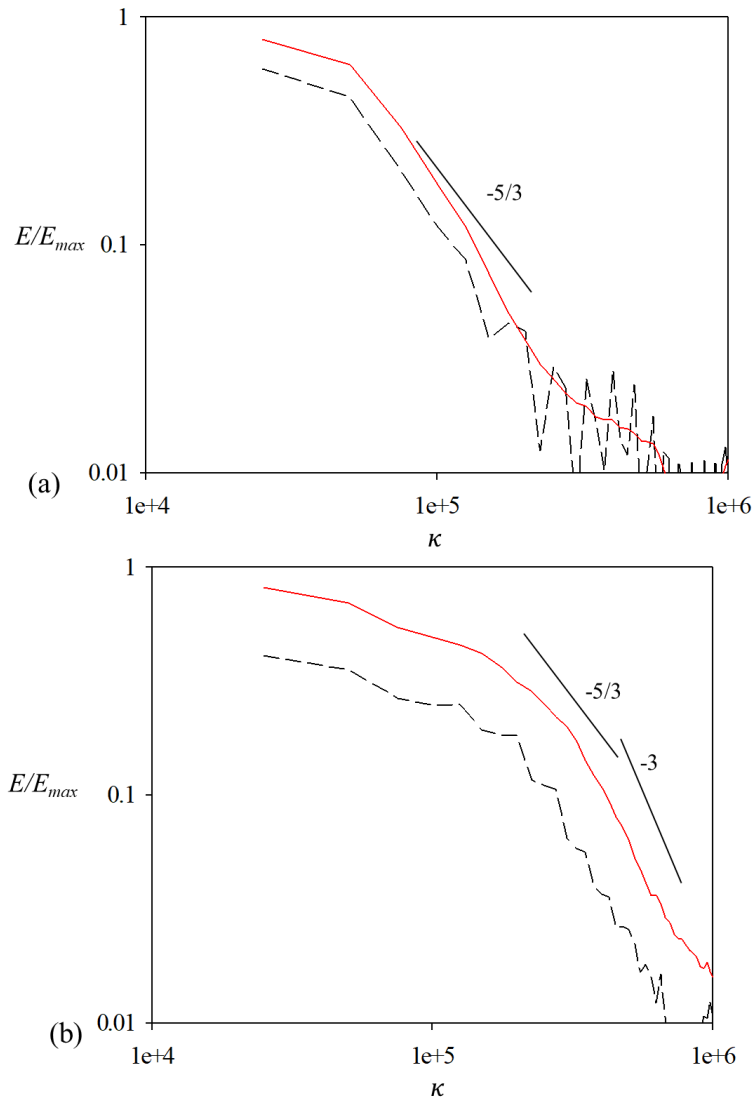
Fig. 5.5 Energy spectrum of turbulent flow with (Re, ER) = (440, 9.0) at x/d = 0. (a) single-phase; (b) $\langle \bar{\alpha} \rangle$ = 0.70 % : black dashed line, z/h = -1.0; red solid line, z/h = 1.5.
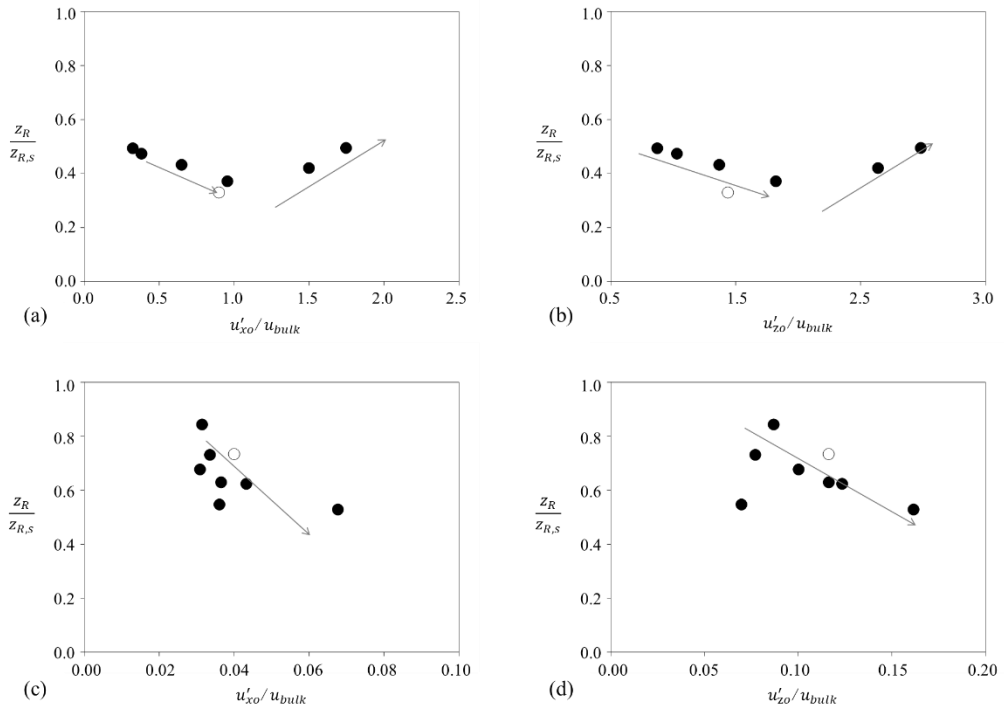
Fig. 5.6 Variation of the reattachment length (z_R) normalized by that of single-phase flow ($z_{R,s}$) with inlet centerline streamwise (u'_{zo}/u_{bulk}) and lateral (u'_{xo}/u_{bulk}) turbulence intensity at (a,b) $Re \approx 400$, (c,d) = 6000: $\bigcirc$, $ER = 4.0$; $\bullet$, 9.0.
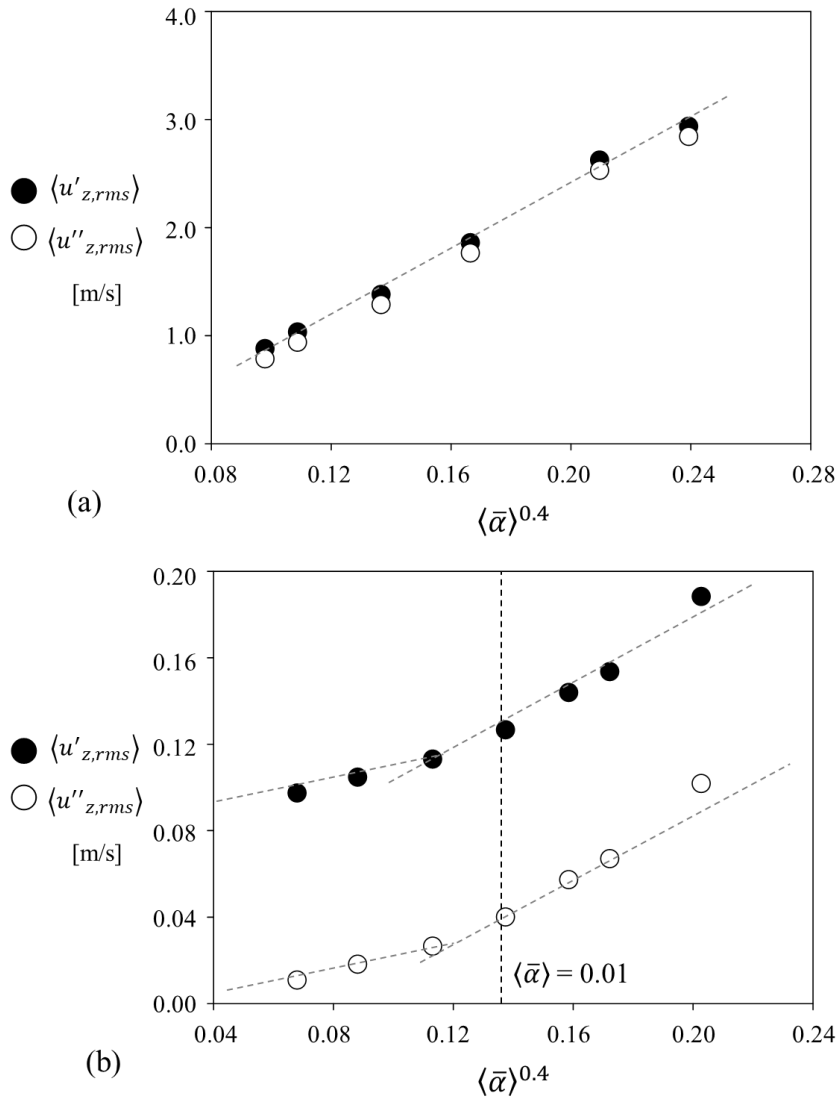
Fig. 5.7 Scaling relation between bubble-induced streamwise liquid velocity fluctuation and volume void fraction $\langle\bar{\alpha}\rangle$ at z/d = -1.0, y = 0 plane: (a) *Re*, *ER* = 440, 9.0; (b) 6000, 9.0. ●, inlet streamwise velocity fluctuation ($\langle u'_{z,rms}\rangle$); ○, pure bubble-induced inlet streamwise velocity fluctuation ($\langle u''_{z,rms}\rangle$).
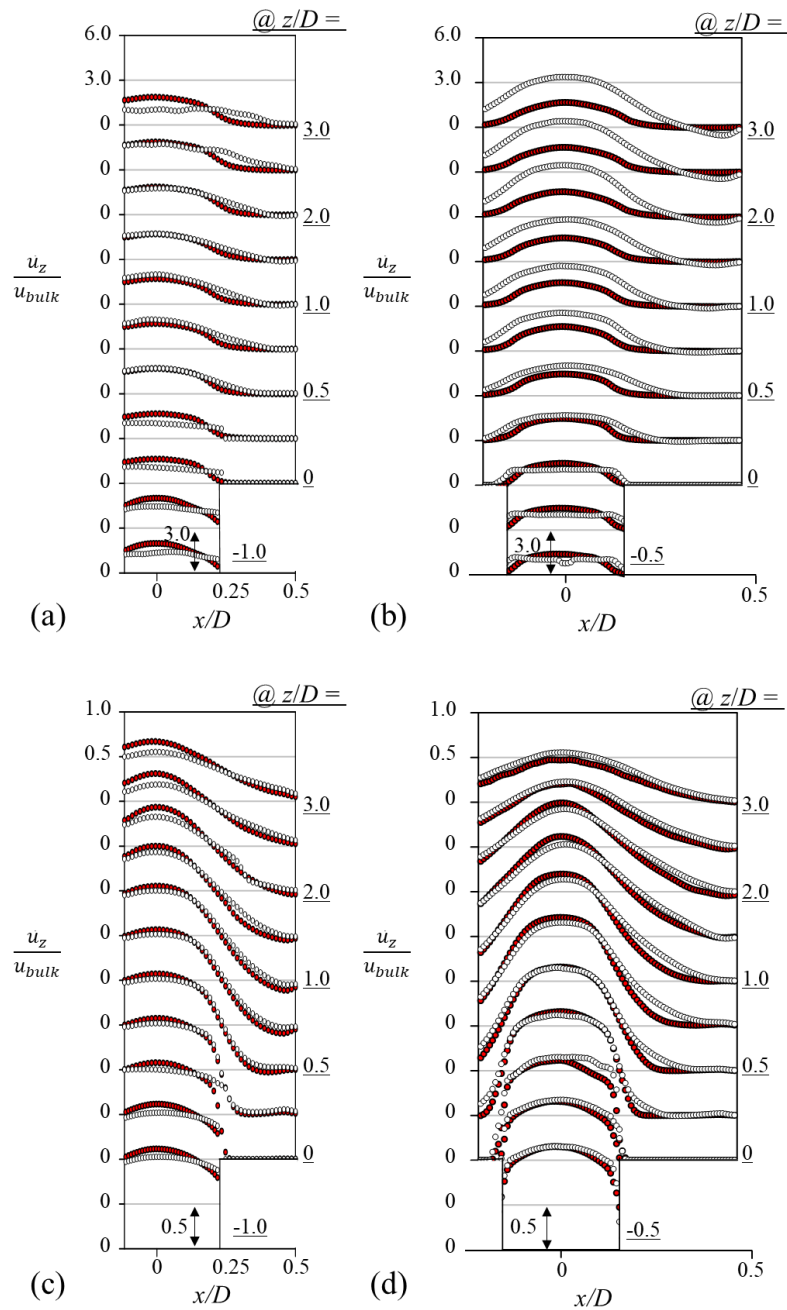
Fig. 5.8 Time-averaged streamwise liquid-phase velocity ($\bar{u}_z/u_{bulk}$) at (a) Re, $\langle\bar{\alpha}\rangle$, $ER = 420, 0.39\%, 4.0$; (b) $440, 0.39\%, 9.0$; (c) $6000, 0.72\%, 4.0$; (d) 6000, $0.70\%, 9.0$. ●, single-phase flow; ○, two-phase flow. In vertical axes, each height (z/D) has the same scale.
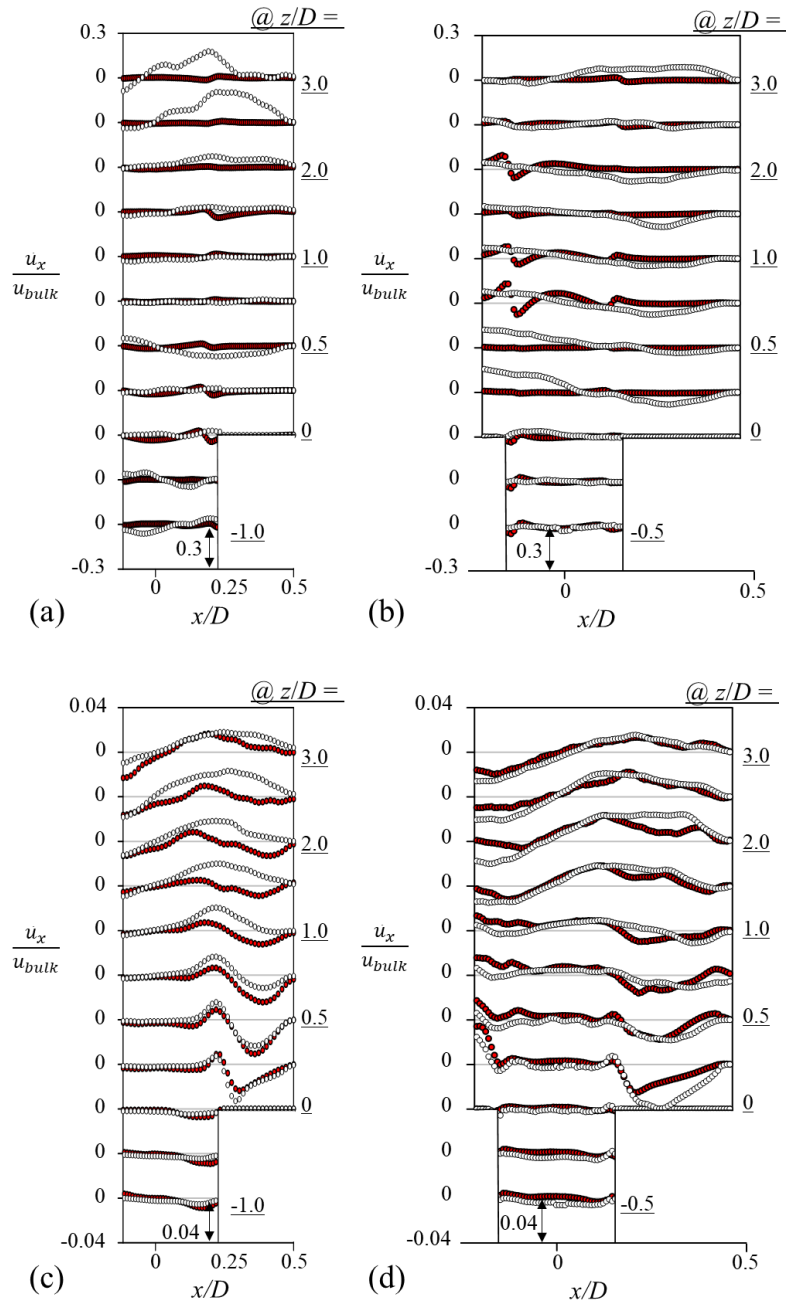
Fig. 5.9 Time-averaged lateral liquid-phase velocity ($\bar{u}_x/u_{bulk}$) at (a) Re, $\langle\bar{\alpha}\rangle$, ER = 420, 0.39%, 4.0; (b) 440, 0.39%, 9.0; (c) 6000, 0.72%, 4.0; (d) 6000, 0.70%, 9.0. ●, single-phase flow; ○, two-phase flow. In vertical axes, each height (z/D) has the same scale.
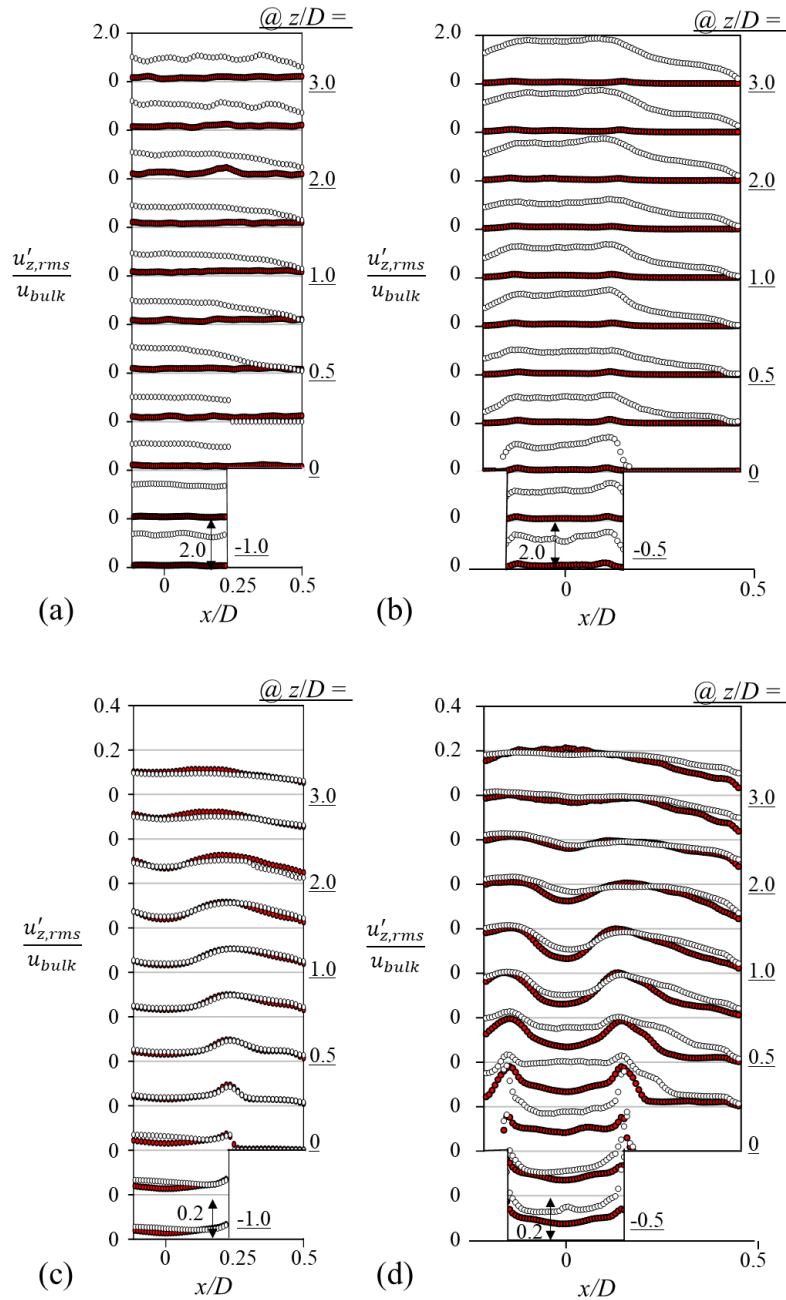
Fig. 5.10 Root-mean-square of streamwise liquid-phase velocity fluctuation ($u'_{z,rms}/u_{bulk}$) at (a) Re, $\langle\bar{\alpha}\rangle$, ER = 420, 0.39%, 4.0; (b) 440, 0.39%, 9.0; (c) 6000, 0.72%, 4.0; (d) 6000, 0.70%, 9.0. ●, single-phase flow; ○, two-phase flow. In vertical axes, each height (z/D) has the same scale.
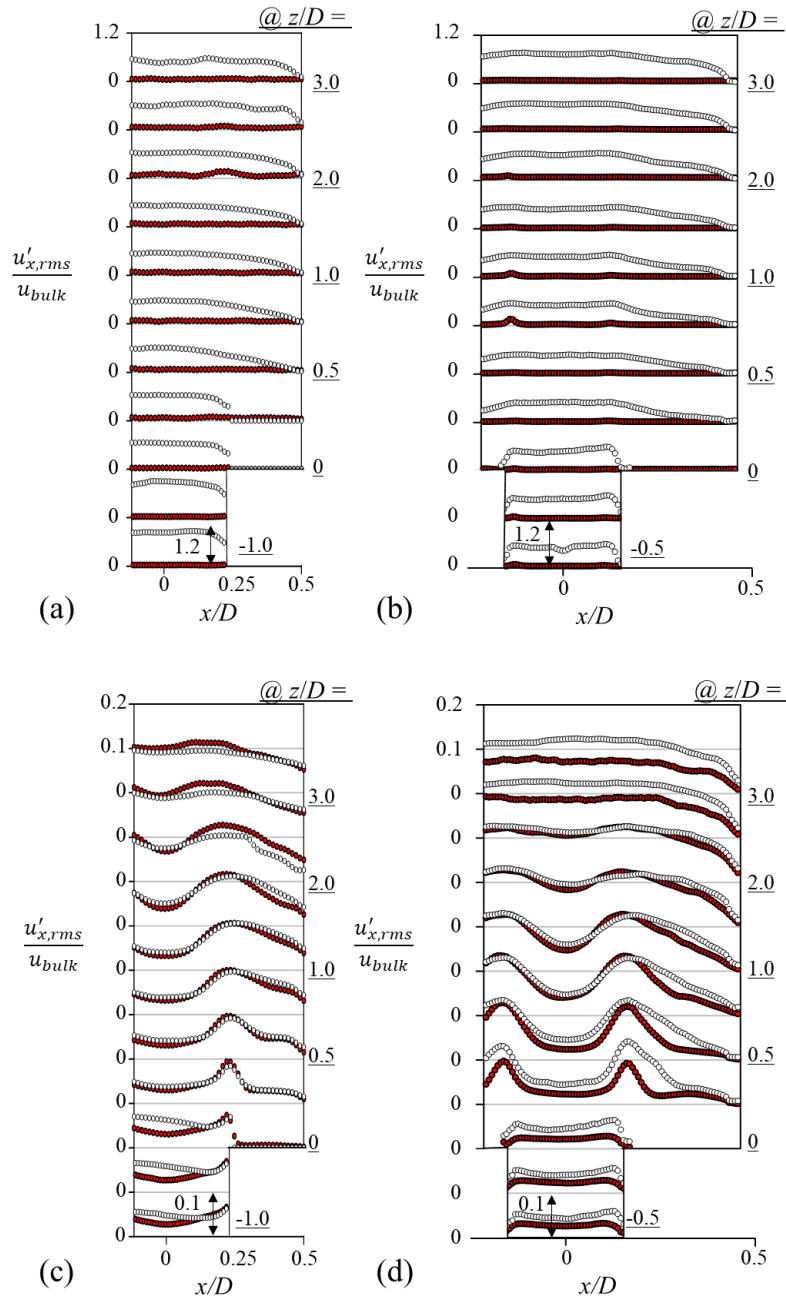
Fig. 5.11 Root-mean-square of lateral liquid-phase velocity fluctuation ($u'_{x,rms}/u_{bulk}$) at (a) Re, $\langle\bar{\alpha}\rangle$, $ER = 420$, 0.39%, 4.0; (b) 440, 0.39%, 9.0; (c) 6000, 0.72%, 4.0; (d) 6000, 0.70%, 9.0. ●, single-phase flow; ○, two-phase flow. In vertical axes, each height (z/D) has the same scale.
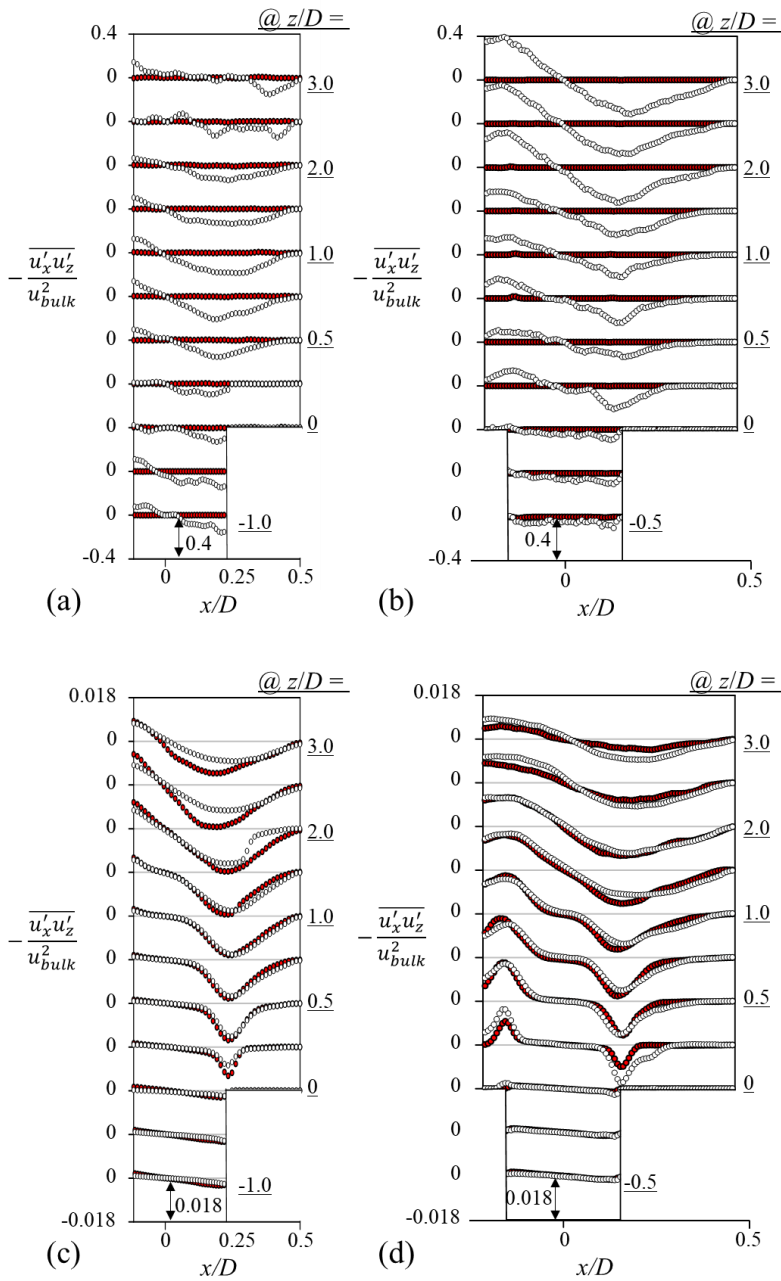
Fig. 5.12 Reynolds stress of liquid-phase ($-\overline{u'_x u'_z}/u^2_{bulk}$) at (a) Re, $\langle \bar{\alpha} \rangle$, ER = 420, 0.39%, 4.0; (b) 440, 0.39%, 9.0; (c) 6000, 0.72%, 4.0; (d) 6000, 0.70%, 9.0. ●, single-phase flow; ○, two-phase flow. In vertical axes, each height (z/D) has the same scale.
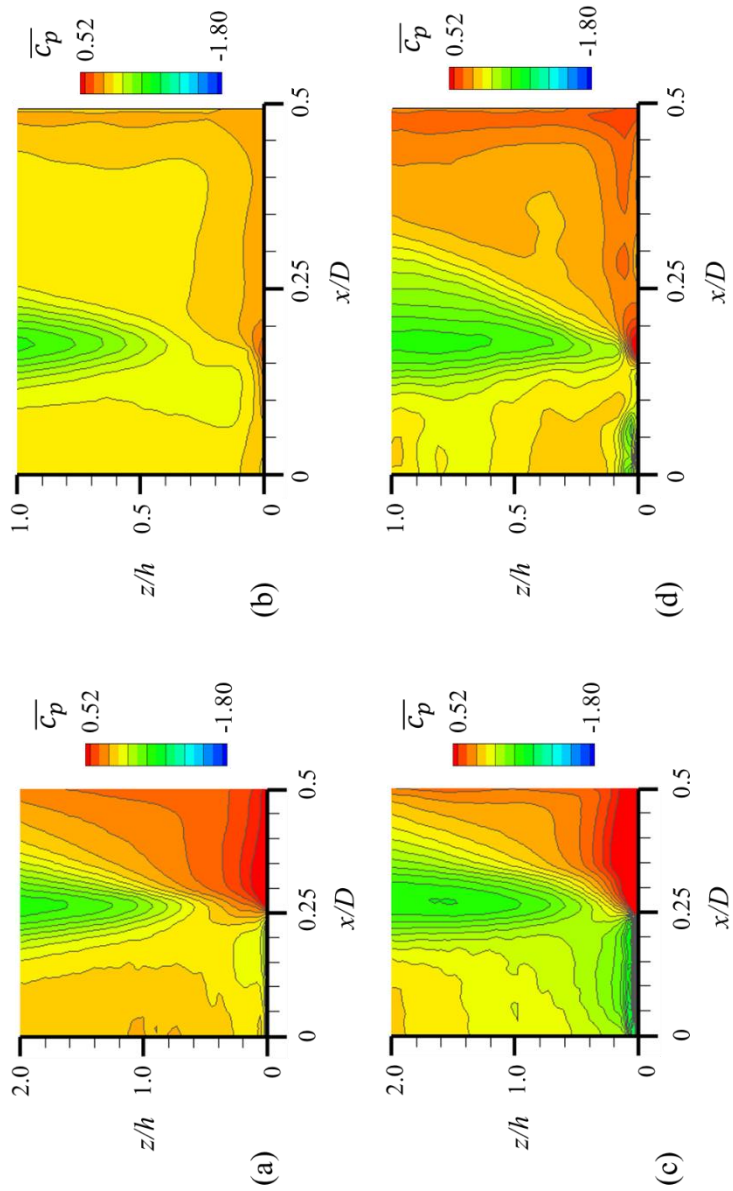
Fig. 5.13 Time-averaged pressure coefficient ($\overline{c_p}$) contour for Re = 6000: (a) $\langle\overline{\alpha}\rangle$, ER = 0, 4.0; (b) 0, 9.0; (c) 0.72%, 4.0; (d) 0.70%, 9.0.
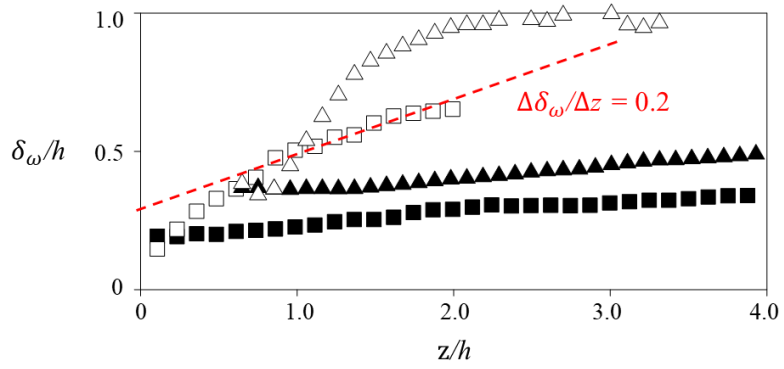
Fig. 5.14 Shear layer vorticity thickness (δ_ω/h) at $Re \approx 400$: ▲, $\langle\bar{\alpha}\rangle$, $ER = 0\%$, 4.0; △, 0.39%, 4.0; ■, 0%, 9.0; □, 0.39%, 9.0.
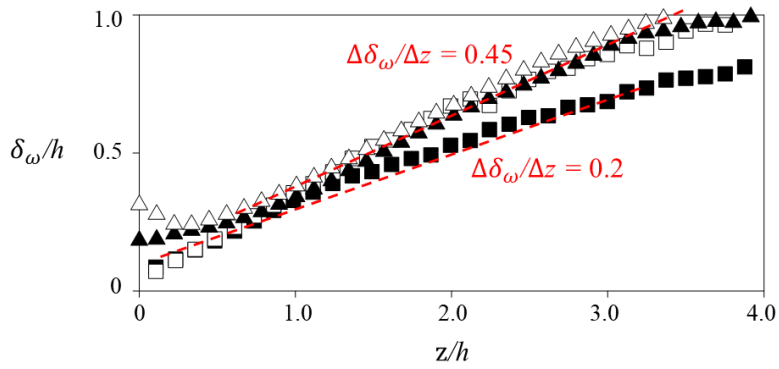
Fig. 5.15 Shear layer vorticity thickness (δ_ω/h) at $Re = 6000$: ▲, $\langle\bar{\alpha}\rangle$, $ER = 0\%$, 4.0; △, 0.72%, 4.0; ■, 0%, 9.0; □, 0.70%, 9.0.
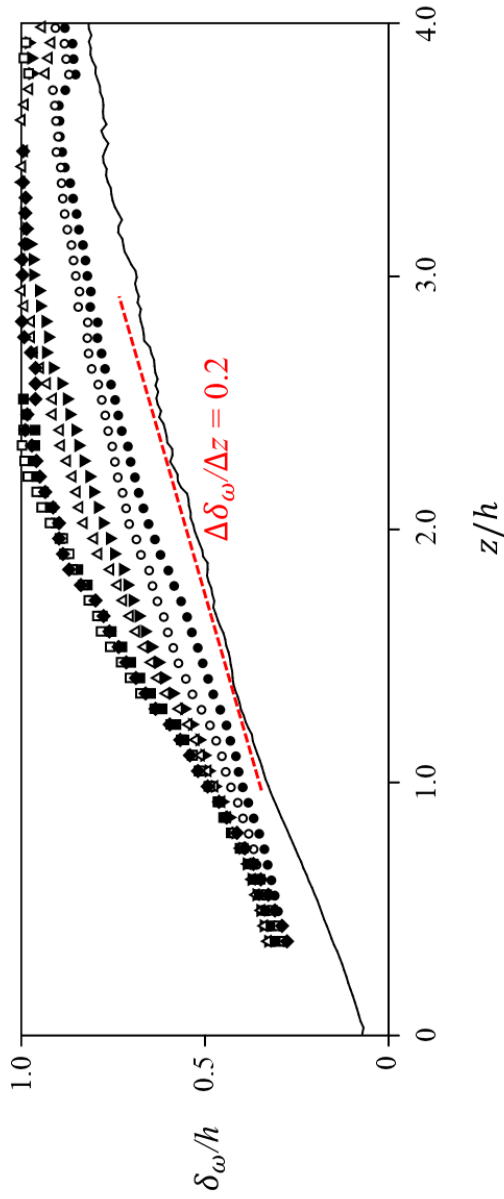
Fig. 5.16 Shear layer vorticity thickness (δ_ω/h) at Re = 6000 and ER = 9.0: solid line, single-phase flow; ●, $\langle\bar{\alpha}\rangle$ = 0.12%; ○, 0.23%; ▼, 0.43%; △, 0.70%; ■, 1.00%; □, 1.23%; ◆, 1.85%.
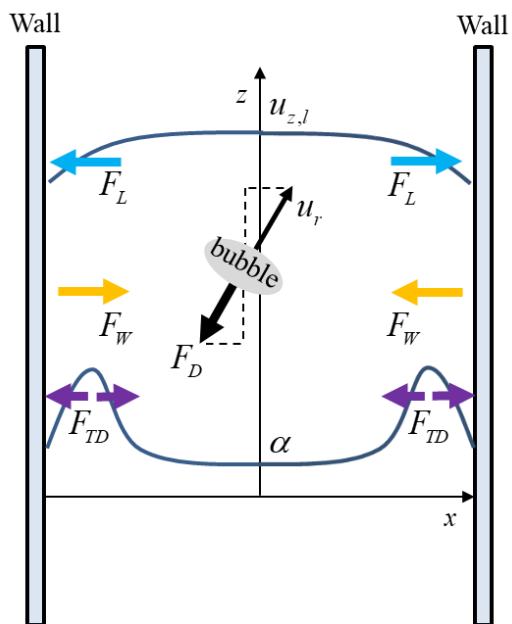
Fig. 5.17 Schematic of lateral interfacial forces acting on deformable bubble.
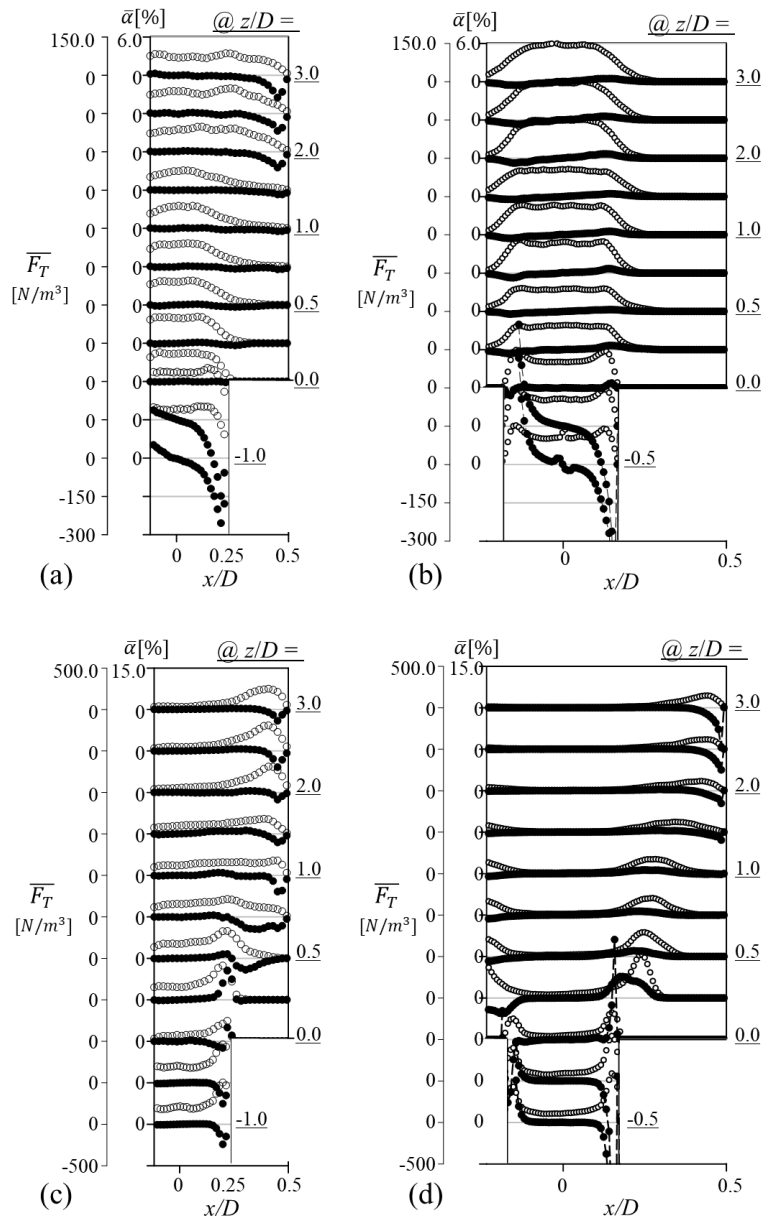
Fig. 5.18 Time-averaged net lateral force ($F_{T,x}$) acting on bubbles (●) with the void distribution (○) at (a) *Re*, $\langle\bar{\alpha}\rangle$, *ER* = 420, 0.39%, 4.0; (b) 440, 0.39%, 9.0; (c) 6000, 0.72%, 4.0; (d) 6000, 0.70%, 9.0. In vertical axes, each height (*z/D*) has the same scale.
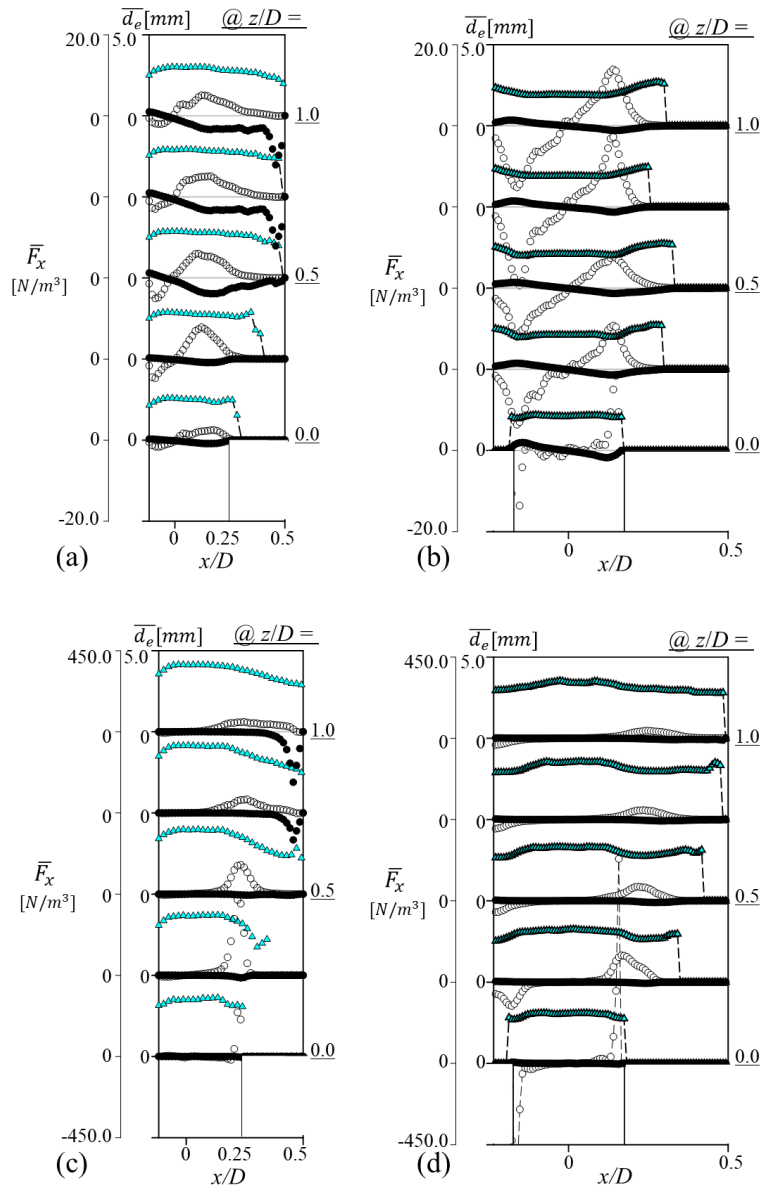
Fig. 5.19 Time-averaged lateral forces (●, wall-lubricating force; ○, wall-normal lift force) acting on bubbles with the bubble size distribution (▲) at (a) *Re*, ⟨$\bar{\alpha}$⟩, *ER* = 420, 0.39%, 4.0; (b) 440, 0.39%, 9.0; (c) 6000, 0.72%, 4.0; (d) 6000, 0.70%, 9.0. In vertical axes, each height (*z/D*) has the same scale.
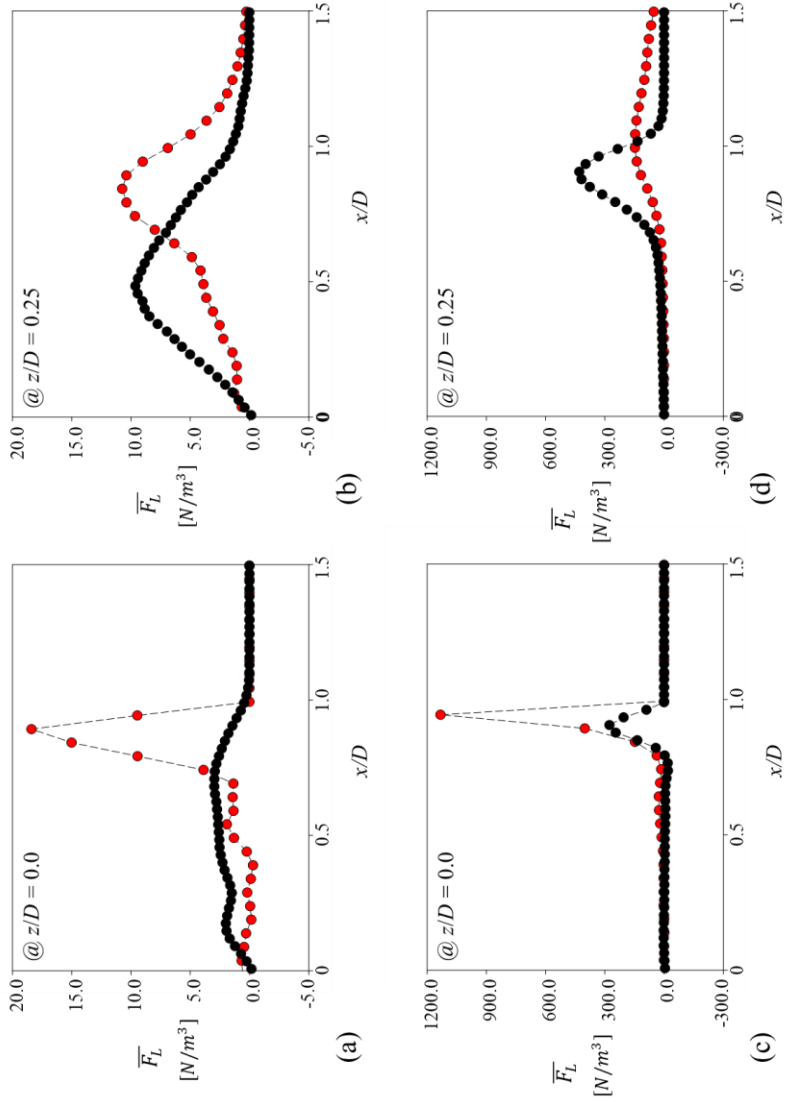
Fig. 5.20 Time-averaged wall-normal lift force acting on bubbles at (a,b) $Re \approx$ 400; (c,d) = 6000: ●, $ER = 4.0$; ●, 9.0.

Chapter 6.

Reattachment length variation

6.1 Variation of reattachment length

One of the most important factors in a sudden cross-section changed geometry is the reattachment length. We plotted the variation of reattachment length (z_R) normalized by the step height h (Fig 6.1a) and single phase reattachment length $z_{R,s}$ (Fig 6.1b) as a function of $\langle \bar{\alpha} \rangle$. In turbulent flow, all data falls on a single curve regardless of the ER changes. Interestingly, the reattachment length initially increases and then decreases as alpha increases $\langle \bar{\alpha} \rangle$. In laminar flow, unlike turbulent flow, the ER dominates the length variation and causes a gap between curves for each ER. Through the change in reattachment length, the following conclusions can be drawn: (i) the presence of bubbles can significantly reduce the reattachment length in both laminar and turbulent flows compared to single-phase flow, and (ii) the dependence of the ER is different for laminar and turbulent flows. In the following sections, we will explain the reasons behind this difference.

6.2 Effects of ER

It is well-known that in backward-facing step flow, when single-phase turbulence increases, the kinetic energy of the shear layer increases and accelerates the reattachment. However, unlike single-phase turbulence, bubbly flow causes localization of turbulence due to the movement of bubbles, which causes differences in flow behavior depending on changes in expansion ratio, mean void fraction and background turbulence. To find the reason for the difference in the reattachment length variation according to each flow condition analyzed above, SIT and BIT were linearly decomposed and analyzed. Lee & Park (2020) modeled the bubble-induced agitation of the liquid phase with a void fraction ($\bar{\alpha}$), relative velocity ($\bar{v}_r$), and the lateral gradient of each term ($\partial \bar{\alpha}/\partial x$ and $\partial \bar{v}_r/\partial x$) (eq. (6.1)).

$$u''_{z,rms} = c_1\overline{v_r}\,\overline{\alpha}^{0.1}\langle\overline{\alpha}\rangle^{0.4} + c_2\overline{d_e}\left(1 - 0.4\overline{\alpha}^{2/3}\right)\left[\overline{\alpha}^{0.1}\frac{\partial\overline{v_r}}{\partial x} + 0.1\overline{v_r}\,\overline{\alpha}^{-0.9}\frac{\partial\overline{\alpha}}{\partial x}\right] \quad (6.1)$$

Fig. 6.2 shows the development of pure bubble-induced turbulence, void fraction, and relative velocity at $Re = 6000$ with two different ERs. As the expansion ratio increased, so did the BIT, resulting in faster reattachment for the expansion ratio of 9.0 (Fig. 6.2a). Also, the ratio of BIT to total turbulence (Fig. 6.2b) is higher at the wall than in the core in both ERs, even though there are few bubbles near the wall, which means that the influence of eddies detached from the bubble is also large in the near wall region. And we were able to find that the source of the high BIT of ER 9.0 was caused by an increase in relative velocity ($\lesssim 30\%$) (Fig. 6.2d).

6.3 Effects of void fraction

To analyze the cause of the initial increase of the reattachment length with increased $\langle\overline{\alpha}\rangle$ in turbulent flow ($\langle\overline{\alpha}\rangle < 0.005$), we plot the development of rms of the liquid velocity fluctuation ($u'_{z,rms}/u_{bulk}$) of various $\langle\overline{\alpha}\rangle$ at turbulent flow with ER 9.0. At the middle of the separation bubble ($z/z_R = 0.5$), the peak of the velocity fluctuation increases with $\langle\overline{\alpha}\rangle$, similar to the trend of turbulence before the expansion (Fig. 5.6b). However, at $z/z_R = 1.0$ (flow reattach to the wall), the peak of the smallest alpha ($\langle\overline{\alpha}\rangle = 0.12\%$) overtakes the other alpha peaks, which is more evident in the lateral liquid fluctuations (Fig. 6.3d).

The case with the smallest mean void fraction ($\langle\overline{\alpha}\rangle = 0.12\%$) has the smallest liquid fluctuation value immediately after the expansion, compared to other void fractions, but due to the flow structure interaction caused by the bubble after the expansion, the BIT increases faster compared to the other $\langle\overline{\alpha}\rangle$ cases. As a result, in the range of $\langle\overline{\alpha}\rangle < 0.005$, the reattachment length of the smallest mean void fraction ($\langle\overline{\alpha}\rangle = 0.12\%$) could be shorter than the length of $\langle\overline{\alpha}\rangle = 0.23, 0.43$ %, as the total turbulence is increased. Similar to Fig. 6.2 (d), the reason for the increase in BIT at $\langle\overline{\alpha}\rangle = 0.12\%$ compared to $\langle\overline{\alpha}\rangle = 0.23, 0.43$ % was due to the increases in relative velocity (Fig. 6.4).

The cause of the BIT decrease along to $\langle\overline{\alpha}\rangle$ at a small mean void fraction ($\langle\overline{\alpha}\rangle < 0.5\%$) can be considered as follows. Immediately after expansion, the lift increases

rapidly as the ER increases (Fig. 5.19c), but after a while (z/D > 0.25), the pressure drop is greater in *ER* 9.0 than in *ER* 4.0, so the lift peak becomes smaller (Fig. 5.19 d), and the force acting on the bubble towards the wall decreased. As a result, below the BIT dominant regime ($\langle \bar{\alpha} \rangle$ > 0.5%), where the reattachment length decreases with $\langle \bar{\alpha} \rangle$ increases, when $\langle \bar{\alpha} \rangle$ increases, the reattachment length increases because bubbles migrate slowly to the wall.

Interestingly, the reattachment length in laminar flow increases slightly after $\langle \bar{\alpha} \rangle$ = 0.02. According to Celis et al (2021), for the two-phase expansion pipe flow, bubble breakup is dominant compared to the bubble coalescence after the expansion. Therefore, as the void fraction increases, bubble break-up increases which consumes the surrounding turbulence energy. As a result, for laminar flows with void fractions larger than two percent, the BIT after expansion decreases as the void fraction increases and the reattachment length becomes slightly increased or saturated.

6.4 Comparison with previous studies

Lastly, the reattachment length in the present study was compared and validated with the results of previous studies on turbulent single-phase backward-facing step flow and circular expansion pipe, based on the Reynolds number. Fig. 6.5 illustrates that in previous studies the reattachment length tended to decrease as the Reynolds number increases. The single-phase results of the present study align with this observed trend. It was confirmed that even with a small amount of bubbles in the present study, the effect of reducing the reattachment length similar to that of increasing the Reynolds number of the background flow by almost tenfold. Interestingly, the reduction in reattachment length by BIT was greater although the void fraction in this study was more than twice as small in the previous study with circular pipe.

In this study, the flow characteristics of a single-phase turbulent inlet were compared with the values measured in a fully developed circular pipe with a similar Reynolds number to determine whether this change in reattachment length according to the geometry of the pipe cross-section was caused by the inlet BIT or BIT after expansion (Westerweel et al, 1996). Fig. 6.6 shows the normalized streamwise liquid

velocity and Reynolds stress of the present square pipe and previous circular pipe experiments. It is confirmed that the flow in the center plane of the square pipe has similarities with the flow in the fully developed circular pipe. Since the expansion of the cross-sectional area in the diagonal direction of the square pipe is greater than the expansion in the side direction, it is estimated that the additional turbulence induced after the expansion will increase the BIT and result in an additional reattachment length reduction compared to the circular pipe.
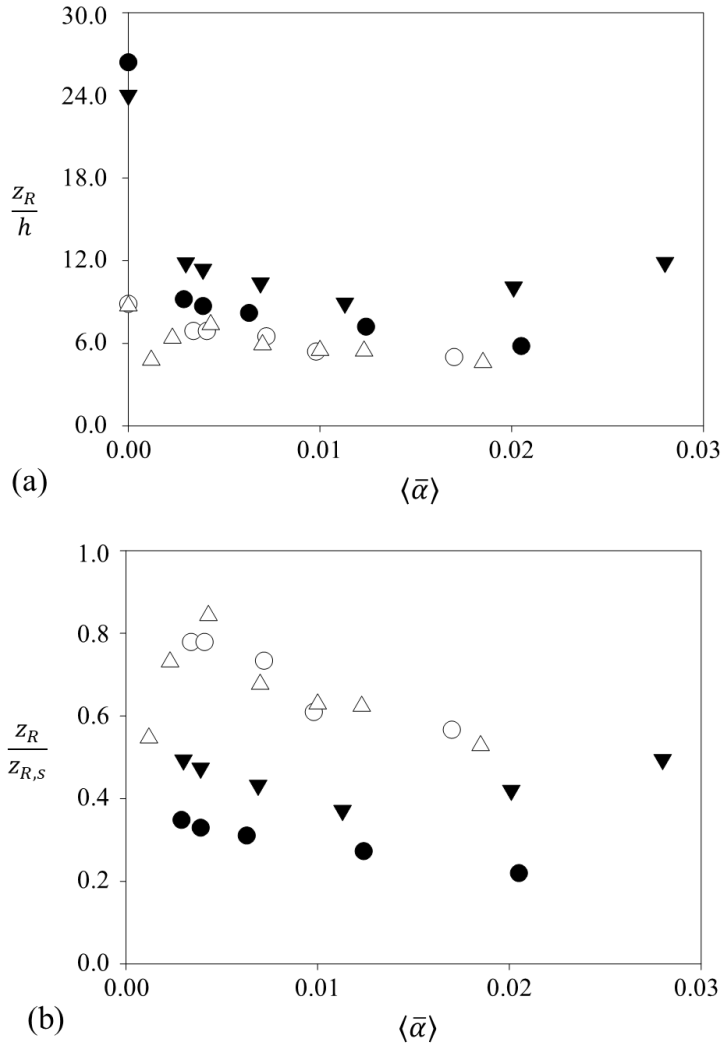
Fig. 6.1 Variation of the reattachment length (z_R) normalized by (a) step height (h); (b) reattachment length of a single-phase flow ($z_{R,s}$) with volumetric void fraction: ●, *Re, ER* = 420, 4.0; ○, 6000, 4.0; ▼, 440, 9.0; △, 6000, 9.0.
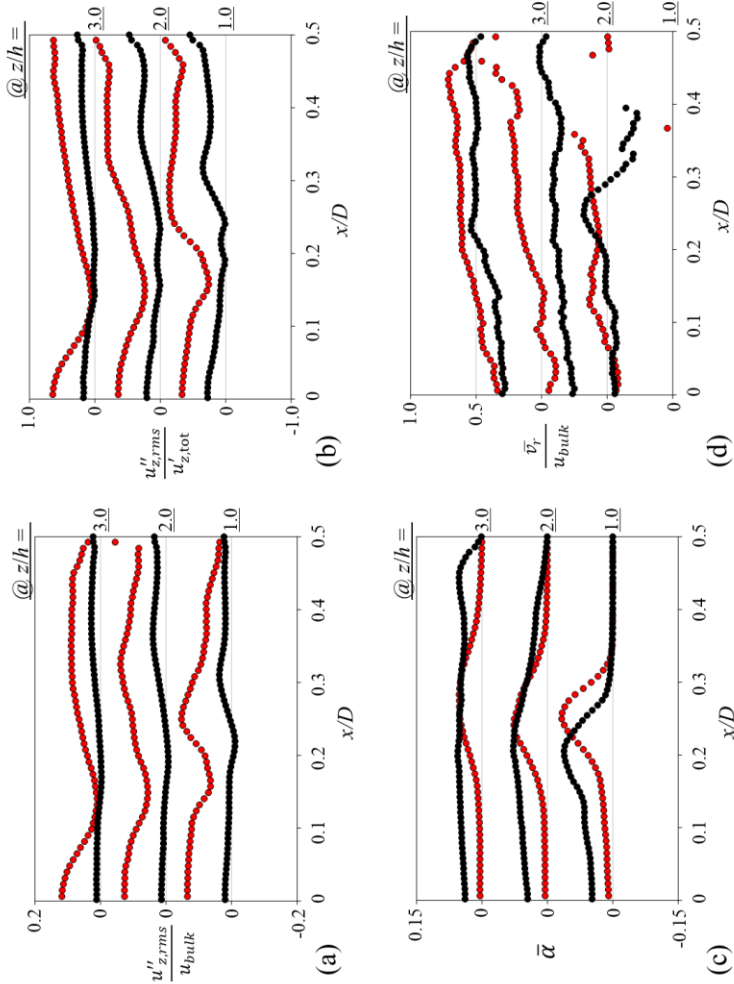
Fig. 6.2 Development of pure bubble induced turbulence at $Re = 6000$: (a) pure bubble-induced streamwise liquid velocity fluctuation ($u''_{z,rms}/u_{bulk}$); (b) ratio between pure bubble-induced streamwise liquid velocity fluctuation and total streamwise liquid velocity fluctuation ($u''_{z,rms}/u'_{z,tot}$); (c) void distribution ($\bar{\alpha}$); (d) relative velocity distribution ($\bar{v}_r/u_{bulk}$). ● , $ER = 4.0$; ● , 9.0. In vertical axes, each height (z/D) has the same scale.
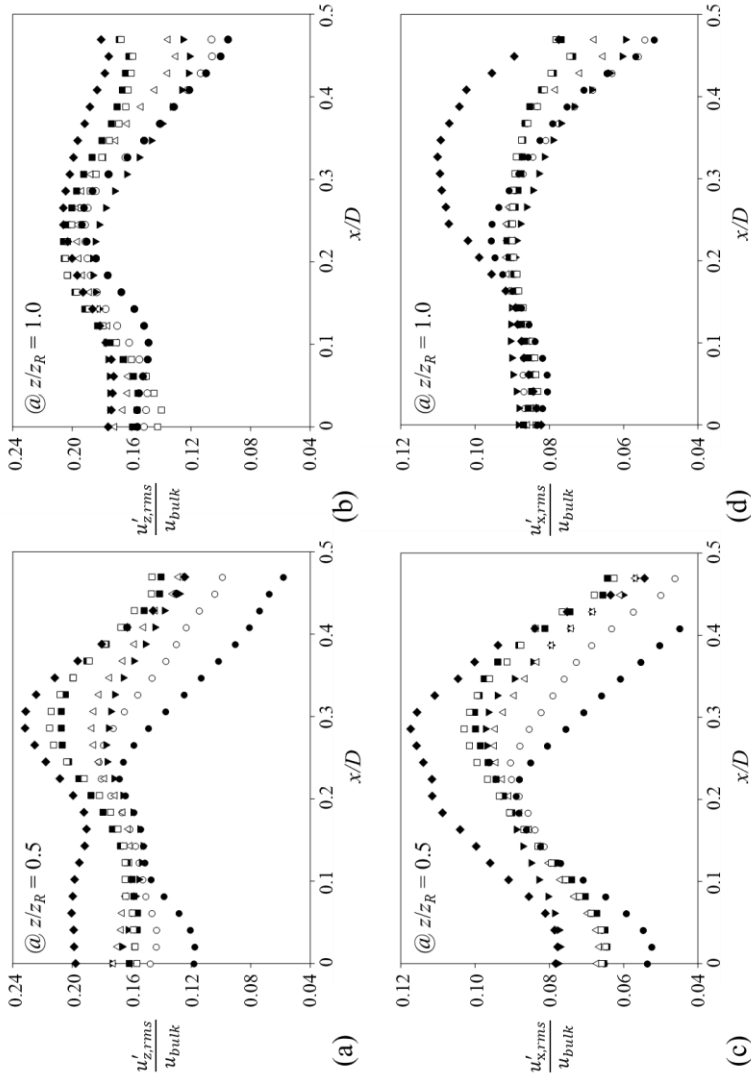
Fig. 6.3 Development of streamwise liquid velocity fluctuation ($u'_{z,rms}/u_{bulk}$) (a,b) and lateral liquid velocity fluctuation ($u'_{x,rms}/u_{bulk}$) (c-d) at $Re = 6000$ and $ER = 9.0$: ●, $\langle \bar{\alpha} \rangle = 0.12\%$; ○, 0.23%; ▼, 0.43%; △, 0.70%; ■, 1.00%; □, 1.23%; ◆, 1.85%.
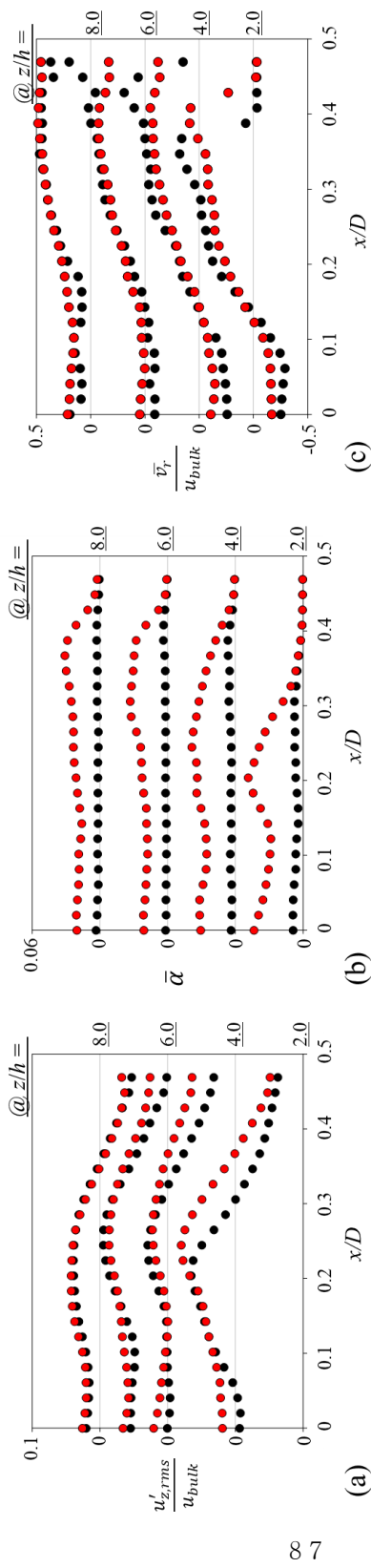
Fig. 6.4 Development of bubble induced turbulence at $Re = 6000$ and $ER = 9.0$: (a) streamwise liquid velocity fluctuation ($u'_{z,rms}/u_{bulk}$); (b) void distribution ($\bar{\alpha}$); (c) relative velocity distribution ($\bar{v}_r/u_{bulk}$). ●, $\langle\bar{\alpha}\rangle =$ 0.12%; ●, 0.43%. In vertical axes, each height (z/D) has the same scale.
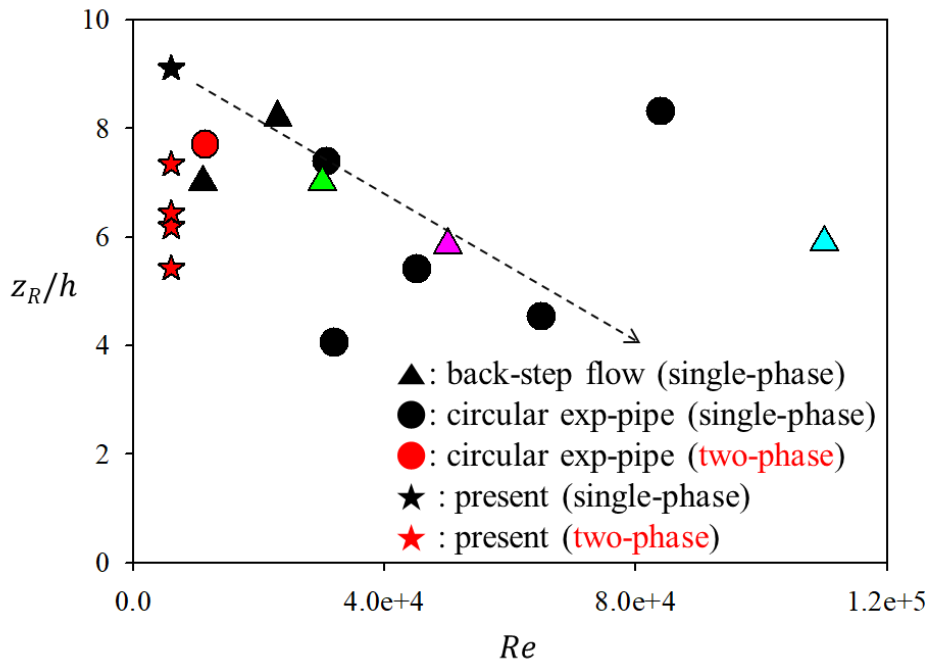
Fig. 6.5 Comparison of the reattachment length with previous studies in turbulent regime ▲ : Eaton & Johnston (1981); ▲, Kim et al. (1978); ▲, Baker (1975); ▲, Chandrsuda et al. (1978); ●, So (1987); ●, Pakhomov & Terekhov (2016); ★, present (single-phase); ★, present (two-phase).
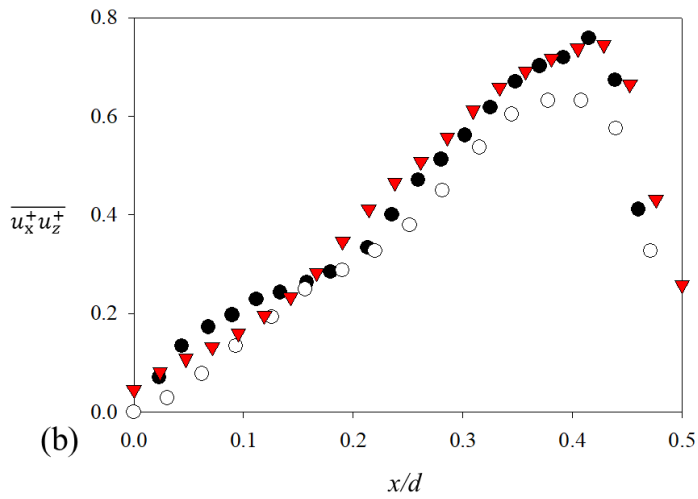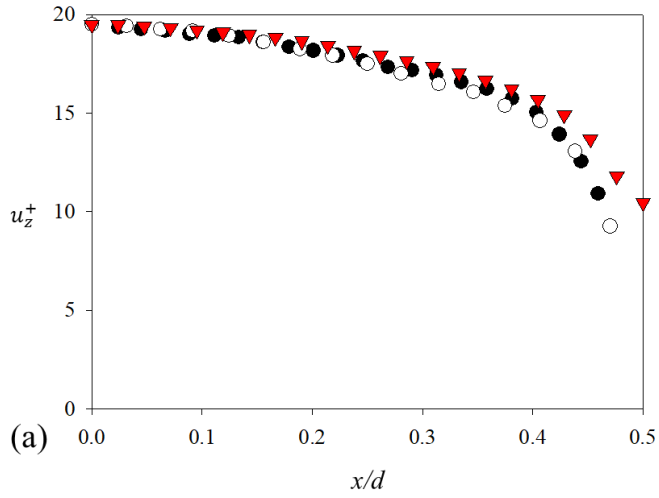
Fig. 6.6 Comparison of the present inlet single-phase flow characteristics with fully developed circular turbulent pipe data (Westerweel et al, 1996): (a) normalized streamwise liquid velocity (u_z^+); (b) normalized Reynolds stress ($\overline{u_x^+ u_z^+}$) with friction velocity. ●, PIV (Re = 5300); ○, DPIV (Re = 5300); ▼, Present (Re = 6000)

Chapter 7.

Concluding remarks

In the present study, we have experimentally investigated the air-water bubbly flows in an upward square pipe with a sudden expansion in a cross-sectional area, focusing on the bubble dynamics and the effect of bubbles on the liquid-phase flow (especially, the reattachment length variation with expansion ratio and bubble-induce turbulence and its mechanism). As a steeper velocity gradient and subsequent turbulence are induced along the separating shear layer at the expansion edge, the bubbly flows are affected by how the bubbles interact with this shear flow. For example, at the small expiation ratio, after the expansion, smaller bubbles tend to migrate toward the wall while larger ones rise in a core region, which is encouraged more as the Reynolds number increases.

However, in a large expansion ratio, due to the large pressure drop and distance from the wall, large bubbles have a chance to reach the wall, and a bubble-size peak is shown near the wall. The shear layer spreading rate that determines the change in the reattachment length is estimated by shear layer vorticity thickness. The injection of bubbles increased the shear layer spreading rate, and as the mean void fraction increased, the initial shear layer vorticity thickness gradient also increased.

The relation between the liquid-phase velocity gradient and the lateral migration of bubbles was examined by calculating the interfacial forces acting on rising bubbles. Based on this lateral bubble dispersion after the expansion, the liquid-phase flow characteristics are modulated as well. That is, the flow acceleration and enhancement of turbulence are locally induced near the separation edge and are widened toward the wall as the flow develops downstream. However, due to the enhanced fluid mixing, the disturbed flow statistics saturate faster than the single-phase flow. The locally enhanced turbulence in the separating shear layer, on the other hand, is found to be the main reason for the reattachment length reduction in two-phase flows.

Summarizing the effect of bubble and expansion ratio, we found that bubbles can greatly decrease reattachment length in both laminar and turbulent flows

compared to single-phase flow, and the expansion ratio affects laminar and turbulent flows differently.

As the void fraction increases ($\langle\bar{\alpha}\rangle > 0.005$), the amount of reattachment length reduction increases, but the overall effect of reattachment length reduction by bubbles is mitigated as the Reynolds number of the background flow increases. However, turbulent flow with a small void fraction ($\langle\bar{\alpha}\rangle < 0.005$) shows reversed reattachment length reduction, i.e., the reattachment length increases with void fraction increases, due to the small bubble-induced turbulence comparable to a large pressure drop. In turbulent flow, there was a faster reattachment for an expansion ratio of 9.0 compared to 4.0 due to an increase in BIT as the expansion ratio increased.

Moreover, in turbulent flow, the dependence of the reattachment length reduction compared to single-phase flow on the expansion ratio disappears due to the high turbulence of the background flow, and the reattachment reduction of laminar flow is dominated by the expansion ratio. And it is found that the BIT caused by the difference in the relative velocity of the bubbles was the main factor causing the change in the reattachment length in the present set-up.

The present study is significant as it is the first study to investigate the effect of BIT on reattachment length across various void fractions and provide an explanation for the observed changes. We think the present study provides us with a good starting point to develop more rigorous models that are applicable to wider ranges of two-phase flow conditions and also serves as reference data to validate the numerical simulations. This requires further analysis of the flow regime with small or large void fractions where the trend of decreasing reattachment length with increasing inlet BIT does not maintain.

As the number of bubbles increases, bubble-bubble interactions become more active, which affects the BIT after expansion. Therefore, additional discussions on the bubble break-up and coalescence effects in a sudden expansion pipe are necessary. In addition, to analyze the interaction between inlet turbulence and BIT, it is useful to measure the BIT after the expansion as the amount of background turbulence changes.

Bibliography

Adams, E.W. & Johnston, J.P. 1988 Flow structure in the near-wall zone of a turbulent separated flow. *AIAA J.* **26**, 932-939.

Ahmed, W. H., Ching, C. Y. & Shoukri, M. 2008 Development of two-phase flow downstream of a horizontal sudden expansion. *Int. J. Heat Mass Transf.* **29**, 194-206.

Ali, S. et al. 2020 An objective comparison of detection and segmentation algorithms for artefacts in clinical endoscopy. *Sci. Rep.* **10**, 2748.

Alméras, E., Mathai, V., Lohse, D. & Sun, C. 2017 Experimental investigation of the turbulence induced by a bubble swarm rising within incident turbulence. *J. Fluid Mech.* **825**, 1091-1112.

Aloui, F. & Souhar, M. 1996 Experimental study of a two-phase bubbly flow in a flat duct symmetric sudden expansion-Part II: Liquid and bubble velocities, bubble sizes. *Int. J. Multiphas. Flow* **22**, 849-861.

Aloui, F., Doubliez, L., Legrand, J. & Souhar, M. 1999 Bubbly flow in an axisymmetric sudden expansion: Pressure drop, void fraction, wall shear stress, bubble velocities and sizes. *Exp. Therm. Fluid Sci.* **19**, 118-130.

Aoyama, S., Hayashi, K., Hosokawa, S., Lucas, D. & Tomiyama, A. 2017 Lift force acting on single bubbles in linear shear flows. *Int. J. Multiphas. Flow* **96**, 113-122.

Attou, A., Giot, M. & Seynhaeve, J.M. 1997 Modelling of steady-state two-phase bubbly flow through a sudden enlargement. *Int. J. Heat Mass Transf.* **40**, 3375-3385.

Bröder, D. & Sommerfeld, M. 2007 Planar shadow image velocimetry for the analysis of the hydrodynamics in bubbly flows. *Meas. Sci. Technol.* **18**, 2513-2528.

Brunton, S. L., Noack, B. R. & Koumoutsakos, P. 2020 Machine learning for fluid mechanics. *Annu. Rev. Fluid Mech.* **52**, 477-508.

Caicedo, J. C. et al. 2019 Nucleus segmentation across imaging experiments: the 2018 Data Science Bowl. *Nat. Methods* **16**, 1247-1253.

Celis, G. E. O., Rosero, C. M. P., Loureiro, J. B. R. & Freire, A. S. 2021 Breakup

and coalescence of large and small bubbles in sudden expansions and contractions in vertical pipes. *Int. J. Multiphas. Flow* **137**, 103548.

Cerqueira, R. F. L & Paladino, E. E. 2020 Development of a deep learning-based image processing technique for bubble pattern recognition and shape reconstruction in dense bubbly flows. *Chem. Eng. Sci*. **230**, 116163.

Chandrsuda, C., Mehta, R. D., Weir, A. D. & Bradshaw, P. 1978 Effect of free-stream turbulence on large structure in turbulent mixing layers. *J. Fluid Mech*. **85**, 693-704.

Chen, G., Weng, Q., Hay, G. J. & He, Y. 2018 Geographic object-based image analysis (GEOBIA): emerging trends and future opportunities. *GIsci. Remote Sens*. **55**, 159-182.

Cho, Y. S. et al. 2020 Automated measurement of hydrops ratio from MRI in patients with Ménière's disease using CNN-based segmentation. *Sci. Rep*. **10**, 7003.

Choi, D., Kim, H. & Park, H. 2022 Bubble velocimetry using the conventional and CNN-based optical flow algorithms. *Sci. Rep*. **12**, 11879.

Chun-Yu, G., Yi-Wei, F., Yang, H., Peng, X. & Yun-Fei, K. 2021 Deep-learning-based liquid extraction algorithm for particle image velocimetry in two-phase flow experiments of an object entering water. *Appl. Ocean Res*. **108**, 102526.

Chun, K.B. & Sung, H.J. 1996 Control of turbulent separated flow over a backward-facing step by local forcing. *Exp. Fluids* **21**, 417-426.

Clift, R., Grave, J.R. & Weber, M.E. 1978 *Bubbles, Drops, and Particles*. Academic.

Cramer, K.R. 1958 On laminar separation bubbles. *J. Aerosp. Sci*. **25**, 143-144.

Eaton, J. K. & Johnston, J. P. 1981 A review of research on subsonic turbulent flow reattachment. *AIAA J*. **19**, 1093-1100.

Fan, L.S. & Tsuchiya, K. 1990 *Bubble wake dynamics in liquids and liquid-solid suspensions*. Butterworths-Heinemann, Butterworths.

Farnebäck, Gunnar. 2003 *Two-frame motion estimation based on polynomial expansion. Image Analysis: 13th Scandinavian Conference, SCIA 2003 Halmstad, Sweden, June 29–July 2, 2003 Proceedings 13*. Springer Berlin Heidelberg.

Farrokhpay, S., Filippov, L. & Fornasiero, D. 2021 Flotation of fine particles: A review. *Miner. Process. Extr. Metall. Rev*. **42**, 473-483.

Fessler, J.R. & Eaton, J.K. 1999 Turbulence modification by particles in a backward-

facing step flow. *J. Fluid Mech.* **394**, 97-117.

Frank, T., Zwart, P. J., Krepper, E., Prasser, H. M. & Lucas, D. 2008 Validation of CFD models for mono-and polydisperse air–water two-phase flows in pipes. *Nucl. Eng. Des.* **238**, 647-659.

Fu, Y. & Liu, Y. 2016 Development of a robust image processing technique for bubbly flow measurement in a narrow rectangular channel. *Int. J. Multiphas. Flow* **84**, 217-228.

Fu, Y. & Liu, Y. 2018 3D bubble reconstruction using multiple cameras and space carving method. *Meas. Sci. Technol.* **29**, 075206.

Fu, Y. & Liu, Y. 2019 BubGAN: Bubble generative adversarial networks for synthesizing realistic bubbly flow images. *Chem. Eng. Sci.* **204**, 35-47.

Furuichi, N., Takeda, Y. & Kumada, M. 2003 Spatial structure of the flow through an axisymmetric sudden expansion. *Exp. Fluids* **34**, 643-650.

Gai, S.L. & Sharma, S.D. 1984 Subsonic turbulent flow over a rearward facing segmented step. *Phys. Fluids* **27**, 544-546.

Goldstein, R.J., Eriksen, V.L., Olson, R.M. & Eckert, E.R.G. 1970 Laminar separation, reattachment, and transition of the flow over a downstream-facing step. *J. Basic Eng.* **92**, 732-739.

Gordiychuk, A., Svanera, M., Benini, S. & Poesio, P. 2016 Size distribution and Sauter mean diameter of micro bubbles for a Venturi type bubble generator. *Exp. Therm. Fluid Sci.* **70**, 51-60.

Haas, T., Schubert, C., Eickhoff, M. & Pfeifer, H. 2020 BubCNN: Bubble detection using Faster RCNN and shape regression network. *Chem. Eng. Sci.* **216**, 115467.

He, K., Gkioxari, G., Dollár, P. & Girshick, R. 2017 Mask R-CNN. *Proc. IEEE Int. Conf. Comput. Vis.* 2961-2969.

Hosokawa, S. & Tomiyama, A. 2013 Bubble-induced pseudo turbulence in laminar pipe flows. *Int. J. Heat Fluid Flow* **40**, 97-105.

Hosokawa, S., Suzuki, T. & Tomiyama, A. 2012 Turbulence kinetic energy budget in bubbly flows in a vertical duct. *Exp. Fluids* **52**, 719-728.

Hosokawa, S., Tanaka, K., Tomiyama, A., Maeda, Y. Yamaguchi, S. & Ito, Y. 2009 Measurement of micro bubbles generated by a pressurized dissolution method. *J. Phys.: Conf. Series*. **147**, 012016.

Ishii, M. & Zuber, N. 1979 Drag coefficient and relative velocity in bubbly, droplet or particulate flows. *AIChE J.* **25**, 843-855.

Jeong, H. & Park, H. 2015 Near-wall rising behaviour of a deformable bubble at high Reynolds number. *J. Fluid Mech.* **771**, 564–594.

Jović, S. 1998 Recovery of reattached turbulent shear layers. *Exp. Therm. Fluid Sci.* **17**, 57-62.

Jung, H., Yoon, S., Kim, Y., Lee, J. H., Park, H., Kim, D., Kim J. & Kang, S. 2020 Development and evaluation of data-driven modeling for bubble size in turbulent bubbly flows using artificial multi-layer neural networks. *Chem. Eng. Sci*. **213**, 115357.

Jürgens, W. & Kaltenbach, H. J. 2012 The effect of sweep on the forced transitional flow over a backward-facing step. *Comput. Fluids* **59**, 1-10.

Kang, S. & Choi, H. 2002 Suboptimal feedback control of turbulent flow over a backward-facing step. *J. Fluid Mech.* **463**, 201-227.

Karn, A., Ellis, C., Arndt, R. & Hong, J. 2015 An integrative image measurement technique for dense bubbly flows with a wide size distribution. *Chem. Eng. Sci.* **122**, 240-249.

Kashinsky, O. N., Timkin, L. S. & Cartellier, A. 1993 Experimental study of "laminar" bubbly flows in a vertical pipe. *Exp. Fluids* **15**, 308-314.

Khezzar, L., Whitelaw, J. H. & Yianneskis, M. 1986 Round sudden-expansion flows. *Proc. Inst. Mech. Eng.* **200**, 447-455.

Kim, H. & Park, H. 2022 Bubble dynamics and induced flow in a subcooled nucleate pool boiling with varying subcooled temperature. *Int. J. Heat Mass Transf.* **183**, 122054.

Kim, J. & Lee, C. 2020 Prediction of turbulent heat transfer using convolutional neural networks. *J. Fluid Mech*. **882**, A18.

Kim, J., Kline, S.J. & Johnston, J.P. 1980 Investigation of a reattaching turbulent shear layer: Flow over a backward-facing step. *ASME Trans. J. Fluids Eng.* **102**, 302-308.

Kim, M., Lee, J.H. & Park, H. 2016 Study of bubble-induced turbulence in upward laminar bubbly pipe flows measured with a two-phase particle image velocimetry. *Exp. Fluids* **57**, 1-21.

Kim, Y. & Park, H. 2019 Upward bubbly flows in a square pipe with a sudden expansion: Bubble dispersion and reattachment length. *Int. J. Multiphas. Flow* **118**, 254-269.

Kim, Y. & Park, H. 2021 Deep learning-based automated and universal bubble detection and mask extraction in complex two-phase flows. *Sci. Rep*. **11**, 8940.

Lahey Jr, R. T., De Bertodano, M. L. & Jones Jr, O. C. 1993 Phase distribution in complex geometry conduits. *Nucl. Eng. Des*. **141**, 177-201.

Lance, M. & Bataille, J. 1991 Turbulence in the liquid phase of a uniform bubbly air–water flow. *J. Fluid Mech.* **222**, 95-118.

Lau, Y., Deen, N. & Kuipers, J. 2013 Development of an image measurement technique for size distribution in dense bubbly flows. *Chem. Eng. Sci*. **94**, 20-29.

Lawson, N. J., Rudman, M., Guerra, A. & Liow, J. L. 1999 Experimental and numerical comparisons of the break-up of a large bubble. *Exp. Fluids* **26**, 524-534.

Lee, J. & Park, H. 2017 Wake structures behind an oscillating bubble rising close to a vertical wall. *Int. J. Multiphas. Flow* **91**, 225-242.

Lee, J. & Park, H. 2020 Bubble dynamics and bubble-induced agitation in the homogeneous bubble-swarm past a circular cylinder at small to moderate void fractions. *Phys. Rev. Fluids* **5**, 054304.

Lee, J. H., Kim, H., Lee, J. & Park, H. 2021 Scale-wise analysis of upward turbulent bubbly flows: An experimental study. *Phys. Fluids* **33**, 053316.

Li, J., Shao, S. & Hong, J. 2020 Machine learning shadowgraph for particle size and shape characterization. *Meas. Sci. Tech*. **32**, 015406.

Li, Y., Qi, H., Dai, J., Ji, X. & Wei, Y. 2017 Fully convolutional instance-aware semantic segmentation. *Proc. IEEE Int. Conf. Comput. Vis.* 2359-2367.

Lindken, R. & Merzkirch, W. 2002 A novel PIV technique for measurements in multiphase flows and its application to two-phase bubbly flows. *Exp. Fluids* **33**, 814-825.

Liu, T. J. & Bankoff, S. G. 1993 Structure of air-water bubbly flow in a vertical pipe—II. Void fraction, bubble velocity and bubble size distribution. *Int. J. Heat Mass Transf.* **36**, 1061-1072.

Lu, J., Biswas, S. & Tryggvason, G. 2006 A DNS study of laminar bubbly flows in

a vertical channel. *Int. J. Heat Mass Transf.* **32**, 643-660.

Martínez-Mercado, J., Palacios-Morales, C.A. & Zenit, R. 2007 Measurement of pseudoturbulence intensity in monodispersed bubbly liquids for $10 < Re < 500$. *Phys. Fluids* **19**, 103302.

Michiyoshi, I. & Serizawa, A. 1986 Turbulence in two-phase bubbly flow. *Nucl. Eng. Des.* **95**, 253-267.

Moen, E., Bannon, D., Kudo, T., Graf, W., Covert, M. & van Valen, D. 2019 Deep learning for cellular image analysis. *Nat. Methods* **16**, 1233-1246.

Moshkov, N., Mathe, B., Kertesz-Farkas, A., Hollandi, R. & Horvath, P. 2020 Test-time augmentation for deep learning-based cell segmentation on microscopy images. *Sci. Rep*. **10**, 5068.

Oktay, A. B. & Gurses, A. 2019 Automatic detection, localization and segmentation of nano-particles with deep learning in microscopy images. *Micron* **120**, 113-119.

Ötügen, M.V. 1991 Expansion ratio effects on the separated shear layer and reattachment downstream of a backward-facing step. *Exp. Fluids* **10**, 273-280.

Pakhomov, M.A. & Terekhov, V.I. 2016 Modeling of the flow patterns and heat transfer in a turbulent bubbly polydispersed flow downstream of a sudden pipe expansion. *Int. J. Heat Mass Transf.* **101**, 1251-1262.

Pang, M. & Wei, J. 2013 Experimental investigation on the turbulence channel flow laden with small bubbles by PIV. *Chem. Eng. Sci.* **94**, 302-315

Park, H., Jeon, W.-P., Choi, H. & Yoo, J.Y. 2007 Mixing enhancement behind a backward-facing step using tabs. *Phys. Fluids* **19**, 105103.

Park, J. & Choi, H. 2020 Machine-learning-based feedback control for drag reduction in a turbulent channel flow. *J. Fluid Mech*. **904**, A24

Park, J. & Park, H. 2021 Particle dispersion induced by vortical interactions in a particle-laden upward jet with a partial crossflow. *J. Fluid Mech*. **915**, A5.

Petrick, M. & Swanson, B.S. 1959 Expansion and contraction of an air-water mixture in vertical flow. *AIChE J.* **5**, 440-445.

Poletaev, I., Tokarev, M. P. & Pervunin, K. S. 2020 Bubble patterns recognition using neural networks: Application to the analysis of a two-phase bubbly jet. *Int. J. Multiphas. Flow* **126**, 103194.

Pope, S. B. 2000 *Turbulent flows*. Cambridge university press.

Prakash, V. N., Mercado, J. M., van Wijngaarden, L., Mancilla, E., Tagawa, Y., Lohse, D. & Sun, C. 2016 Energy spectra in turbulent bubbly flows. *J. Fluid Mech.* **791**, 174-190.

Ren, S., He, K., Girshick, R. & Sun, J. 2015 Faster R-CNN: Towards real-time object detection with region proposal networks. *Adv. Neural Inf. Process. Syst.* **28**, 91-99.

Rensen, J. Luther, S. & Lohse, D. 2005 The effect of bubbles on developed turbulence. *J. Fluid Mech.* **538**, 153-187.

Riboux, G., Legendre, D. & Risso, F. 2013 A model of bubble-induced turbulence based on large-scale wake interactions. *J. Fluid. Mech.* **719**, 362-387.

Riboux, G., Risso, F. & Legendre, D. 2010 Experimental characterization of the agitation generated by bubbles rising at high Reynolds number. *J. Fluid Mech.* **643**, 509-539.

Rinne, A. & Loth, R. 1996 Development of local two-phase flow parameters for vertical bubbly flow in a pipe with sudden expansion. *Exp. Therm. Fluid Sci.* **13**, 152-166.

Risso, F. & Ellingsen, K. 2002 Velocity fluctuations in a homogeneous dilute dispersion of high-Reynolds-number rising bubbles. *J. Fluid Mech.* **453**, 395-410.

Sathe, M. J., Thaker, I. H., Strand, T. E. & Joshi, J. B. 2010 Advanced PIV/LIF and shadowgraphy system to visualize flow structure in two-phase bubbly flows. *Chem. Eng. Sci.* **65**, 2431-2442.

Sato, Y. & Sekoguchi, K. 1975 Liquid velocity distribution in two-phase bubble flow. *Int. J. Multiphas. Flow* **2**, 79-95.

Sauvola, J. & Pietikäinen, M. 2000 Adaptive document image binarization. *Pattern Recognit.* **33**, 225-236.

Schlegel, J. P., Sawant, P., Paranjape, S., Ozar, B., Hibiki, T. & Ishii, M. 2009 Void fraction and flow regime in adiabatic upward two-phase flow in large diameter vertical pipes. *Nucl. Eng. Des.* **239**, 2864-2874.

Schrijer, F. F. J., Sciacchitano, A. & Scarano, F. 2014 Spatio-temporal and modal analysis of unsteady fluctuations in a high-subsonic base flow. *Phys. Fluids*, **26**, 086101.

Serizawa, A., Kataoka, I. & Michiyoshi, I. 1975 Turbulence structure of air-water

bubbly flow-II. Local properties. *Int. J. Multiphas. Flow* **2**, 235-246.

Smits, A. J. & Dussauge, J. P. 2006 *Turbulent shear layers in supersonic flow*. Springer Science & Business Media.

So, R.M.C. 1987 Inlet centerline turbulence effects on reattachment length in axisymmetric sudden-expansion flows. *Exp. Fluids* **5**, 424-426.

Soille, P. 2013 *Morphological image analysis: principles and applications.* Springer Science & Business Media.

Stephens, D. J. & Allan, V. J. 2003 Light microscopy techniques for live cell imaging. *Science* **300**, 82-86

Stoecklein, D., Lore, K. G., Davies, M., Sarkar, S. & Ganapathysubramanian, B. 2017 Deep learning for flow sculpting: Insights into efficient learning using scientific simulation data. *Sci. Rep.* **7**, 46368.

Stöhr, M., Schanze, J. & Khalili, A. 2009 Visualization of gas-liquid mass transfer and wake structure of rising bubbles using pH-sensitive PLIF. *Exp. Fluids* **47**, 135-143.

Terekhov, V. I., Smul'skii, Y. I. & Sharov, K. A. 2012 Interference of separated flows behind backward-facing step in the presence of passive control. *Tech. Phys. Lett.* **38**, 125-128.

Theofanous, T.G. & Sullivan, J. 1982 Turbulence in two-phase dispersed flows. *J. Fluid Mech.* **116**, 343–362.

Tomiyama, A. 1995 Effects of Eotvos number and dimensionless liquid volumetric flux on lateral motion of a bubble in a laminar duct flow. *Proc. 2nd Int. Conf. Multiphas. Flow.*

Tomiyama, A., Tamai, H., Zun, I. & Hosokawa, S. 2002 Transverse migration of single bubbles in simple shear flows. *Chem. Eng. Sci.* **57**, 1849-1858.

Torisaki, S. & Miwa, S. 2020 Robust bubble feature extraction in gas-liquid two-phase flow using object detection technique. *J. Nucl. Sci. Tech.* **57**, 1231-1244.

Van der Welle, R. 1985 Void fraction, bubble velocity and bubble size in two-phase flow. *Int. J. Multiphas. Flow* **11**, 317-345.

Villegas, L. R., Colombet, D., Guiraud, P., Legendre, D., Cazin, S. & Cockx, A. 2019 Image processing for the experimental investigation of dense dispersed flows: Application to bubbly flows. *Int. J. Multiphas. Flow* **111**, 16-30.

Voutsinas, A., Shakouchi, T., Tsujimoto, K. & Ando, T. 2009 Investigation of bubble size effect on vertical upward bubbly two-phase pipe flow consisted with an abrupt expansion. *J. Fluid Sci. Tech.* **4**, 442-453.

Wang, S.K., Lee, S.J., Jones, O.C. Jr. & Lahey, R.T. 1987 3-D turbulence structure and phase distribution measurements in bubbly two-phase flows. *Int. J. Multiphas. Flow* **13**, 327-343.

Westerweel, J., Draad, A. A., Van der Hoeven, J. T. & Van Oord, J. 1996 Measurement of fully-developed turbulent pipe flow with digital particle image velocimetry. *Exp. Fluids* **20**, 165-177.

Xie, X. 2008 A review of recent advances in surface defect detection using texture analysis techniques. *ELCVIA* **7**, 1-22.

Ye, S., Zhang, Z., Song, X., Wang, Y., Chen, Y. & Huang, C. 2020 A flow feature detection method for modeling pressure distribution around a cylinder in non-uniform flows by using a convolutional neural network. *Sci. Rep.* **10**, 4459.

Zhong, S., Zou, X., Zhang, Z. & Tian, H. 2016 A flexible image analysis method for measuring bubble parameters. *Chem. Eng. Sci*. **141**, 143-153.

Zhou, X., Doup, B. & Sun, X. 2013 Measurements of liquid-phase turbulence in gas–liquid two-phase flows using particle image velocimetry. *Meas. Sci. Technol.* **24**, 125303.

사각 팽창관 내 기포류 유동에서 재부착길이 변화에 대한 실험연구

서울대학교 대학원
기계항공공학부
김예원(KIM YEWON)

요약

본 연구에서는 고속 2상 입자영상속도계(PIV)와 그림자영상기법을 활용하여 기체상과 액체상을 동시에 측정하여 단면적이 급격한 팽창하는 정사각관의 공기-물 2상 유동에서 유동 특성을 실험적으로 조사하였다. 우리는 액체상 Reynolds 수를 각각 Re = 400(층류) 및 6000(난류)으로, 면적 팽창비를 ER = 4.0 과 9.0으로 설정하였으며 평균 체적 기포분율($\langle \bar{\alpha} \rangle$)은 0% (단상유동)에서 2.80%까지 변화시켰다. 기체상 영상의 분석을 위해 기존 영상처리 기술을 대체하여 시간을 절약할 수 있는 딥러닝 기반의 자동화된 기포 마스크 추출 알고리즘을 개발하여 기포 특성 분석에 적용하였다. 기포분율과 팽창비에 따른 액체상 속도장을 단상유동과도 비교하는 동시에 3차원 기포분포, 기포속도, 궤적을 측정하였다. 크기가 큰 기포는 팽창 직후 더 강한 양력을 경험하여 작은 기포에 비해 빠르게 벽을 향해 이동하는 것이 관찰되었으며, 레이놀즈 수가 증가함에 따라 액체상 속도 구배가 더 가파르게 변하기 때문에 이러한 기포 크기에 따른 이동 양상은 촉진된다. 그러나 팽창비가 작으면 큰 기포는 벽 반발력을 극복하지 못하고 관의 중심부로 밀려나 상승하게 되고 팽창비가 커지면 큰 기포는 벽에 도달할 수 있으며 벽 근처에서 기포 크기의 피크가 관찰된다. 또한 팽창비와 평균 기포분율이 액체상의 유동특성 변화에 미치는 영향을 분석하고, 전단층 와도 두께를 계산하여 기포와 파이프 형상이 전단층의 발달 속도에 미치는 영향을 분석하였다.

　　액체상의 유동 특성에 의해 기포 크기의 분포가 변하는 양상을 설명하기 위해 액체상의 유동장을 기반으로 상승하는 기포에 작용하는 계면힘을 계산하여 검증하였다. 기포 분포의 영향을 받아 팽창 전 유동의 난류도가 강화되고 이는 분리 전단층에 에너지를 공급하여 계단 뒤의 재부착 길이를 감소시킨다. 마지막으로 유동조건 및 배관형상에 따라 재부착길이가 변화하는 양상을 정리하였고 특히 팽창비와 기포분율의 영향을 상세히 분석하였다. 본 연구 결과는 실제 산업현장에서 사용되는 구조인 팽창 내의 기체－액체 2상 유동의 유동 조건에 따른 재부착 길이의 변화와 두 상간의 상호작용에 대한 보다 깊은 이해에 도움이 될 것으로 기대한다.